Bio-inspired Approaches for Human Locomotion: From Concepts to Applications

Biologisch inspirierte Ansätze für die menschliche Fortbewegung: Von Konzepten zur Anwendungen

Zur Erlangung des Grades eines Doktors der Naturwissenschaften (Dr. rer. nat.)
vorgelegte Dissertation von M.Sc. Guoping Zhao aus Huai'an, Jiangsu, P.R. China
Fachbereich Humanwissenschaften, Technische Universität Darmstadt
Tag der Einreichung: 27 Juli 2019, Tag der Prüfung: 01 Oktober 2019
Darmstadt — D 17

1. Gutachten: Prof. Dr. André Seyfarth
2. Gutachten: Prof. Dr. Oskar von Stryk

TECHNISCHE UNIVERSITÄT DARMSTADT

Fachbereich Humanwissenschaften

Bio-inspired Approaches for Human Locomotion: From Concepts to Applications
Biologisch inspirierte Ansätze für die menschliche Fortbewegung: Von Konzepten zur Anwendungen

Vorgelegte Dissertation von M.Sc. Guoping Zhao aus Huai'an, Jiangsu, P.R. China

1. Gutachten: Prof. Dr. André Seyfarth
2. Gutachten: Prof. Dr. Oskar von Stryk

Tag der Einreichung: 27 Juli 2019
Tag der Prüfung: 01 Oktober 2019

Darmstadt — D 17

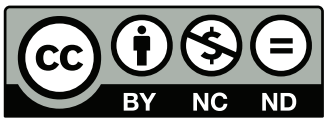

Erklärung zur Dissertation

Hiermit versichere ich, die vorliegende Dissertation ohne Hilfe Dritter nur mit den angegebenen Quellen und Hilfsmitteln angefertigt zu haben. Alle Stellen, die aus Quellen entnommen wurden, sind als solche kenntlich gemacht. Diese Arbeit hat in gleicher oder ähnlicher Form noch keiner Prüfungsbehörde vorgelegen.

Darmstadt, den 27.07.2019

(M.Sc. Guoping Zhao)

Zusammenfassung

Nach Millionen von Jahren der Evolution kann der Mensch in komplexen Umgebungen Fortbewegungsaufgaben mit vielseitigen, robusten und effizienten zweibeinigen Gangarten ausführen. Ein Verständnis über die dafür nötige Fortbewegungskontrolle kann uns helfen, neuartige biologisch inspirierte Methoden zur Verbesserung von Robotern mit Beinen (z. B. Humanoide) und tragbaren robotischen Systemen für die untere Extremität (z.B. Prothesen, Exoskelette) zu entwickeln.

Diese Dissertation untersucht systematisch biologisch inspirierte Ansätze von den Konzepten bis zur Anwendung, um die menschliche Fortbewegung besser zu verstehen. Sie umfasst drei Hauptteile: biomechanische Studien zu menschlichen Experimenten, die Modellierung der menschlichen Fortbewegung und die Hardware-Implementierungen von biologisch inspirierten Konzepten.

Die biomechanischen Studien liefern Einblicke in die menschlichen Bewegungskontrollsysteme. Die Bewegungssteuerung des Menschen kann in drei motorische Unterfunktionen unterteilt werden: den Stand (axiale Beinfunktion), das Schwingen (rotatorische Beinfunktion) und das Gleichgewicht (Haltungssteuerung). In der Arbeit wird untersucht, wie diese Unterfunktionen miteinander interagieren, indem wir den Beitrag von Stand- und Schwungbeinbewegungen zur Gehdynamik analysierten. Die Ergebnisse zeigen einen Kopplungsmechanismus und synergistische Wechselwirkungen zwischen den Teilfunktionen. Weitere experimentellen Daten zur menschlichen Ganginitiierung (vom Stehen bis zum Gehen) zeigen, dass die Funktionen des Schwungbeins und die des Standbeins beim ersten Schritt des Standbeins auftreten. Zudem hat sich gezeigt, dass eine starke Korrelation in den Gelenken zwischen der Kontrolle in der Frontalebene und der Sagittalebene existiert. Alle diese Ergebnisse zeigen, dass die Unterstützung einer Unterfunktion Vorteile für die anderen bietet.

Inspiriert von den Ergebnissen früherer biomechanischer Studien haben wir Strategien zur Kontrolle des Gleichgewichts, auf biologisch inspirierter Basis, in ein Gang-Exoskelett für die unteren Extremitäten implementiert. Diese Hardware-Implementierungen werden verwendet, um die Vorteile von biologisch inspirierten Steuerungskonzepten zu validieren und zu demonstrieren. Die Ergebnisse zeigen, dass der implementierte biologisch inspirierte Gleichgewichts-Controller nicht nur die Schwung- und Standbeinfunktion unterstützen, sondern auch die Stoffwechselkosten senken und damit das menschliche Gehen unterstützen kann. Die Ergebnisse stützen auch die früheren biomechanischen Studien, die auf synergistische Wechselwirkungen zwischen den Teilfunktionen hindeuten. Darüber hinaus haben wir einen bioinspirierten neuromuskulären Reflex-basierten Controller in einen Hüpfroboter implementiert, um die potenziellen Vorteile der Muskeleigenschaften für die Standbeinfunktion (elastischer Rückstoß) zu untersuchen. Die Ergebnisse zeigen, dass der Roboter mit dem bioinspirierten Controller ein stabiles und robustes Hüpfen erreichen kann. Weitere Analysen zeigen, dass die neuromuskulären Eigenschaften eine wichtige Rolle bei der Stabilisierung der Bewegung spielen. Diese Ergebnisse deuten darauf hin, dass Gangmodelle, welche Muskeleigenschaften und eine reflexartige Steuerung beinhalten, die Fortbewegung des Menschen besser reproduzieren können.

Die Modellierung der menschlichen Fortbewegung hilft uns, die biologisch inspirierten Konzepte in der Simulation zu testen und die Schlüsselkomponenten der menschlichen Fortbewegungssteuerung aufzudecken. Hier haben wir auf Basis der bisherigen Erkenntnisse ein komplexes neuromuskuläres

Gangmodell entwickelt, um ein personenspezifisches Gehverhalten zu erzeugen. Zur Erstellung der Kontrollrichtlinie (Sensor-Motor-Mappings), welche eine ähnliche Funktionalität wie die neuronalen Schaltkreise des menschlichen Rückenmarks aufweist, wurden Methoden des intensiven Verstärkungslernens (Deep reinforcement learning) verwendet. Die Ergebnisse zeigen, dass das Modell ein robustes Gehen erreichen und die Kinematik der Gelenke sowie die Aktivierung der Muskeln reproduzieren kann. Darüber hinaus haben wir auch festgestellt, dass die neuromuskuläre Dynamik das Lernen erleichtern kann. In Zukunft kann das vorgeschlagene Gangmodell verwendet werden, um optimale Steuerungsschemata für tragbare Roboter (z.B. Prothesen, Exoskelette) zu identifizieren.

Zusammenfassend wird in dieser Dissertation ein systematischer Ansatz vorgestellt, mit dem biologisch inspirierte Konzepte für die menschliche Fortbewegung durch experimentelle Studien zum menschlichen Gang, Simulationen und Hardwareimplementierungen untersucht werden. Der Hauptbeitrag dieser Arbeit besteht darin zu demonstrieren, wie die biologisch inspirierten Konzepte aus den experimentellen Daten des Menschen extrahiert, mit den Simulationsmodellen getestet und mit den Hardwaresystemen implementiert und validiert werden. Die Ergebnisse dieser Dissertation können als Rahmen für die Entwicklung neuartiger biologisch inspirierter Steuerungen zur Verbesserung der Funktionalität von Robotern mit Beinen (z.B. Humanoiden) und tragbaren Robotern (z. B. Prothesen, Exoskelette) verwendet werden.

Abstract

After millions of years of evolution, humans can achieve locomotion tasks in complex environments with versatile, robust and efficient bipedal gaits. Understanding human locomotion control systems can help us develop novel bio-inspired based methods for improving the current legged robots (e.g. humanoids) and wearable devices (e.g. prostheses, exoskeletons).

This thesis systematically explores the bio-inspired approaches from concepts to applications for further understanding human locomotion. It includes three main parts: biomechanical studies on human experiments, hardware implementations of bio-inspired concepts, and modeling of human locomotion.

The biomechanical studies provide insights on the human locomotor control systems. Human locomotion control can be separated into three locomotor subfunctions which are stance (axial leg function), swing (rotational leg function), and balance (posture control). We investigated how these subfunctions interact with each other by analyzing the contribution of stance and swing leg movements to the walking dynamics. The results reveal a coupling mechanism and synergistic interactions between the subfunctions. Further analyses on the human gait initiation (from standing to walking) experimental data demonstrate that the swing leg and stance leg functions are emerged during the first stride of the stance limb. And we find a strong correlation between the control of the frontal plane and the sagittal plane joints. All these results indicate that the support of one subfunction can provide benefits for the others.

Inspired by the findings from the previous biomechanical studies, we implemented bio-inspired balance control strategies on a lower-limb exoskeleton for human walking. The hardware implementations are used to validate and demonstrate the benefits of bio-inspired control concepts. The results show that the bio-inspired balance controller can not only support the swing and stance leg function but also reduce the metabolic costs and assist human walking. The results also support the prior biomechanical studies which suggest synergistic interactions between the subfunctions. In addition, we also implemented a bio-inspired neuromuscular reflex based controller for a hopping robot to investigate the potential benefits of the muscle properties for the stance (rebounding) leg function. The results demonstrate that the robot can achieve stable and robust hopping with the bio-inspired controller. Further analyses show that the neuromuscular properties play an important role in stabilizing the motion. These results indicate that gait models which include the muscle properties and reflex-like control could better reproduce human locomotion.

The modeling of human locomotion help us test the bio-inspired concepts in the simulation and reveal the key components of human locomotion control. Here, based on the previous findings, we developed a complex neuromuscular gait model to produce subject specific walking behaviors. Deep reinforcement learning methods were used to generate the control policy (sensor-motor mappings) which has similar functionality as human spinal cord neural circuitries. The results show that the model can achieve robust walking and closely reproduce human joint kinematics and muscle activations. In addition, we also found that the neuromuscular dynamics can facilitate the learning. In future, the proposed gait model can be used to identify optimal control schemes for wearable robots (e.g. prostheses, exoskeletons).

In summary, this thesis presents a systematic approach of investigating bio-inspired concepts for human locomotion by experimental studies of human gait, simulations, and hardware implementations.

The main contribution of this work is demonstrating how the bio-inspired concepts are extracted from the human experimental data, tested with the simulation models, and implemented and validated with the hardware systems. The outcomes of this thesis can be used as a framework to develop novel bio-inspired controllers for improving the performance of legged robots (e.g. humanoids) and wearable robots (e.g. prostheses, exoskeletons).

Contents

Contents 7

1 Introduction and motivation 11

References 13

2 Overview 17

3 Article I: Contribution of Stance and Swing Leg Movements to Human Walking Dynamics 21
3.1 Abstract . . . 22
3.2 Introduction . . . 22
3.3 Method . . . 22
3.3.1 Experiment . . . 23
3.3.2 Data pre-processing . . . 23
3.3.3 GRF component . . . 24
3.4 Results . . . 25
3.5 Discussions . . . 25
3.6 Future work . . . 27
3.7 Appendix . . . 27

References 28

4 Article II: The Mechanisms and Mechanical Energy of Human Gait Initiation: A Lower-limb Joint Level Perspective 31
4.1 Abstract . . . 32
4.2 Introduction . . . 32
4.3 Method . . . 33
4.3.1 Subjects . . . 34
4.3.2 Experimental setup . . . 34
4.3.3 Experimental protocol . . . 34
4.3.4 Data processing . . . 35
4.3.5 Statistics . . . 35
4.4 Results . . . 36
4.4.1 Gait initiation mechanism . . . 36
4.4.2 Energy injection during the gait initiation . . . 39
4.5 Discussion . . . 42
4.5.1 Joint positive power distributions . . . 42
4.5.2 Strategies for accelerating the CoM forward . . . 44
4.5.3 Balancing at the beginning of gait initiation . . . 45
4.5.4 The emergence of the walking pattern . . . 45

4.5.5 Future work . . . 45
4.6 Conclusion . . . 46
4.7 Appendix . . . 46
4.7.1 Mean CoM velocity . . . 46
4.7.2 Joint kinematics and kinetics during slow and fast GI . . . 46

References 49

5 Article III: Template Model Inspired Leg Force Feedback Based Control Can Assist Human Walking 53
5.1 Abstract . . . 54
5.2 Introduction . . . 54
5.3 Methods . . . 55
5.3.1 VPP concept based hip control . . . 55
5.3.2 Knee control . . . 56
5.3.3 Control implementation . . . 56
5.3.4 Experimental setup . . . 58
5.3.5 Experimental protocol . . . 58
5.3.6 Data processing . . . 60
5.4 Results . . . 60
5.4.1 Joint kinematics . . . 61
5.4.2 Muscle activation . . . 62
5.4.3 Metabolic cost . . . 62
5.5 Discussions and conclusions . . . 63

References 63

6 Article IV: Bio-inspired Balance Control Assistance Can Reduce Metabolic Energy Consumption In Human Walking 67
6.1 Abstract . . . 68
6.2 Introduction . . . 68
6.3 Methods . . . 70
6.3.1 Control concepts . . . 70
6.3.2 Implementation . . . 71
6.3.3 Experimental protocol . . . 73
6.3.4 Data processing . . . 74
6.3.5 Statistics . . . 74
6.4 Results . . . 75
6.4.1 Exoskeleton torque and power . . . 75
6.4.2 Joint kinematics . . . 76
6.4.3 Muscle activation . . . 76
6.4.4 Metabolic cost . . . 78

6.5 Discussions . . . 78
6.5.1 Joint kinematic patterns are preserved . . . 80
6.5.2 FMCH based controller is more efficient . . . 81
6.5.3 FMCH based controller has higher consistency in EMG responses . . . 81
6.5.4 Limitations . . . 82

References 83

7 Article V: Bio-inspired neuromuscular reflex based hopping controller for a segmented robotic leg 89
7.1 Abstract . . . 90
7.2 Introduction . . . 90
7.3 Robot Hardware Design and Simulation . . . 92
7.3.1 Mechanical design . . . 92
7.3.2 Control System Architecture . . . 93
7.3.3 Simulation . . . 94
7.4 Controller . . . 94
7.4.1 Muscular model . . . 94
7.4.2 Neural reflex . . . 96
7.4.3 Hopping control scheme . . . 97
7.4.4 MTU vs. simplified nonlinear spring . . . 98
7.4.5 Implementation . . . 98
7.5 Results . . . 99
7.5.1 Return maps . . . 99
7.5.2 Robustness of the FFB . . . 100
7.5.3 MTU vs. simplified nonlinear spring . . . 100
7.5.4 Robot hardware demonstration . . . 102
7.6 Discussion . . . 103
7.7 Appendix . . . 106

References 106

8 Article VI: A deep reinforcement learning based approach towards generating human walking behavior with a neuromuscular model 111
8.1 Abstract . . . 112
8.2 Introduction . . . 112
8.3 Methods . . . 113
8.3.1 Human experiments . . . 113
8.3.2 Modelling . . . 113
8.3.3 Deep-RL implementation . . . 114
8.3.4 Muscle dynamics and perturbation protocols . . . 116
8.3.5 Reward shaping . . . 117

8.4 Results . . . 119
8.4.1 Learned gait . . . 119
8.4.2 Muscle control vs torque control . . . 120
8.5 Discussions . . . 121
8.6 Conclusions . . . 124

References 125

9 Conclusion 129
9.1 Methodology for investigating bio-inspired concepts . . . 129
9.2 Synergies between locomotor subfunctions . . . 129
9.3 Bio-inspired leg force reflex based control can assist human walking . . . 130
9.4 Bio-inspired neuromuscular reflex based control for hopping robot . . . 130
9.5 Individualized gait modeling with reinforcement learning . . . 131
9.6 Outlook . . . 131

References 132

10 List of own publications 133

1 Introduction and motivation

The legged locomotion systems found in animals and humans can better adapt to rough terrains and complex environments than artificial wheeled and tracked robots (Raibert, 1986). Human-like bipedal locomotion is preferred especially for the indoor and outdoor environments which are designed for human daily livings. Therefore a lot of legged robots have been developed in the last few decades to mimic human gaits. For instance, the ASIMO robot can achieve bipedal walking, running and hopping motion (Hirose and Ogawa, 2007). And the Atlas robot can walk on uneven ground (Feng et al., 2016; Wiedebach et al., 2016) and can even generate gymnastic movements like back-flips [1]. Bipedal robots can be very useful in applications like reaching hazardous areas and fulfilling rescuing tasks which were promoted by the DARPA Robotics Challenge (Atkeson et al., 2018). Furthermore, the bipedal robot can also be used as a test platform for developing prostheses and exoskeletons if the behaviors of the robot are very close to the human behaviors. However, the performance of the state of art bipedal robots are still far away from humans in terms of stability, versatility and energetics (Seok et al., 2015). In order to improve the robot performance, we need to learn from the human locomotor systems and employ the learned bio-inspired approaches in the design and control of the robot.

The control of human locomotor systems is programmed in the central nervous system and modified by proprioceptive feedbacks (Dietz, 2002). It can be divide into three different levels. The first level is the preflex layer which is resulting from the muscle dynamics (e.g. muscle force-length and fore-velocity relationships) (Brown and Loeb, 2000). This defines the actuator (muscle) properties and shapes the human system dynamics. The mid-level is the spinal cord control layer which includes reflexes (e.g. muscle force, length and velocity feedbacks) and central pattern generators (CPGs) (Ijspeert, 2008; Song and Geyer, 2015). It has been shown that both reflex and CPGs based control can produce rhythmic muscle stimulation patterns and generate stable locomotion (Ijspeert, 2008; Bizzi et al., 2008; Geyer and Herr, 2010; Song and Geyer, 2015). The neural circuits in the spinal cord have high impacts on the behaviors of human periodic locomotion (e.g. walking and running gait) (Gerasimenko et al., 2008; Harkema et al., 2011). The high-level is the supraspinal control layer (located in the brain, including the brainstem and cerebellum area) which can modulate the control in the spinal cord layer (Duysens and de Crommert, 1998; Jahn et al., 2008).

In addition, the leg muscle morphology also contributes to the control of human locomotor systems. There are both monoarticular and biarticular muscles in the human leg. Biarticular muscles can transfer energy between different joints which can improve the energetics of human locomotion. It has also been found that the human biarticular thigh muscles are the key for controlling the direction of the ground reaction forces (Doorenbosch et al., 1995; Schenau, 1989). Based on these biomechanical findings, we implemented the biarticular muscle like actuators in a bipedal robot and demonstrated the benefits in decoupling the leg forces (in the axial and rotational direction of the leg) and the energetics (Sharbafi et al., 2016).

Although the human locomotor systems are quite complex, the fundamental characteristics of legged locomotion can be described with simplified template models (Full and Koditschek, 1999). For instance,

[1] Boston Dynamics, Atlas The World's Most Dynamic Humanoid, https://www.bostondynamics.com/atlas

by simplifying the stance leg to a prismatic spring and the whole body to a point mass, a spring loaded inverted pendulum (SLIP) model can generate both human-like walking and running gait (Blickhan, 1989; Geyer et al., 2006). Maus et al. (2010) extended the SLIP model with a trunk segment and showed that human-like posture control (trunk movements) can be achieved by regulating the hip torque based on the leg force (virtual pivot point concept, VPP). This VPP based controller can be approximated by a force modulated compliant hip (FMCH) concept which modulates the hip stiffness based on the leg force (Sharbafi and Seyfarth, 2015). Despite the high simplification, it has been shown that the template models can be used as guidelines for designing and controlling bipedal robots (Garofalo et al., 2012; Hubicki et al., 2016).

Human bipedal locomotion behaviors can be separated into three different levels: leg level which describes the overall leg (from the hip joint to the ground contact point) functions, joint level which describes the lower-limb joint functions (i.e. hip, knee and ankle joints), and the neuromuscular level which focuses on the muscle functions. These simple bio-inspired template models can help us further understand the basic principles of human locomotion. However, due to the simplification, most of them are at the leg function level. They cannot directly provide information regarding the joint and muscle functions which could be important for the design and control of prostheses and exoskeletons. Besides, all the current template models can only describe the basic patterns (e.g. the center of mass kinematics, leg forces, etc.) in steady state periodic locomotion. It is unclear how to adapt the conceptual model so that it can reproduce or predict the human responses in non-steady state conditions (e.g. gait transitions, perturbations, etc.). In addition, the capability of template models regarding reproducing human-like rich locomotion behaviors (e.g. pathological gaits, stair/slop climbing, etc.) is very limited.

On the other hand, one way to systematically analyze human legged locomotion is to look at three locomotor subfunctions which are balance (posture control), stance (axial leg function), and swing (rotational leg function) (Seyfarth et al., 2013). The balance subfunction is to keep the trunk upright and stable. The stance subfunction is to resist the gravity and support the body weight. The swing subfunction is to achieve ground clearance and target foot placement at the end of swing phase. These three locomotor subfunctions are working together to generate a certain gait. Sharbafi and Seyfarth (2017) have shown that the locomotor subfunctions can contribute to the walking speed adjustments. Investigating how different locomotor subfunctions interact with each other can help us further understand the human gaits and have a modular design and control of legged robots and exoskeletons.

Therefore, this thesis aims at using the locomotor subfunction concept to investigate and further understand human locomotion in both steady state and non-steady conditions. Kalveram and Seyfarth (2009) proposed an approach called test trilogy which includes simulation, hardware implementation and the behavior comparison to human experimental data. It is a method to test and verify if the bio-inspired concept is logically precise, physically sound and biologically relevant (Kalveram and Seyfarth, 2009). Inspired by the test trilogy, this thesis includes three parts: biomechanical studies on human experiments, simulations of human gaits, and hardware implementations of bio-inspired concepts.

In the next chapter, the overview of this thesis with summaries of each article is presented. Then the articles are presented in the following chapters. At the end, the conclusion and outlook of this thesis are presented.

References

Atkeson, C. G., Benzun, P. B., Banerjee, N., Berenson, D., Bove, C. P., Cui, X., DeDonato, M., Du, R., Feng, S., Franklin, P., et al. (2018). What happened at the darpa robotics challenge finals. In *The DARPA Robotics Challenge Finals: Humanoid Robots to the Rescue*, pages 667–684. Springer.

Bizzi, E., Cheung, V., d'Avella, A., Saltiel, P., and Tresch, M. (2008). Combining modules for movement. *Brain Research Reviews*, 57(1):125 – 133. Networks in Motion.

Blickhan, R. (1989). The spring-mass model for running and hopping. *Journal of Biomechanics*, 22(11–12):1217 – 1227.

Brown, I. E. and Loeb, G. E. (2000). *A Reductionist Approach to Creating and Using Neuromusculoskeletal Models*, pages 148–163. Springer New York, New York, NY.

Dietz, V. (2002). Proprioception and locomotor disorders. *Nature Reviews Neuroscience*, 3(10):781–790.

Doorenbosch, C. A., Harlaar, J., and van Ingen Schenau, G. J. (1995). Stiffness control for lower leg muscles in directing external forces. *Neuroscience Letters*, 202(1):61 – 64.

Duysens, J. and de Crommert, H. W. V. (1998). Neural control of locomotion; part 1: The central pattern generator from cats to humans. *Gait & Posture*, 7(2):131 – 141.

Feng, S., Xinjilefu, X., Atkeson, C. G., and Kim, J. (2016). Robust dynamic walking using online foot step optimization. In *2016 IEEE/RSJ International Conference on Intelligent Robots and Systems (IROS)*, pages 5373–5378.

Full, R. and Koditschek, D. (1999). Templates and anchors: neuromechanical hypotheses of legged locomotion on land. *Journal of Experimental Biology*, 202(23):3325–3332.

Garofalo, G., Ott, C., and Albu-Schäffer, A. (2012). Walking control of fully actuated robots based on the bipedal slip model. In *Robotics and Automation (ICRA), 2012 IEEE International Conference on*, pages 1456–1463.

Gerasimenko, Y., Roy, R. R., and Edgerton, V. R. (2008). Epidural stimulation: Comparison of the spinal circuits that generate and control locomotion in rats, cats and humans. *Experimental Neurology*, 209(2):417 – 425. Regeneration and Rehabilitation after Spinal Cord Injury.

Geyer, H. and Herr, H. (2010). A muscle-reflex model that encodes principles of legged mechanics produces human walking dynamics and muscle activities. *IEEE Transactions on neural systems and rehabilitation engineering*, 18(3):263–273.

Geyer, H., Seyfarth, A., and Blickhan, R. (2006). Compliant leg behaviour explains basic dynamics of walking and running. *Proceedings of the Royal Society of London B: Biological Sciences*, 273(1603):2861–2867.

Harkema, S., Gerasimenko, Y., Hodes, J., Burdick, J., Angeli, C., Chen, Y., Ferreira, C., Willhite, A., Rejc, E., Grossman, R. G., and Edgerton, V. R. (2011). Effect of epidural stimulation of the lumbosacral

spinal cord on voluntary movement, standing, and assisted stepping after motor complete paraplegia: a case study. *The Lancet*, 377(9781):1938 – 1947.

Hirose, M. and Ogawa, K. (2007). Honda humanoid robots development. *Philosophical Transactions of the Royal Society A: Mathematical, Physical and Engineering Sciences*, 365(1850):11–19.

Hubicki, C., Grimes, J., Jones, M., Renjewski, D., Spröwitz, A., Abate, A., and Hurst, J. (2016). Atrias: Design and validation of a tether-free 3d-capable spring-mass bipedal robot. *The International Journal of Robotics Research*.

Ijspeert, A. J. (2008). Central pattern generators for locomotion control in animals and robots: a review. *Neural networks*, 21(4):642–653.

Jahn, K., Deutschländer, A., Stephan, T., Kalla, R., Hüfner, K., Wagner, J., Strupp, M., and Brandt, T. (2008). Chapter 4.20 - supraspinal locomotor control in quadrupeds and humans. In Kennard, C. and Leigh, R. J., editors, *Using Eye Movements as an Experimental Probe of Brain Function*, volume 171 of *Progress in Brain Research*, pages 353 – 362. Elsevier.

Kalveram, K. T. and Seyfarth, A. (2009). Inverse biomimetics: How robots can help to verify concepts concerning sensorimotor control of human arm and leg movements. *Journal of Physiology-Paris*, 103(3):232 – 243. Neurorobotics.

Maus, H.-M., Lipfert, S. W., Gross, M., Rummel, J., and Seyfarth, A. (2010). Upright human gait did not provide a major mechanical challenge for our ancestors. *Nature communications*, 1(6):70.

Raibert, M. H. (1986). *Legged robots that balance*. MIT press.

Schenau, G. J. V. I. (1989). From rotation to translation: Constraints on multi-joint movements and the unique action of bi-articular muscles. *Human Movement Science*, 8(4):301 – 337.

Seok, S., Wang, A., Chuah, M. Y., Hyun, D. J., Lee, J., Otten, D. M., Lang, J. H., and Kim, S. (2015). Design principles for energy-efficient legged locomotion and implementation on the mit cheetah robot. *IEEE/ASME Transactions on Mechatronics*, 20(3):1117–1129.

Seyfarth, A., Grimmer, S., et al. (2013). Biomechanical and neuromechanical concepts for legged locomotion: Computer models and robot validation: Andre seyfarth, sten grimmer, daniel häufle, horst-moritz maus, frank peuker and karl-theodor kalveram. In *Routledge Handbook of Motor Control and Motor Learning*, pages 99–119. Routledge.

Sharbafi, M. A., Rode, C., Kurowski, S., Scholz, D., Möckel, R., Radkhah, K., Zhao, G., Rashty, A. M., von Stryk, O., and Seyfarth, A. (2016). A new biarticular actuator design facilitates control of leg function in BioBiped3. *Bioinspiration & Biomimetics*, 11(4):046003.

Sharbafi, M. A. and Seyfarth, A. (2015). FMCH: A new model for human-like postural control in walking. In *Intelligent Robots and Systems (IROS), 2015 IEEE/RSJ International Conference on*, pages 5742–5747.

Sharbafi, M. A. and Seyfarth, A. (2017). How locomotion sub-functions can control walking at different speeds? *Journal of Biomechanics*, 53:163 – 170.

Song, S. and Geyer, H. (2015). A neural circuitry that emphasizes spinal feedback generates diverse behaviours of human locomotion. *The Journal of physiology*, 593(16):3493–3511.

Wiedebach, G., Bertrand, S., Wu, T., Fiorio, L., McCrory, S., Griffin, R., Nori, F., and Pratt, J. (2016). Walking on partial footholds including line contacts with the humanoid robot atlas. In *2016 IEEE-RAS 16th International Conference on Humanoid Robots (Humanoids)*, pages 1312–1319.

2 Overview

This dissertation consists of six articles presented in separate chapters. Article I, III and IV are peer-reviewed and published/accepted papers. Information on each publisher and the original publication can be found at each chapter cover page. Article II, V and VI are submitted and currently under review. References of each chapter are listed at the end of the chapter. The following paragraphs summarize the content of each article.

Article I: Contribution of Stance and Swing Leg Movements to Human Walking Dynamics

This chapter presents an experimental study on human steady state walking. Here, we focuses on the question how the different locomotor subfunctions (i.e. stance leg, swing leg, and trunk movement) interact with each other during the single support phase. Template gait models assuming massless legs (e.g. models based on spring loaded inverted pendulum (SLIP) or inverted pendulum (IP) template) have been widely used to interpret human gaits. Although these models can describe basic gait features like center of mass (CoM) trajectories or ground reaction force (GRF) patterns, it is rather challenging to investigate swing leg function/control with these massless leg models. In this chapter, based on experiment data, we analyze how much swing leg, stance leg and upper body movement contribute to total GRF during single-support phase of walking. The results show that, in vertical direction, swing leg and upper body create in-phase M-shape force patterns, but stance leg does not contribute to the M-shape force pattern. In walking direction, the inertia forces created by swing and stance leg cancel each other out, while stance leg and upper body create similar inertia forces in both shape and magnitude. The results suggest that there is a phase locking mechanism for swing leg, stance leg and upper body movement. It can help to refine current conceptual models which better describe human walking.

This chapter investigates the swing and stance locomotor subfunction at the leg level. It indicates a coupling mechanism and synergistic interactions between the subfunctions. The next chapter focuses on how different locomotor subfunctions emerge during gait initiation from the lower-limb joint level perspective.

Article II: The Mechanisms and Mechanical Energy of Human Gait Initiation: A Lower-limb Joint Level Perspective

Instead of analyzing human behaviors during the steady state period gait, this chapter aims at further understanding the gait initiation (from standing to walking) mechanisms and the mechanical energy contributions from a lower limb joint perspective. In particular, we aimed at identifying mechanisms and energetic sources for increasing forward velocity and realizing the lateral weight shifting to keep balance. Additionally, we investigated how different locomotor subfunctions emerge during gait initiation.

Nine subjects (27.0 ± 4.2 years) without gait related impairments were instructed to initiate gait on an instrumented track to reach three self-selected target velocities: slow, normal and fast. Sagittal ankle, knee and hip and frontal hip kinematics and kinetics of the first five strides were analyzed. The results show that the initial lateral weight shift is achieved by the hip abduction torque on the lifting leg (leading limb). Before the take-off (TO) of the leading limb, the body forward movement is initiated by decreasing

the ankle plantarflexion torque, which results in an inverted pendulum-like passive forward falling. The hip (sagittal) has the highest positive mechanical energy output in the first stride of the leading limb, while the ankle joint contributes the most positive mechanical energy in the first stride of the trailing limb (stance leg). The vertical ground reaction forces and all joint kinetics show similar patterns as in the reference walking stride after the leading limb TO. All identified effects can be observed for all three gait initiation conditions (slow, normal, and fast).

Our results indicate a strong correlation between control of the frontal plane and the sagittal plane joints during gait initiation. This study presents unique insights on the weight shifting and energy injection mechanisms during gait initiation from the lower limb joint perspective. The identified mechanisms and the related data can be used as a guideline for improving gait initiation with wearable robots such as exoskeletons and prostheses.

Article III: Template Model Inspired Leg Force Feedback Based Control Can Assist Human Walking

In the previous two chapters we present biomechanical studies of human gait during both steady state and non-steady state walking in both leg level and joint level. In this and the next chapter, we investigate if it is feasible to implement the bio-inspired concepts observed from the human gait in a robotic system. The amount of research on developing exoskeletons for human gait assistance has been growing in the recent years. However, the control design of exoskeletons for assisting human walking remains unclear. Here, we present a novel template model inspired approach for assistive lower-extremity exoskeletons.

In particular, we implement a virtual pivot point (VPP) template model inspired leg force feedback based controller on a lower-extremity powered exoskeleton (LOPES II) and demonstrate that it can effectively assist humans during walking. It has been shown that the VPP template model is capable of stabilizing the trunk and reproduce a human-like hip torque during the stance phase of walking. With leg force and joint angle feedback inspired by the VPP template model, our controller provides hip and knee torque assistance during the stance phase. A pilot experiment was conducted with four healthy subjects. Joint kinematics, leg muscle electromyography (EMG), and metabolic cost were measured during walking with and without assistance. Results show that, for 0.6 m/s walking, our controller can reduce leg muscle activations, especially for the medial gastrocnemius (about 16.0%), while hip and knee joint kinematics remain similar to the condition without the controller. Besides, the controller also reduces 10% of the net metabolic cost during walking.

This paper demonstrates walking assistance benefits of the VPP template model for the first time. The support of human walking is achieved by a force feedback of leg force applied to the control of hip and knee joints. It can help us to provide a framework for investigating walking assistance control in the future.

Article IV: Bio-inspired Balance Control Assistance Can Reduce Metabolic Energy Consumption In Human Walking

The previous chapter investigated the bio-inspired leg force feedback controller with both hip and knee assistance for walking. The results showed that this approach is feasible to implement and can reduce both human metabolic costs and leg muscle activation. However, the individual contributions of hip and knee joint to the reductions are unclear. It also remains open whether a single joint (i.e. hip or knee

joints) bio-inspired assistance controller can reduce metabolic costs. Therefore, in this chapter, we focus on assisting only the hip joint.

This chapter presents a novel bio-inspired reflex-based control for assisting human walking. In this approach, the leg force is used as a feedback signal to adjust hip compliance. The effects of modulating hip compliance on walking gait is investigated through joint kinematics, leg muscle activations and overall metabolic costs for eight healthy young subjects. Reduction in the average metabolic cost and muscle activation are achieved with fixed hip compliance. Compared to the fixed hip compliance, improved assistance as reflected in more consistent reduction in muscle activities and more natural kinematic behavior are obtained using the leg force feedback. Furthermore, smoother motor torques and less peak power are two additional advantages obtained by compliance modulation. The results show that the proposed control method which is inspired by human posture control can not only facilitate the human gait, but also reduce the exoskeleton power consumption. This demonstrates that the proposed bio-inspired controller allows a synergistic interaction between human and robot.

Article V: Bio-inspired neuromuscular reflex based hopping controller for a segmented robotic leg

Previous chapters present the investigations of the human locomotor subfunctions in the leg and joint level. This and the following chapter focuses on the neuromuscular level. In this chapter, we present a low-cost robotic leg which is capable of dynamic locomotion (i.e. hopping) and demonstrate the bio-inspired neuromuscular reflex based controller with the robotic leg.

It has been shown that human-like hopping can be achieved by muscle reflex control in the neuromechanical simulations. However, it is unclear if this concept is applicable and feasible for controlling a real robot. This paper presents a low-cost two-segmented robotic leg design and demonstrates the feasibility and the benefits of the bio-inspired neuromuscular reflex based control for hopping. Simulation models were developed to describe the dynamics of the real robot. Different neuromuscular reflex pathways were investigated with the simulation model. We found that stable hopping can be achieved with both positive muscle force and length feedback. And the hopping height can be controlled by modulating the muscle force feedback gains with the return maps. The force feedback neuromuscular reflex based controller is robust against body mass and ground impedance changes. In order to investigate the influences of the muscle properties on the hopping behavior, the hopping height return map of a simplified muscle model was compared with the normal muscle model. The results show that the muscle properties play an important role in stabilizing the movement, highlighting the importance of morphological computation. Finally, we implemented the controller on the real robot to prove the feasibility of the proposed neuromuscular reflex based control idea. The results of this paper demonstrate the neuromuscular reflex based control approach is feasible to implement and capable of achieving stable and robust hopping in a real robot. It provides a promising direction of controlling the legged robot to achieve robust dynamic motion in the future.

Article VI: A deep reinforcement learning based approach towards generating human walking behavior with a neuromuscular model

Although different people share the general patterns during steady state locomotion, the responsive behaviors in perturbations (including adaptation to the wearable robots) can be quite subject dependent.

This has been shown by the results of Article III and IV. Because of the high simplifications in the body structure and the control, the capability of template models is very limited in terms of reproducing subject specific gait characteristics. A gait model capable of generating human-like walking behavior at both the kinematic and the muscular level can be a very useful framework for developing control schemes for humanoids and wearable robots such as exoskeletons and prostheses. Therefore, in this chapter, we aim at developing a gait model which capture the properties of the major leg muscle groups and the reflex based control.

In this work we demonstrated the feasibility of using deep reinforcement learning based approach for neuromuscular gait modeling. A lower limb gait model consists of seven segments, fourteen degrees of freedom, and twenty two Hill-type muscles was built to capture human leg dynamics and the characteristics of muscle properties. We implemented the proximal policy optimization algorithm to learn the sensory-motor mappings (control policy) and generate human-like walking behavior for the model. Human motion capture data, muscle activation patterns and metabolic cost estimation were included in the reward function for training. The results show that the model can closely reproduce the human kinematics and ground reaction forces during walking. It is capable of generating human walking behavior in a speed range from $0.6\,\mathrm{m/s}$ to $1.2\,\mathrm{m/s}$. It is also able to withstand unexpected hip torque perturbations during walking. We further explored the advantages of using the neuromuscular based model over the ideal joint torque based model. We observed that the neuromuscular model is more sample efficient compared to the torque model.

3 Article I: Contribution of Stance and Swing Leg Movements to Human Walking Dynamics

Authors:

Guoping Zhao and Andre Seyfarth

Lauflabor Locomotion Laboratory, TU Darmstadt, Darmstadt, Germany

Published as a paper in

ASSISTIVE ROBOTICS: Proceedings of the 18th International Conference on CLAWAR 2015. pages 224–231.

3.1 Abstract

Minimalistic gait models assuming massless legs (e.g. models based on spring loaded inverted pendulum (SLIP) or inverted pendulum (IP) template) have been widely used to interpret human gaits. Although these models can describe basic gait features like center of mass (CoM) trajectories or ground reaction force (GRF) patterns, it is rather challenging to investigate swing leg control strategies with these massless leg models. In this paper, based on experiment data, we analyse how much swing leg, stance leg and upper body movement contribute to total GRF during single-support phase of walking. The results show that, in vertical direction, swing leg and upper body create in-phase M-shape force patterns, but stance leg does not contribute to the M-shape force pattern. In walking direction, the inertia forces created by swing and stance leg cancel each other out, while stance leg and upper body create similar inertia forces in both shape and magnitude. The results suggest there is a phase locking mechanism for swing leg, stance leg and upper body movement. It can help to refine current conceptual models which better describe human walking.

Keywords

GRF contribution; swing leg; stance leg.

3.2 Introduction

Currently, two different minimalistic template models–spring loaded inverted pendulum (SLIP) (McMahon and Cheng, 1990; Blickhan, 1989) and inverted pendulum (IP) (McGeer, 1990)–are widely used for describing human gait pattern. A series of models (e.g. SLIP with trunk (Maus et al., 2010) or with curved foot (Hong et al., 2013), IP with ankle (Ahn and Hogan, 2012)) have been developed based on these two templates.

These massless leg models can describe several basic gait characteristics (Maus et al., 2014; Maus and Seyfarth, 2014; Pandy, 2003; Geyer et al., 2006), but they have some inherent drawbacks. First of all, in massless leg models, contributions from swing and stance leg inertia forces to GRF pattern are all attributed to stance leg function. Secondly, massless leg conceptual models cannot describe human locomotion with perturbations which require to accelerate limbs (consequently create a torque on the trunk) to keep balance. That is, accelerating limb masses can potentially help human to stabilize the trunk. In addition, it is quite challenging to investigate swing leg control strategies with massless leg models. For example, in order to stabilize a walking model, we can calculate the capture region based on the capture point concept (Pratt et al., 2006), but it is unclear how to control the swing leg properly so that the foot can reach the capture region in time without affecting trunk pitch stability considerably.

Thus, in order to find out the influence of swing and stance leg movements on human walking dynamics, here we investigate how much swing leg, stance leg, and upper body movement contribute to total GRF pattern based on experiment data of human walking at five different speeds.

3.3 Method

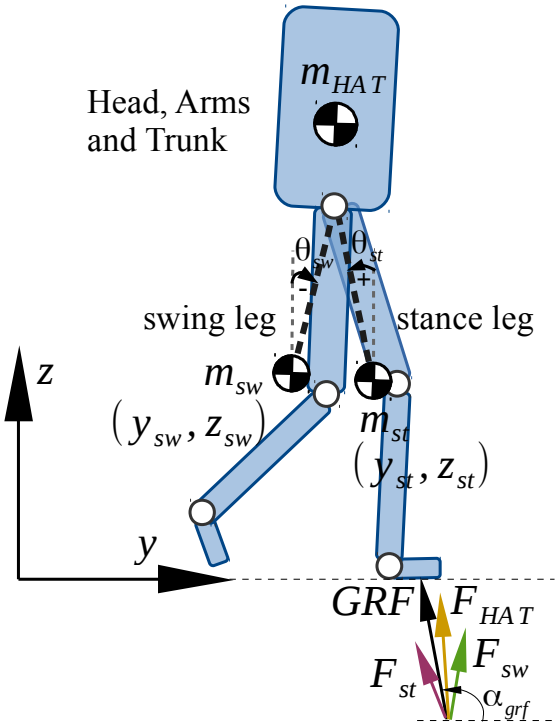

Figure 1: Seven-link model to investigate GRF components.

3.3.1 Experiment

Nine young healthy subjects (4 males, 5 females, age 24.8±2.3 years, body mass 71.7±12.7 kg, height 1.75±0.09 meters, preferred transition speed (PTS) from walking to running 2.06±0.13m/s) participated in the experiments. Subjects were instructed to walk on an instrumented treadmill (HEF Tecmachine, Andrezieux Boutheon, France). The belt speed was controlled at five different speeds (25%, 50%, 75%, 100% and 125% of each subject's PTS, that is, ∼0.5m/s, ∼1.0m/s, ∼1.5m/s, ∼2.1m/s and ∼2.6m/s). Three dimensional GRF data were collected by force sensors embedded in the treadmill (Kistler, Winterthur, Switzerland) at a frequency of 1kHz. Three dimensional kinematic data of lower limbs were collected by 8 high-speed cameras (Qualisys, Gothenburg, Sweden) at a frequency of 240Hz. Fifteen markers were used for each subject to capture the motion. Force and kinematic data were synchronized by a trigger signal provided by the treadmill. The time lag and time drift between the two systems are 2.5ms and 0.02ms/s. They were corrected after the measurements (Lipfert et al., 2009).

In order to get individual PTS, each subject was asked to walk on the treadmill based on a predefined speed curve (increase from 1.0m/s by 0.2m/s every 2 seconds until 3.0m/s, and then decrease in a same manner). After four trials, each subject chose a speed at which he/she felt most comfortable to switch the gait between walking and running. All subjects wore athletic shoes and had enough time for warming up and getting familiar with the measurements.

3.3.2 Data pre-processing

All data were processed using MATLAB (2014a, The MathWorks Inc., Natick, USA). GRF raw data were down sampled to 240Hz after filtered by a 49-51Hz bandstop and a 70Hz low-pass filter (zero-lag 4th

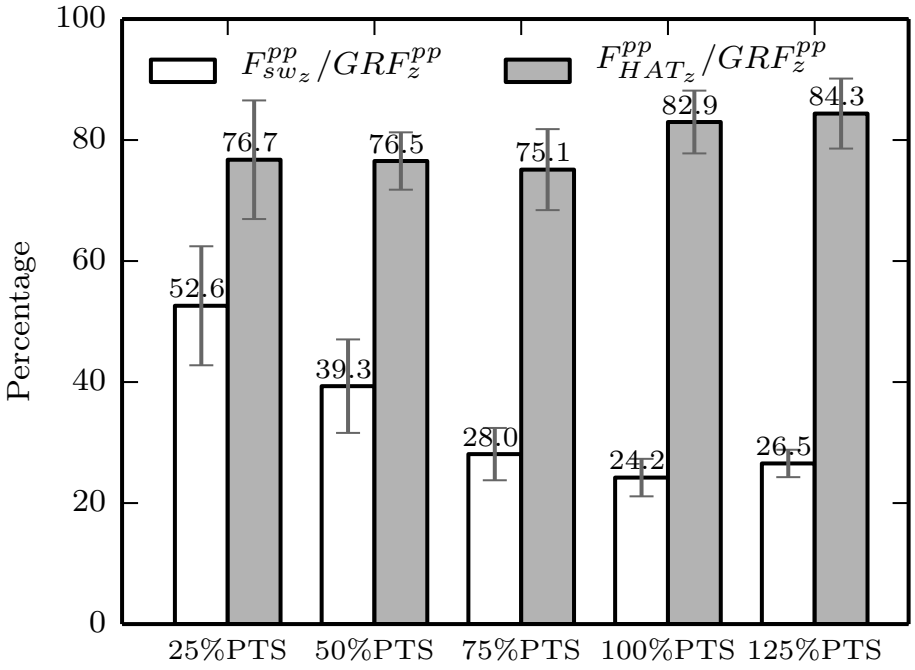

Figure 2: Means and standard deviations of nine subjests' peak-to-peak (pp) value of F_{sw_z} and F_{HAT_z} to GRF_z during single-support phase at five different walking speeds. The means are indicated by bars and the standard deviations by error bars. The subscript sw, HAT and z denote swing leg, head-arms-trunk, and vertical direction, respectively.

order Butterworth). The position data of all markers were filtered by a 40Hz zero-lag 4th order Butterworth low-pass filter. The velocity and acceleration of all markers were filtered by a 15Hz zero-lag 4th order Butterworth low-pass filter. Take-off (TO) moment was defined as the moment when the decreasing vertical GRF crosses 10N. Touch-down (TD) moment was defined, in the same way, as the moment when the increasing vertical GRF crosses 10N. In total, 1284 gait cycles were separated and analysed in this paper.

3.3.3 GRF component

As shown in Fig. 1, GRF can be divided into three parts:

$$\begin{aligned}\mathbf{GRF} =& \mathbf{F}_{sw} + \mathbf{F}_{st} + \mathbf{F}_{HAT} \\ =& m_{leg}\begin{bmatrix}\ddot{y}_{sw}\\ \ddot{z}_{sw}+g\end{bmatrix} + m_{leg}\begin{bmatrix}\ddot{y}_{st}\\ \ddot{z}_{st}+g\end{bmatrix} + m_{HAT}\begin{bmatrix}\ddot{y}_{HAT}\\ \ddot{z}_{HAT}+g\end{bmatrix}\end{aligned} \tag{1}$$

where the subscripts sw, st and HAT indicate swing leg, stance leg and upper body (head-arms-trunk), respectively; m_{leg} is leg mass; g is the gravity acceleration; $(y,z)^T$ denote the position of the segment center of mass (CoM), y-axis and z-axis denote walking direction and vertical direction, respectively. In this paper, based on cadaver studies (Winter, 2009), CoM accelerations of two legs and HAT were calculated by the movement of markers attached on limbs and GRF. See Appendix for more details.

3.4 Results

For preferred walking speed (75% PTS, around 1.5m/s), Fig. 2 shows that the ratio of $F^{pp}_{HAT_z}$ to GRF^{pp}_z is about 75.1%, which means that the swing leg dynamics explain about 24.9% of the typical M-shaped GRF variation (because F_{st_z} keeps almost constant, Fig. 3). For slow walking speeds (25% and 50% PTS), swing leg can explain about 23%. For fast walking speeds (100% and 125%PTS), the ratios of $F^{pp}_{HAT_z}$ to GRF^{pp}_z are higher than preferred walking speed (around 83∼84%). $F^{pp}_{sw_z}/GRF^{pp}_z$ is higher at low walking speeds (52.6% at 25%PTS, 39.3% at 50%PTS) than at preferred walking speed (28%).

Fig. 3 shows that in vertical direction, the force contribution created by upper body is dominant for the GRF at all speeds. Surprisingly, swing leg also contributes to the characteristic M-shape force pattern in walking in contrast to stance leg. For all speeds, F_{sw_z} has a similar M-shape pattern to GRF_z: one peak at the early and one peak at the late of single-support phase, but F_{st_z} keeps almost constant (about leg weight, except for the early single-support phase of 100%, and 125% PTS). In walking direction, as shown in Fig. 3, the forces created by the movement of stance leg (F_{st_y}) and HAT (F_{HAT_y}) are similar to each other in both magnitude and shape. In contrast, the GRF contribution of swing leg (F_{sw_y}) has a similar shape and magnitude as F_{st_y} but is opposite in direction. The direction of force contribution created by HAT is almost the same as the GRF direction (Fig. 3). The forces caused by accelerations of both legs do not have a strong influence on total GRF direction.

3.5 Discussions

The motivations of this study was to understand the effect of leg movement on the dynamic behavior of human walking during single-support phase. In order to achieve this, we analysed the contributions of stance leg, swing leg and upper body movements to total GRF at five different walking speeds based on experimental data. The results suggest the phase locking mechanism among stance leg, swing leg and HAT. For example, in vertical direction, the swing leg inertia force has an in-phase M-shape pattern with respect to HAT inertia force and GRF, but stance leg inertia force does not have a pronounced similar M-shape pattern.

In vertical direction, although the force created by HAT is dominant at all walking speeds, which agrees with the assumption of point mass models, swing leg also contribute to M-shape force patterns (Fig. 3). In SLIP model, the M-shape of GRF is just attributed to the axial compliance of stance leg. Here we see that the swing leg contributes to this stance leg function. For example, $F^{pp}_{sw_z}$ is about 39.3% of GRF^{pp}_z at 50%PTS (around 1.0m/s, Fig. 2). In addition, the virtual leg length of swing leg also has a similar M-shape comparing to F_{sw_z}. This suggests to use a spring loaded pendulum model to mimic the swing leg dynamics.

At low speed walking (25% and 50%PTS), F_{st_z} is almost constant and equal to leg weight during whole single-support phase. This agrees with the IP model which assumes a rigid stance leg. But for preferred and high speed walking (75% to 125%PTS), F_{st_z} has a pronounced peak at the beginning of single-support phase. In this case, the stance leg is more like a mass spring damper system, which could absorb landing impacts.

From the force patterns in walking direction (Fig. 3) we can find that the swing leg and stance leg are coupled. The forces generated by two legs cancel each other out during the single-support phase. This effect was previously found in the M-SLIP model (Peuker et al., 2012). From the trunk stabilization

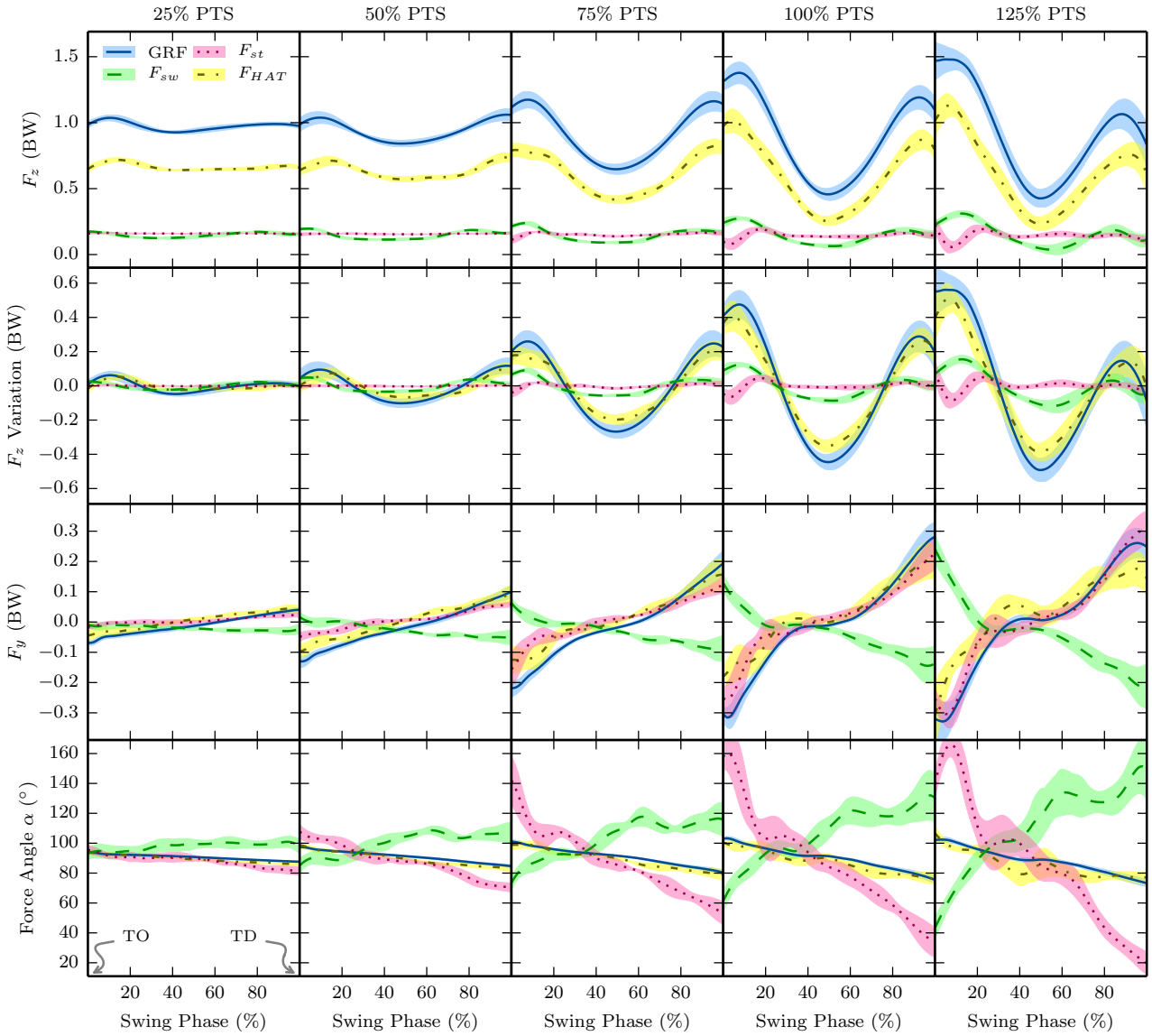

Figure 3: GRF components. F_z and F_y denote the force in vertical and walking direction. F_{sw}, F_{st} and F_{HAT} denote the force caused by swing leg, stance leg and HAT (head, arms and trunk) dynamics, respectively. All forces are normalized by body weight (BW). TO and TD denote take-off and touch-down, the beginning and end of single-support phase. Bands on each waveform indicate the standard derivation (±SD).

point of view, the coupling effect of two legs could simplify the upper body control. It has been widely observed that there is a high peak power output from the ankle joint during push-off in order to generate enough speed to swing the leg forward (Lipfert et al., 2013). Thus, stance leg dynamics have a strong impact for the initiation of swing phase at push-off. On the other hand, swing leg dynamics also have a strong impact at touch-down. With the coupling mechanism of two legs, impact on one leg could mainly just affect the movement of the other leg rather than the trunk.

3.6 Future work

In this paper we found that swing and stance leg have significantly different behaviors in both vertical and walking direction. A next step could be to analyse the double stance phase to understand the transition between swing leg and stance leg. And based on the results of this paper, it becomes possible to build more realistic conceptual walking models which could better describe the swing leg and upper body balance control strategies.

Acknowledgment

This work was supported by the EU project BALANCE under Grant Agreement No. 601003. The authors would like to thank Susanne W. Lipfert for conducting the experiments. We are very thankful to Maziar A. Sharbafi for helpful advice and discussions.

3.7 Appendix

According to the anthropometric data given by Winter (2009), leg CoM position was calculated by the positions of markers which are attached on hip/greater trochanter, knee, ankle/lateral malleolus, and 2nd metatarsal, respectively. Leg CoM velocity and acceleration were calculated by differentiating the position data. There are two ways to calculate $\mathbf{F}_{HAT}$:

1. Calculate HAT CoM acceleration based on the markers attached on trunk (greater trochanter and glenohumeral joint) and arms (elbow and wrist joint). This method assumes the trunk is rigid, which neglects e.g. spine compliance and wobbling mass effects.

2. Calculate $\mathbf{F}_{HAT}$ by subtracting $\mathbf{F}_{sw}$ and $\mathbf{F}_{st}$ from **GRF** (measured by force plates). This method avoids the error of estimating trunk CoM acceleration by trunk markers' positions. But it introduces the error of $\mathbf{F}_{sw}$ and $\mathbf{F}_{st}$ from **GRF** to $\mathbf{F}_{HAT}$.

In order to check whether the calculation method of $\mathbf{F}_{HAT}$ affects the results a lot, we calculated F_{HAT_z} at normal walking speed (75%PTS) in both methods (Fig. 4). Fig. 4 shows that although the error at the beginning and end of swing phase is a little bit high, the whole shape of two curves do not change a lot. In over 95% of swing phase the error is lower than 5% of body weight. Because the shape of $\mathbf{F}_{HAT}$ is not sensitive to the method, in this paper, $\mathbf{F}_{HAT}$ is calculated by the second method (subtracting force leg forces).

Author contributions

Guoping Zhao is the main and corresponding author of this paper. He was responsible for the conception and design, analysis and interpretation of data and writing of the manuscript. Andre Seyfarth was the

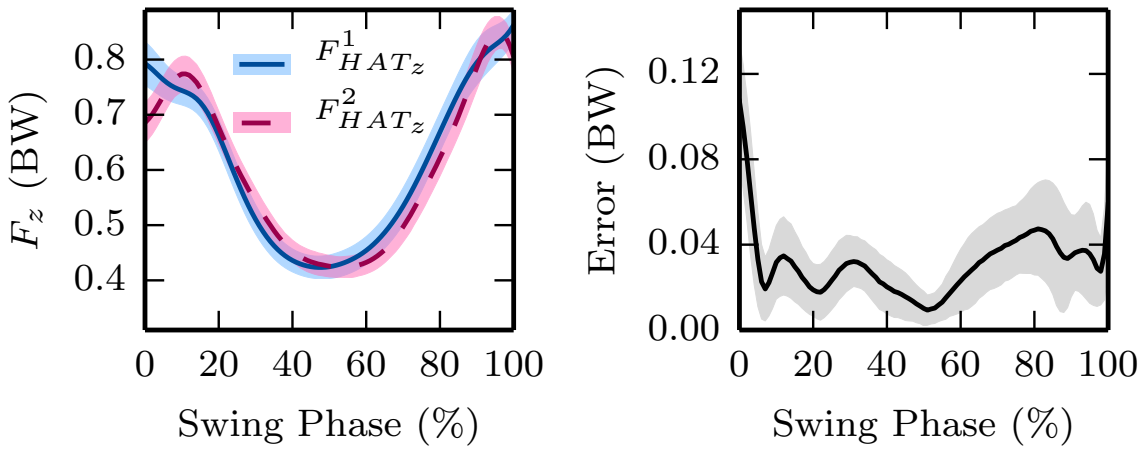

Figure 4: Comparison of two methods. $F^1_{HAT_z}$ and $F^2_{HAT_z}$ denote the force calculated by first (marker positions) and second (subtracting leg forces) method, respectively. The error shows the difference between $F^1_{HAT_z}$ and $F^2_{HAT_z}$.

supervisor of the project and contributed to develop the concept and revise the manuscript.

References

Ahn, J. and Hogan, N. (2012). A simple state-determined model reproduces entrainment and phase-locking of human walking. *PLoS ONE*, 7(11):e47963.

Blickhan, R. (1989). The spring-mass model for running and hopping. *Journal of Biomechanics*, 22(11–12):1217 – 1227.

Geyer, H., Seyfarth, A., and Blickhan, R. (2006). Compliant leg behaviour explains basic dynamics of walking and running. *Proceedings. Biological sciences / The Royal Society*, 273(1603):2861–7.

Hong, H., Kim, S., Kim, C., Lee, S., and Park, S. (2013). Spring-like gait mechanics observed during walking in both young and older adults. *Journal of Biomechanics*, 46(1):77 – 82.

Lipfert, S., Günther, M., Renjewski, D., and Seyfarth, A. (2013). Impulsive ankle push-off powers leg swing in human walking. *The Journal of Experimental Biology*.

Lipfert, S. W., Günther, M., and Seyfarth, A. (2009). Diverging times in movement analysis. *Journal of Biomechanics*, 42(6):786 – 788.

Maus, H.-M., Lipfert, S. W., Gross, M., Rummel, J., and Seyfarth, A. (2010). Upright human gait did not provide a major mechanical challenge for our ancestors. *Nature communications*, 1(6):70.

Maus, H.-M., Revzen, S., Guckenheimer, J., Ludwig, C., Reger, J., and Seyfarth, A. (2014). Constructing predictive models of human running. *Journal of The Royal Society Interface*, 12(103).

Maus, H.-M. and Seyfarth, A. (2014). Walking in circles: a modelling approach. *J. R. Soc. Interface*, 11(20140594).

McGeer, T. (1990). Passive dynamic walking. *The International Journal of Robotics Research*, 9(2):62–82.

McMahon, T. and Cheng, G. (1990). The mechanics of running - how does stiffness couple with speed. *Journal of Biomechanics*, 23(1):65–78.

Pandy, M. G. (2003). Simple and complex models for studying muscle function in walking. *Philosophical Transactions of the Royal Society of London. Series B: Biological Sciences*, 358(1437):1501–1509.

Peuker, F., Seyfarth, A., and Grimmer, S. (2012). Inheritance of slip running stability to a single-legged and bipedal model with leg mass and damping. In *Biomedical Robotics and Biomechatronics (BioRob), 2012 4th IEEE RAS EMBS International Conference on*, pages 395–400.

Pratt, J., Carff, J., Drakunov, S., and Goswami, A. (2006). Capture point: A step toward humanoid push recovery. In *Humanoid Robots, 2006 6th IEEE-RAS International Conference on*, pages 200–207.

Winter, D. A. (2009). *Biomechanics and Motor Control of Human Movement*. John Wiley & Sons, Hoboken, NewJersey USA, fourth edition.

4 Article II: The Mechanisms and Mechanical Energy of Human Gait Initiation: A Lower-limb Joint Level Perspective

Authors:

Guoping Zhao, Martin Grimmer, and Andre Seyfarth

Lauflabor Locomotion Laboratory, TU Darmstadt, Darmstadt, Germany

Submitted for publication in 2019

4.1 Abstract

This study aims at further understanding the gait initiation mechanisms and the mechanical energy contributions from a lower-limb joint perspective. Healthy subjects were instructed to initiate gait on an instrumented track to reach three self-selected target velocities: slow, normal and fast. Lower-limb joint kinematics and kinetics of the first five strides were analyzed. The results show that the initial lateral weight shift is achieved by the hip abduction torque on the lifting leg (leading limb). Before the take-off (TO) of the leading limb, the body forward movement is initiated by decreasing the ankle plantarflexion torque, which results in an inverted pendulum-like passive forward falling. The hip flexion/extension joint has the highest positive mechanical energy output in the first stride of the leading limb, while the ankle joint contributes the most positive mechanical energy in the first stride of the trailing limb (stance leg). Our results indicate a strong correlation between control of the frontal plane and the sagittal plane joints during gait initiation. The identified mechanisms and the related data can be used as a guideline for improving gait initiation with wearable robots such as exoskeletons and prostheses.

4.2 Introduction

Adults typically walk between 6000 and 13000 steps per day (Tudor-Locke and Bassett Jr, 2004). Next to longer episodes of walking there are many short episodes where transitions between the stable state of standing and the dynamically stable state during walking are required. Besides keeping balance during transitions, the gait termination has to dissipate energy while the gait initiation has to inject energy to the body segments.

Gait initiation could be challenging for human balance control system as it moves from static standing balance to dynamic periodic walking balance (Halliday et al., 1998). For instance, patients with Parkinson's disease often have difficulties in initializing walking from standing (Bloem et al., 2004; Nutt et al., 2011). From the lower-limb muscle activation perspective, gait initiation starts with an abrupt decrease in the soleus and gastrocnemius muscle activation and increase in the tibialis muscle activation on the stance limb (Brunt et al., 1991, 1999; Crenna and Frigo, 1991; Elble et al., 1994).

Several studies have also investigated the center of mass (CoM) and center of pressure (CoP) movements during gait initiation. For instance, Jian et al. (1993) described the gait initiation process as following: To start gait initiation the CoP moves rapidly posteriorly and towards the swing limb to accelerate the CoM forward and towards the stance limb. Then, the swing limb is unloaded and the CoP moves towards the stance foot, creating an acceleration forward. Before the touch down of the swing foot, the CoM has already established a near steady-state trajectory. However, it remains unclear how lower-limb joints contribute to the mechanism of shifting the CoM and CoP.

Based on inverse dynamics, lower-limb joint mechanical power and energy have been used to explain walking energetics (Farris and Sawicki, 2011; Umberger and Martin, 2007). For level walking the average positive and negative power of the hip, knee and ankle are increasing with increasing velocity (Farris and Sawicki, 2011). Similarly joint work and peak power are increasing (Grimmer et al., 2014). In contrast, the relative contribution of total average positive power for each lower-limb joint stays at an equal level (Farris and Sawicki, 2011). For instance, the hip and the ankle provide the major energy injection (about 40%) during walking at velocities of 0.75 m/s to 2.0 m/s (Farris and Sawicki, 2011). For gait initiation, Hansen et al. (2010) analyzed the ankle energy contribution and demonstrated that the ankle net positive

work increases with increasing gait initiation target velocity. To date, no study has shown the lower-limb joint mechanical power and energy contribution during gait initiation of different target velocities.

This study aims at providing further understanding of the energy sources and processes that are used during gait initiation to create and increase the CoM forward velocity. The analysis includes the local joint level as well as the global CoM behavior. We expect that humans use a combination of specific energy injection strategies to achieve a target velocity including a) a dominant role of specific joints to inject energy, b) transfer from potential to kinetic energy, and c) avoiding of energy dissipation. Further, we expect that there are d) actively controlled weight shifting balance mechanisms mediating between the frontal and the sagittal plane in order to organize the energy injection.

Farris and Sawicki (2011) found that different walking velocities have a similar relative contribution of total average hip, knee and ankle positive power. In order to study the target velocity related effects on the joint contributions during gait initiation, three different target velocities were analyzed in this study. We expect that, in line with the findings of Farris and Sawicki (2011), relative energetic joint contributions and the balance mechanisms do not change with target velocity. We explain our expectations in more detail below.

Firstly, in continuous level walking the hip and the ankle joint contribute similar amount of positive work while the knee contributes less than half of the hip or the ankle (Farris and Sawicki, 2011). We want to investigate if this relationship is also existing during gait initiation. More specifically, we focus on investigating if there are specific joints that primarily drive the leading and the trailing limb in the initiation stride as well as the following strides to reach the target velocity. It is hypothesized that, in order to swing the leg forward, the hip in the leading limb contributes more during the first initiation stride compared to steady state walking. For the following strides, we expect a relative contribution of all joints similar to steady state walking with major positive work contributions of the hip and ankle.

Secondly, two major energy sources for the increase of CoM kinetic energy are expected: 1) lower-limb joint positive work, and 2) CoM potential energy. We hypothesized that the potential energy contributes the most to the CoM kinetic energy for the first stride, whereas for the following acceleration strides the positive joint work dominates.

Thirdly, next to energy injection during gait initiation, reducing energy dissipation could be an energy efficient strategy for acceleration. It is hypothesized that the CoM mechanical collision and preload work are reduced compared to regular walking but increase with increasing walking velocity.

Lastly, at the beginning of gait initiation, the CoM initially shifts towards the trailing limb (Jian et al., 1993; Yiou et al., 2017). To investigate on the mechanism of the shift, we focus on joints contributing to lateral sway. There are two main mechanisms that could initiate the lateral shifting of the CoM: 1) hip abduction torques on the leading limb side and/or hip adduction torques on the trailing limb side; 2) elongating the leading limb (e.g. ankle dorsiflexion) and/or shortening the trailing limb (e.g. knee flexion). As elongating or shortening the leg might conflict with the initiation of sagittal plane movement, we expect that it is easier to achieve the CoM shifting with hip abduction or adduction. We hypothesized that it is primarily accomplished by the hip abduction on the leading limb because hip exerts also large abduction torque during the stance phase of regular walking (Houck et al., 2006).

4.3 Method

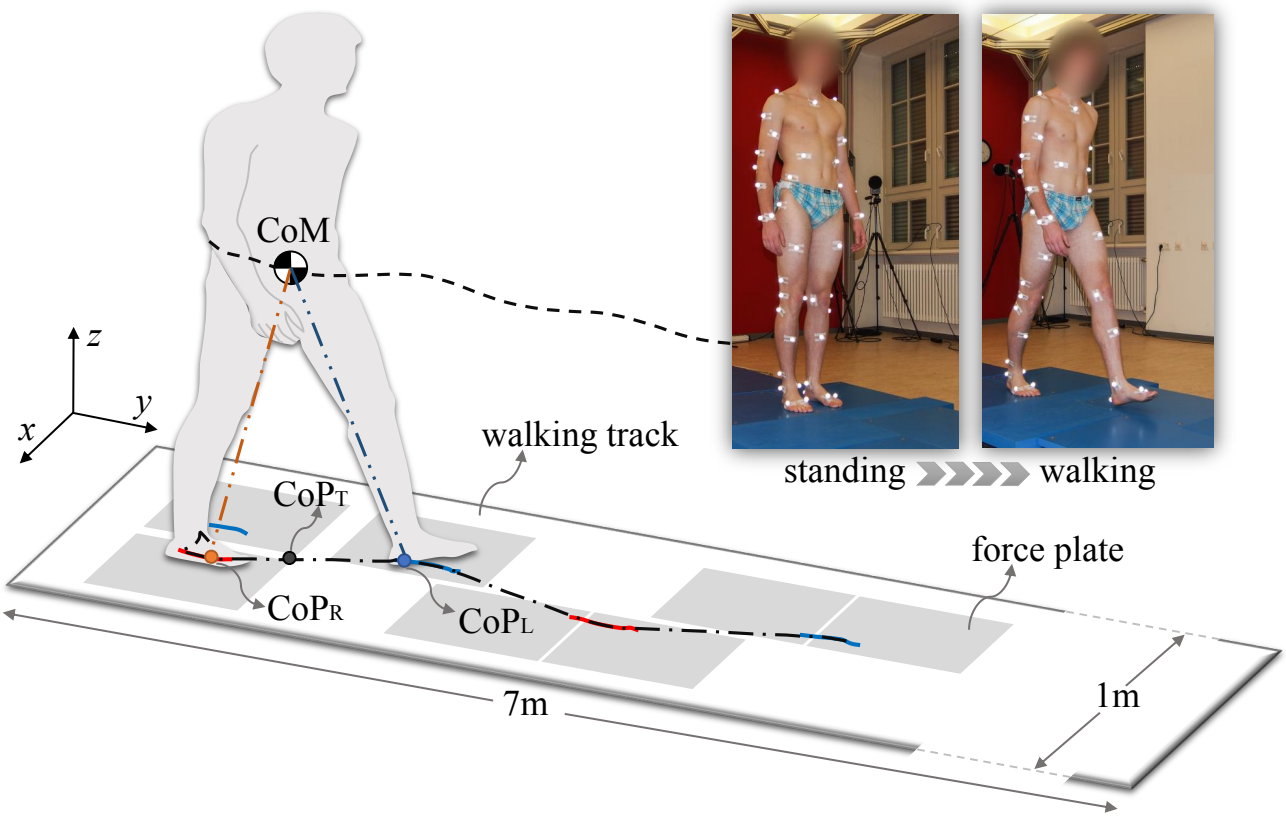

Figure 1: Experimental setup overview. CoP_L, CoP_R, and CoP_T denote the left leg, right leg, and total center of pressure, respectively.

4.3.1 Subjects

Nine young healthy subjects (one female, eight males, age 27.0±4.2 years, body mass 74.2±9.2 kg, height 1.83±0.06 m, mean ± std.) were enrolled in this study. Subject body height was restricted between 1.7 m and 2.0 m because of the step length limitation from the force plate setup (Fig. 1). All subjects were healthy without any neuromuscular injury or functional impairment. The study was approved by the Ethics Committee of TU Darmstadt. All subjects gave informed consent.

4.3.2 Experimental setup

A 7 m long, 1 m wide flat walking track was construct for this experiment (Fig. 1). Seven force plates (five 9260AA and two 9287C, Kistler, Switzerland) were firmly mounted on a metal frame and embedded in the track. Ground reaction forces (GRF) were recorded at 1 kHz. The force plate positions were carefully arranged so that they can measure the GRFs of each leg during standing and the first three strides for the gait initiation trails. A 3D motion capture system (ten high-speed cameras, model Qqus, Qualisys, Sweden) recorded full body kinematics from 51 reflective markers at 500 Hz.

4.3.3 Experimental protocol

Before data collection, subjects performed several different walking trials to 1) warm up and familiarize with the setup, 2) test whether their step length was too large or too small for the setup, 3) determine the appropriate starting locations where the first three strides GRFs can be collected. Then, walking

trials (8 repetitions) with preferred velocity were conducted on the track. Subjects were instructed to start walking at least 3 m before he/she stepped on the first force plate. For gait initiation trials, subjects were instructed to stand as still as possible on the first two force plates. Then after an auditory cue, subjects started walking at any time with three different self-selected target velocities (slow, normal, and fast, 8 repetitions for each velocity). Subjects always started walking with left leg due to the force plate arrangement. All experiments were conducted barefoot.

4.3.4 Data processing

The beginning of initiation was defined as the moment when the displacement between the CoP and the CoM in walking direction is larger than 2 cm. The vertical GRF was used for detecting the touch-down (TD) and the take-off (TO) event. Gait initiation trial data were separated into standing, L1, R1, L2, R2 and L3 (as shown in Fig. 2). Standing was defined from the beginning of the experiment till the beginning of initiation. L1 and R1 were defined from the beginning of initiation till the first TD of the left and right leg, respectively. L2, R2 and L3 were defined as the following the second left, second right, and third left stride, respectively. Each stride is defined from TD to TD of the same leg (Fig. 2).

The marker based total body CoM position was calculated using maker positions from all body segments and the anthropomorphic data (Winter, 2009). Three dimensional total body CoM positions and velocities were computed by combining both marker based CoM position and GRFs using the method from (Maus et al., 2011). CoM power for the left and the right leg was calculated as the dot product of CoM velocity and the left and right GRFs, respectively. The hip, knee and ankle kinematics and kinetics were computed with the open-source OpenSim software (version 3.3) (Delp et al., 2007) using a full body model adapted from Hamner et al. (2010). Joint kinetics data were normalized to the individual subject body mass. GRFs were normalized to the individual subject body weight. Joint net, positive and negative work during each stride (e.g. L1, R1, L2 etc.) were calculated by integrating the joint power over one stride period, positive power period, and negative power period, respectively. Average joint positive and negative power were calculated by the joint positive and negative work divided by the stride period, respectively (Farris and Sawicki, 2011). The average CoM power were calculated using the individual limb method (Donelan et al., 2002).

All data were processed with Matlab (R2018b, MathWorks) scripts.

4.3.5 Statistics

In this paper we present the results of the statistical analyses of average CoM power and the average joint power (both positive and negative power) during each stride. The Jarque-Bera test was used for checking if the data were normally distributed in each condition. If the data were normally distributed, a one-way repeated measures analysis of variance (ANOVA) was performed across three conditions (i.e. slow, normal and fast target velocity gait initiation). Otherwise, the nonparametric Friedman test was performed. The Mauchly test was used to evaluate sphericity. The Greenhouse-Geiser correction was applied if the sphericity assumption was violated. If the repeated measures ANOVA or the Friedman test indicated a significant effect, the paired t-test was used for *post hoc* tests. The paired t-test was performed between each individual stride during gait initiation and the steady state condition stride. The comparison was performed for the average positive joint power, the average negative joint power,

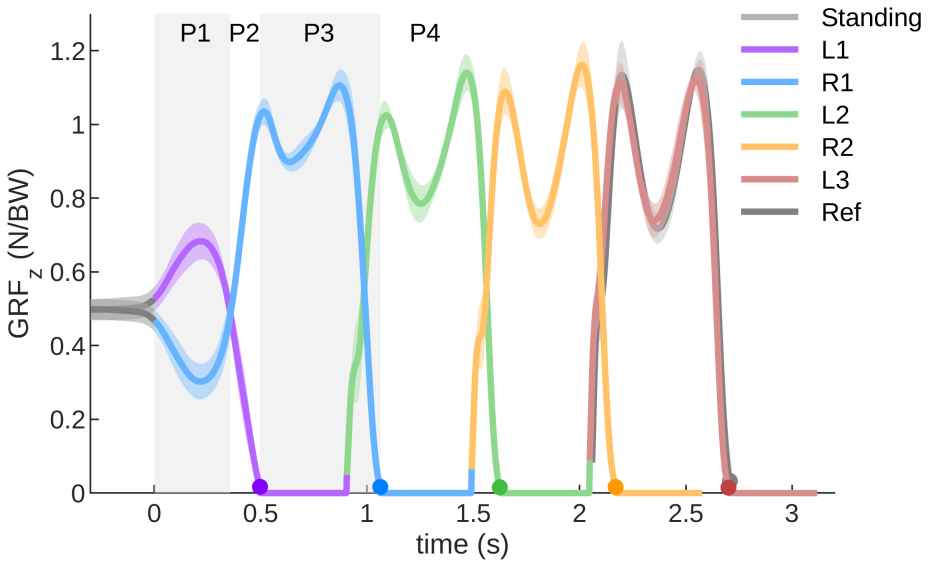

Figure 2: Vertical GRF (GRF_z) during the normal gait initiation. GRF_z is normalized to subject body weight (BW). The solid lines denote the average GRF_z over ten subjects. The error bands denote the ± 1 standard deviation. Different colors denote different strides. Time 0 is defined as the starting of the gait initiation. The dots denote the take-off moment. P1: weight shifting initiation phase; P2: leading limb lifting initiation phase; P3: trailing limb push-off phase; P4: stabilizing phase.

and the CoM power. A statistical difference was considered at a level of $p < 0.05$. A single asterisk (*) and a double asterisks (**) indicate the significant difference of $p < 0.05$ and $p < 0.01$ with respect to the reference (Ref), respectively. All statistical tests were conducted in Matlab (R2018b, MathWorks).

4.4 Results

The results section consists of two subsections. First, the mechanism of the gait initiation is introduced based on the joint level and the CoM data. The second subsection focuses on the energy injection from the average CoM power and each lower-limb joint.

4.4.1 Gait initiation mechanism

We separate the gait initiation process into the following four different phases.

Weight shifting initiation phase (P1)

The weight shifting initiation is defined from the beginning of gait initiation (see Methods) to the beginning of the hip flexion, which occurs with the instance of equal vertical ground reaction force values of L1 and R1. During the weight shifting phase the CoM is shifted forward and at the same time laterally towards the trailing limb (Fig. 3). To realize the lateral shift, the hip of the leading limb exhibits an abduction torque (Fig. 4). With this increasing hip torque, we observe an instantaneous increase in the vertical GRF of the leading limb and a decrease in the trailing limb (L1 and R1 in Fig. 2). The timing of vertical GRF peak of L1 and R1 (negative), and the peak of the L1 hip abduction torque are aligned. At the trailing limb, the vertical GRF decreases while the hip, knee and ankle joints are flexing (Fig. 2,

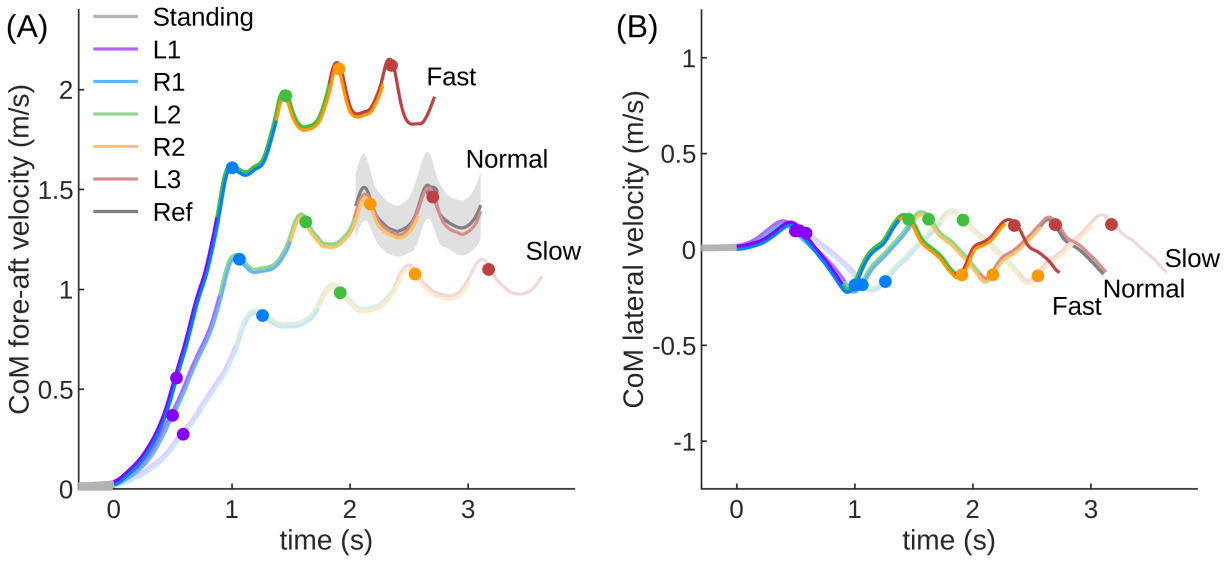

Figure 3: The mean CoM velocity over ten subjects for the slow, normal and fast target velocity gait initiation. Ref is the mean of CoM fore-aft velocity at preferred walking velocity. The light gray error band indicates the ± 1 standard deviation of Ref. Time 0 is defined as the starting of the gait initiation. Different colors denote different strides. The dots denote the take-off timing. (A) The CoM velocity in the fore-aft direction. Positive values indicate the forward direction. (B) The CoM velocity in the lateral direction. Positive values indicate the right direction.

Fig. 4). While the ankle extension torques on both limbs are decreasing (Fig. 4), a forward shifting of weight is observed.

Leading limb lifting initiation phase (P2)

The initiation of lifting the leading limb starts with the flexion of the hip and ends with the take-off of the leading limb. Simultaneously, the hip flexion torque and the hip flexion angle increase (Fig. 4). Small amounts of positive power for ankle plantarflexion and knee flexion can be observed (Fig. 4). While the hip angle is much more flexed compared to the reference walking stride, the magnitude of the flexion torque and particularly the flexion power are comparable to the reference walking stride (Fig. 4).

Trailing limb push-off phase (P3)

The trailing limb push-off phase starts after the take-off of the leading limb and ends with the take-off of the trailing limb. It is characterized by high ankle plantarflexion and knee flexion torque as well as increasing values in hip flexion torque (Fig. 4). A high burst of positive ankle plantarflexion power, positive hip flexion power and little amounts of knee positive power can be observed during this phase. At the first touch-down of the leading limb (beginning of L2), the knee and hip flexion angles are larger than the reference walking trial (Fig. 4).

Stabilizing phase (P4)

The stabilizing phase starts at the push-off of the trailing limb. It is characterized by similar joint angle, torque and power patterns compared to the reference walking stride (Fig. 4). The amplitudes of the reference walking stride are reached with increasing walking velocity. Most of the target velocity is

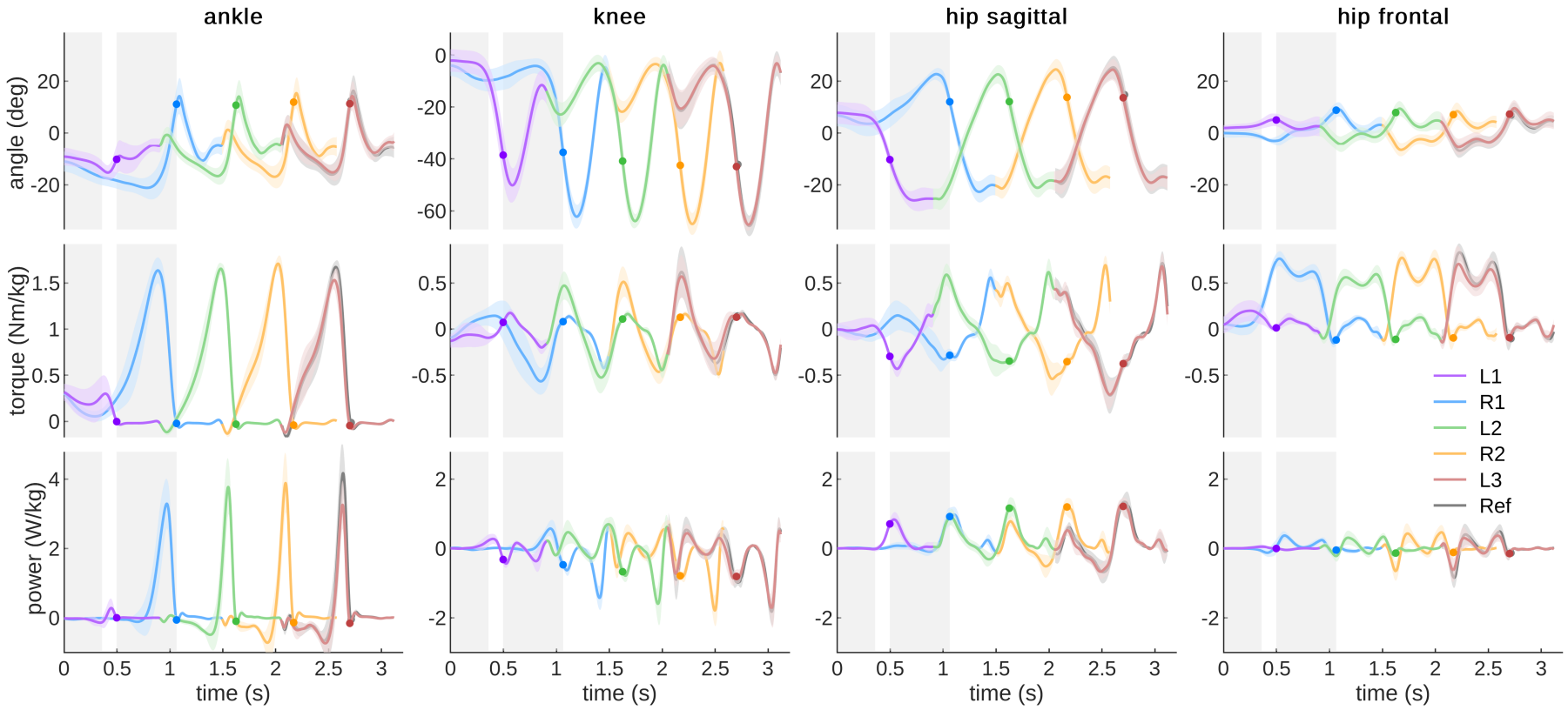

Figure 4: Ankle extension/flexion, knee extension/flexion, hip extension/flexion and hip abduction/adduction angle, torque and power during the normal velocity gait initiation. Hip and knee extension, ankle plantarflexion, hip abduction, and extension torque are defined as positive. Solid lines denote the mean value over nine subjects. The error bands denote ± 1 standard deviation. Time 0 is defined as the beginning of the gait initiation. Different colors denote different strides. L1, L2, L3 denote the first, second, and third stride on the left side, respectively. R1 and R2 denote the first and second stride on the right side. Ref denotes the regular overground walking at self-selected preferred velocity. The dots denote the take-off timing.

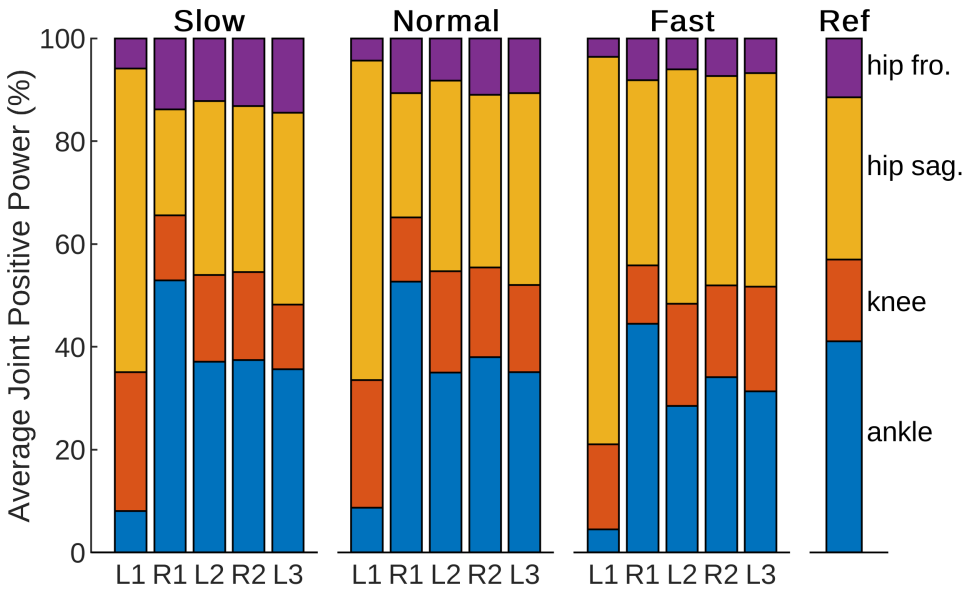

Figure 5: Relative contribution of the average positive joint power for the first five strides of slow, normal and fast gait initiation and the reference trial. Purple indicates the frontal plane hip joint (abduction/adduction). Yellow indicates the sagittal plane hip joint (flexion/extension). Orange indicates the knee flexion/extension. Blue indicates the ankle plantarflexion and dorsiflexion.

already achieved at the take-off of the trailing limb (R1) and only small increases are found for L2, R2 and L3 at all tested target velocities (Tab. 1).

4.4.2 Energy injection during the gait initiation

a) Joint energy input

For the first stride of the leading limb (L1), more than half of the average positive joint power is provided by the hip joint in the sagittal plane (slow $58.2\% \pm 13.6\%$, normal $60.6\% \pm 18.5\%$, fast $74.1\% \pm 14.6\%$, Fig. 5), which is about twice compared to the reference stride (steady walking at preferred velocity, $32.1\% \pm 4.0\%$). During L1, the ankle joint has almost no contribution (slow $8.4\% \pm 8.3\%$, normal $9.0\% \pm 8.0\%$, fast $5.0\% \pm 5.6\%$), which is much lower than the reference stride ($40.9\% \pm 4.7\%$). In contrast, for the first stride of the trailing limb (R1), the ankle joint contributes about half of the total average positive power in slow ($52.7\% \pm 6.9\%$) and normal target velocity condition ($52.2\% \pm 7.0\%$), which is higher compared to the reference stride. The distribution for providing positive joint power changes with each stride till L2 and stays almost equal in the following strides. The percentage contribution of each joint average positive power to the total average positive power is not significantly different for all the strides (i.e. L1, R1, L2, R2, and L3) between the three target velocities (Fig. 5).

The ankle average positive joint power reaches the normal walking level in R1, while the negative joint power in L1, R1 and L2 are significant smaller than the reference walking stride (Fig. 6). The knee negative joint power gradually increases from L1 to R2 and it reaches the reference walking stride level at R2. The knee average positive power in L1 and R1 are much smaller than in the reference. The sagittal hip average positive joint power in both L1 and R1 are less compared to L2, R2, and L3 (Fig. 6). The knee average net power from L1 to L3 are all negative, while all other joints average net power are positive.

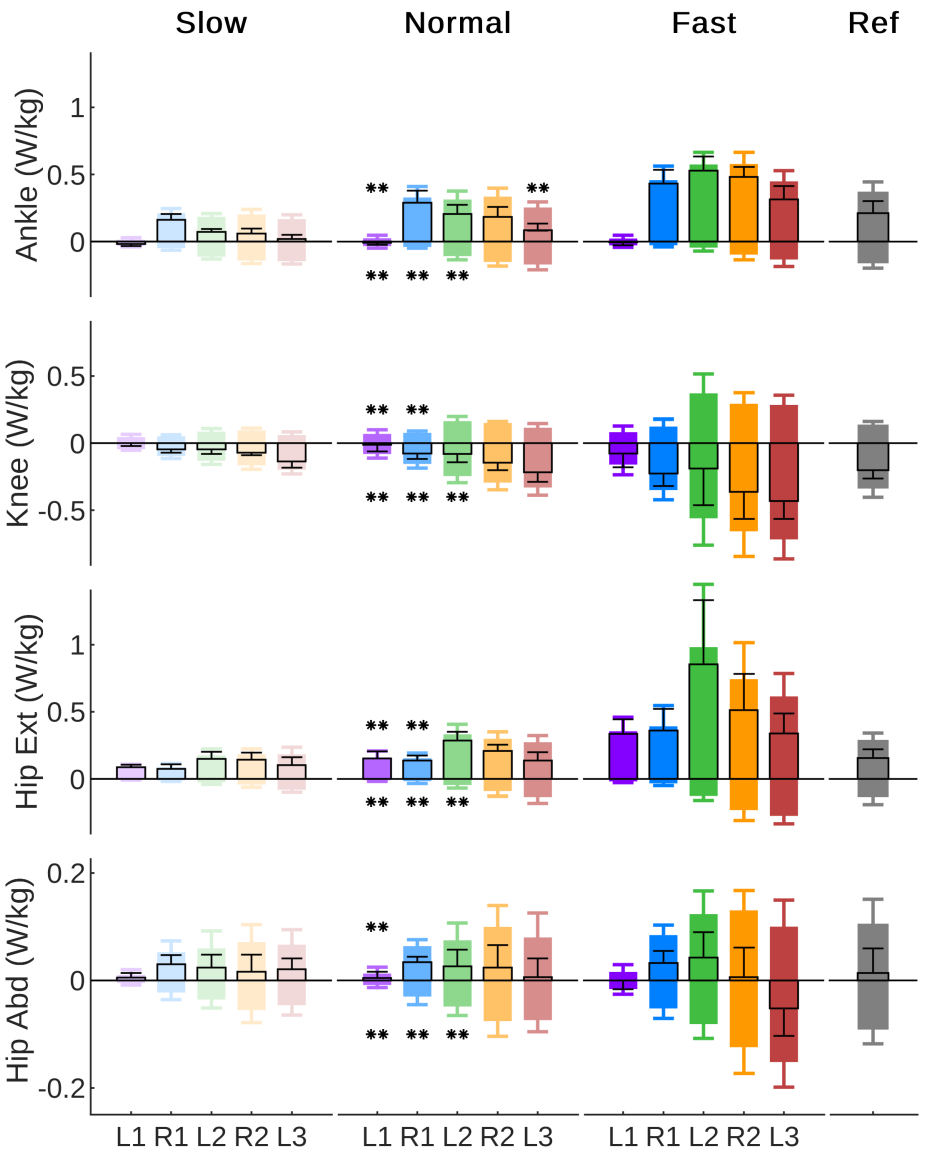

Figure 6: Average positive, negative and net joint power for the first five strides (L1, R1, L2, R2, L3) of slow, normal and fast target velocity gait initiation and the reference walking. Error bars indicate ± 1 standard deviation. Positive bars indicate positive power. Negative bars indicate negative power. Black frames indicate average net joint power. The double asterisks (**) indicates the significant difference $p < 0.01$ with respect to Ref.

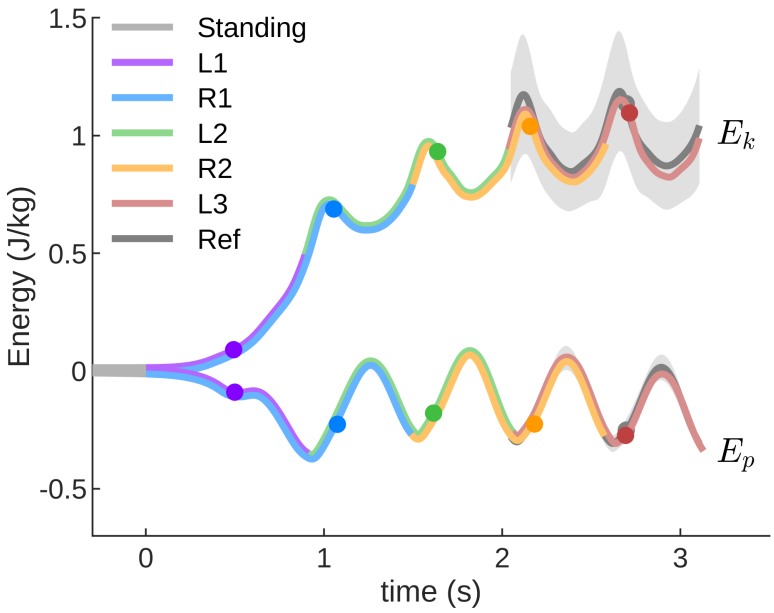

Figure 7: The CoM kinetic (E_k) and potential (E_p) energy during normal velocity gait initiation. Solid lines denote the mean value over nine subjects. Time 0 is defined as the starting of the gait initiation. E_p during standing is defined as zero. Ref denotes overground walking at self-selected preferred velocity. The error bands denote ± 1 standard deviation. Different colors denote different strides. L1, L2, L3 denote the first, second, and third stride on the left side, respectively. R1 and R2 denote the first and second stride on the right side. The dots denote the take-off timing.

Comparing the different target velocity conditions, the relative contributions of the joint average positive power are similar between the slow and the normal condition for all five strides (Fig. 5). The sagittal hip joint has higher contribution in the fast condition compared to the normal condition in L1 and R1. The total average positive joint power increases with higher target velocity.

b) CoM potential and kinetic energy

A comparison of the CoM potential and the CoM kinetic energy of gait initiation (normal target velocity) is shown in Fig. 7. For standing, the CoM potential energy was defined as zero. At the instance of the L1 TO, the increase in the CoM kinetic energy ($0.077 \pm 0.034\,\mathrm{J/kg}$) is similar ($p = 0.334$) to the decrease in CoM potential energy ($0.096 \pm 0.047\,\mathrm{J/kg}$). At the beginning of L2, the CoM potential energy reaches the minimum ($0.370 \pm 0.075\,\mathrm{J/kg}$).

c) CoM Mechanical Power

The CoM mechanical power stays almost zero over the first stride (L1) for all three target velocity conditions (Fig. 8). For the following strides, the CoM mechanical power shows similar pattern as in the regular walking. For the normal condition, the peak CoM mechanical power in the second stride (R1) reaches similar magnitude as the reference stride. The CoM collision power is minimal for R1 and L2 (Fig. 8 and 9). It increases to values comparable to the reference stride within R2 and L3. The CoM rebound power in L2 is higher than all other strides for both normal and fast conditions. For the normal condition, the CoM preload power is increasing with the increasing number of strides, whereas the CoM

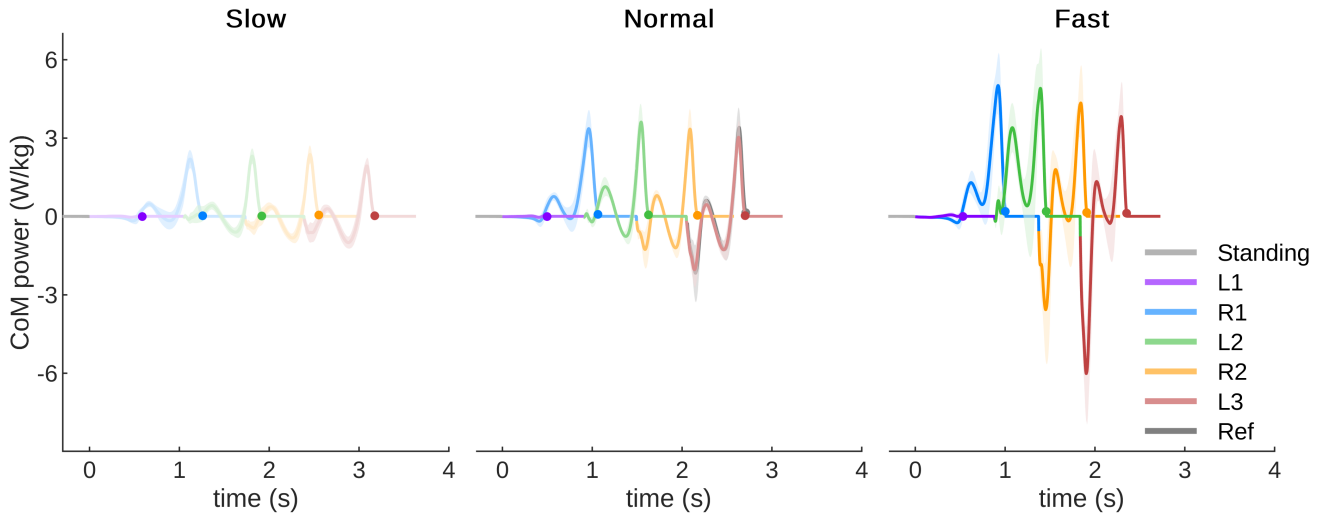

Figure 8: The CoM mechanical power of slow, normal and fast gait initiation. Solid lines denote the mean value over nine subjects. Time 0 is defined as the beginning of the gait initiation. Ref denotes the regular overground walking at self-selected velocity. The error bands denote ± 1 standard deviation. Different colors denote different strides. L1, L2, L3 denote the first, second, and third stride on the left side, respectively. R1 and R2 denote the first and second stride on the right side. The dots denote the take-off timing.

push-off power stays at an equal level compared to the reference. Due to the low magnitude, the phase specific CoM mechanical power during L1 was not analyzed.

4.5 Discussion

The goal of this paper is to further understand the gait initiation mechanism and the energy sources for increasing the CoM forward velocity from the lower-limb joint-level perspective. The first five strides of the gait initiation for three target velocities were analyzed in this study. Inverse kinematics and inverse dynamics analysis were performed to investigate the contribution of individual joint to the gait initiation. The CoM mechanical power, kinetic and potential energy analysis were used to explain joint behaviors. The results reveal the lower-limb joint functions in the frontal and sagittal plane, and provide unique insights on both balancing and energy injection mechanism during human gait initiation.

4.5.1 Joint positive power distributions

In order to investigate if there are specific joints which are primarily drive the leading and Comparing the last stride (L3) during the gait initiation data in slow, normal, and fast target velocity condition, the average positive power at all lower-limb joints increases with walking velocity (Fig. 6). In contrast, the relative contributions of each joint to total positive power are similar with different velocities in L3 (Fig. 5). These findings are in line with previous studies (Cavagna and Kaneko, 1977; Farris and Sawicki, 2011).

However, the contributions of the sagittal hip and ankle joint are different in the first two strides (L1 and R1) of the gait initiation, compared to the steady state walking (Fig. 5). In L1, the sagittal hip joint exhibits the highest average positive power contribution compared to all the other three joints (Fig. 5). A

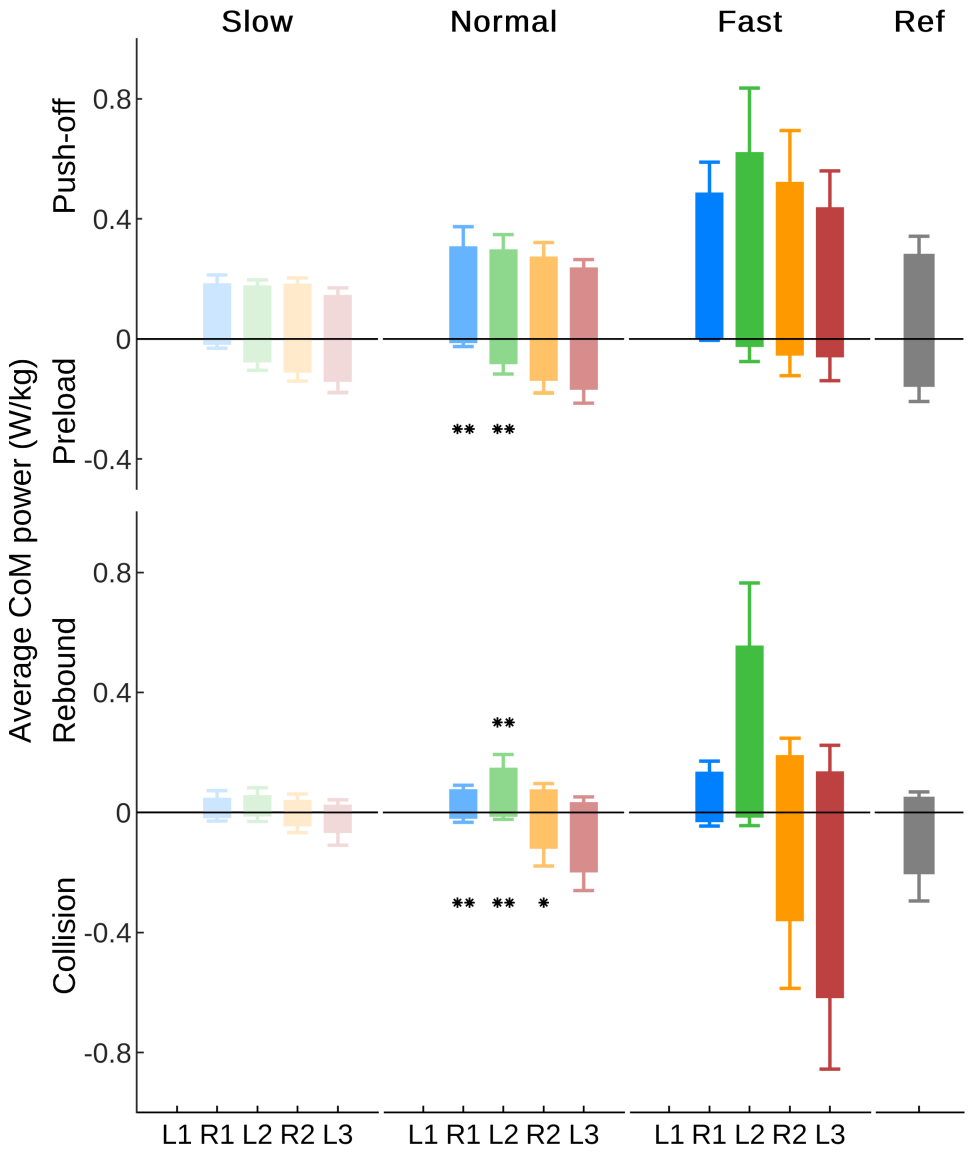

Figure 9: The average CoM power for slow, normal and fast gait initiation in collision, rebound, preload and push-off phase. Ref denotes the regular overground walking at self-selected velocity. Error bars indicate standard deviation. L1, L2, L3 denote the first, second, and third stride on the left side, respectively. R1 and R2 denote the first and second stride on the right side. The single asterisk (*) and double asterisks (**) indicate that the significant difference $p < 0.05$ and $p < 0.01$ with respect to Ref, respectively.

large hip flexion peak torque can be observed after the TO of the leading limb in L1 (Fig. 4). This supports our hypothesis that, in order to swing the leg forward, the hip in the leading limb contributes more during the first stride compared to the steady state (Fig. 5). In addition, the hip flexion torque can also lift the leg upwards and ensure foot ground clearance during the swing phase. Such increases in proximal muscle power output can also be observed during other dynamic movements such as human walking acceleration (Qiao and Jindrich, 2016), human sprinting (Novacheck, 1998) or in running acceleration of turkeys (Roberts and Scales, 2002). The ankle joint torque and power in L1 do not have the push-off pattern, which is typically observed in the steady state walking (Zelik and Adamczyk, 2016) (Fig. 4). This is because the ankle Achilles tendon and muscles (e.g. soleus and gastrocnemius muslce) are not loaded and preactivated as in the steady state walking stride (Ishikawa et al., 2005; Lichtwark and Wilson, 2007, 2008). Therefore the ankle joint shows lower contribution in L1 compared to the steady state (Fig. 5).

Although the CoM is accelerating in both the first (L1) and the second (R1) stride (Fig. 3), the joint positive power contributions are different. In R1, the average positive power contribution of the ankle joint is higher than in the sagittal hip joint for slow and normal gait initiation (Fig. 5). Such an increase in the relative ankle contribution can not be found during acceleration in human walking, in human sprinting or acceleration of running turkeys (Novacheck, 1998; Qiao and Jindrich, 2016; Roberts and Scales, 2002). Such a behavior can only occur for gait initiation as R1 is missing the positive hip extension power, which is typically used in continuous locomotion to accelerate the body forward.

4.5.2 Strategies for accelerating the CoM forward

Four mechanisms that contribute to the CoM forward acceleration during the gait initiation can be observed based on the results. These are a) the transfer of potential energy to kinetic energy, b) an excessive hip flexion of the leading limb, c) a strong ankle push-off by the trailing limb, and d) a minimization of collision power.

Increased lower-limb joint peak torque and power can be observed during accelerated walking (Farris and Raiteri, 2017; Qiao and Jindrich, 2016). On the contrary, our results show that the joint peak torque and power during gait initiation are not more than the steady state walking. This is because, in order to minimize the metabolic cost, humans utilize the potential energy during standing to accelerate the CoM during gait initiation (Fig. 7). Our analyses on the ankle joint torque show that the CoM fore-aft velocity is created by decreasing ankle extension (plantarflexion) torque, which makes the body to fall forward like an inverted pendulum (Fig. 4). This is in line with the findings of decreased soleus muscle activity and increased tibialis muscle activity at the beginning of gait initiation (Crenna and Frigo, 1991). It also supports the prior work using an inverted pendulum model to interpret the gait initiation (Breniere and Do, 1986, 1991; Breniere et al., 1987; Brunt et al., 1991). After the TO of the leading limb (L1), lower-limb joints start to inject energy to the body and accelerate the CoM forward. For instance, the leading limb hip exerts an excessive flexion torque to accelerate the leg forward. The trailing limb ankle joint shows a push-off pattern, which is similar to the steady state walking in both shape and magnitude, to redirect the CoM velocity direction and further accelerate the CoM forward (Fig. 4, 3 and 7). These findings confirm our hypothesis that the potential energy contributes the most to the CoM kinetic energy for the first stride, whereas for the following strides the positive joint work dominates the energy contribution. Besides exerting positive joint power, minimizing negative joint power can also

help to accelerate the CoM velocity and lower the metabolic cost. Our results indicate that this strategy is utilized by humans. For instance, all joint average negative powers in the first three strides are smaller than the steady state condition (Fig. 6). In addition, the CoM collision powers in the second and third strides are almost zero (Fig. 9).

4.5.3 Balancing at the beginning of gait initiation

In order to keep balance, the CoM has to be shifted towards the trailing limb (stance leg) before the lifting of the leading limb (swing leg) (Fig. 2). This requires higher leg force in the leading limb than the trailing limb (Fig. 3). Such a behavior was shown in prior work, which also demonstrated the lateral shift movement of the CoP at the beginning of gait initiation (Caderby et al., 2014; Halliday et al., 1998; Jian et al., 1993). Jian et al. (1993) speculated that the CoP movement is due to a momentary loading of the swing limb and an unloading of the stance limb. It remained unclear how the weight shift is achieved on the joint level.

Our results demonstrate that the trailing limb leg force decreases and the leading limb leg force increases (weight shifting initiation phase, P1, Fig. 2), while both patterns are similar (inverted). This indicates that humans prefer to keep the CoM vertical acceleration zero while shifting the CoM laterally. This could be done by extending the leading limb (e.g. ankle plantarflexion) and shortening the trailing limb (e.g. hip and knee flexion), which potentially requires complex control for the coordination of the muscles of both legs. Another way to achieve this is to exert abduction torque or adduction torque on the leading limb or the trailing limb hip joint, respectively. This is a simpler approach since it only needs to control one joint. The increase in hip abduction torque (Fig. 4) supports our hypothesis that humans use the leading limb hip abduction torque to realize the initial lateral weight shift.

4.5.4 The emergence of the walking pattern

The vertical GRF during the stance phase of walking is characteristically M-shaped (Keller et al., 1996; Nilsson and Thorstensson, 1989), which is attributed to the leg compliance (Geyer et al., 2006). Surprisingly, the trailing limb already exhibits the M-shape pattern after the weight shifting initiation phase (P1, Fig. 2). Further, the CoM mechanical power pattern in R1 also shows similar rebound and push-off behavior as in the normal walking (Fig. 8, Fig. 9). These findings indicate that the compliant leg behavior for walking has already emerged after the TO of the leading limb.

Our results indicate there could be an order of switching the control of lower-limb joints from standing to walking. The leading limb hip flexion/extension joint first shows similar torque at the TO of L1 both in shape and magnitude as the steady state walking stride (Fig. 4). Following, the steady-state-like torque pattern in the trailing limb ankle, knee and hip abduction/adduction joint can be observed. After the TD of L1, all joints show similar patterns (angle, torque, power) as in steady state walking. The similar behaviors can also be found in the slow and the fast gait initiation condition (Fig. 10 and 11).

4.5.5 Future work

This work focused on the biomechanical analysis of human gait initiation from the lower-limb joint perspective. In future studies, we plan to develop walking models, which are capable of reproducing the gait initiation features observed in this paper. For instance, we can potentially extend the current simplified

models (e.g. the conceptual models from Anand et al. (2017); Maus et al. (2010)) to 3D and reproduce the hip joint function for gait initiation. The human gait initiation data can also be used to optimize the control parameters of multi-segment musculoskeletal walking models (e.g. Geyer and Herr (2010); Song and Geyer (2015)). Such a model could provide further insights on how human generate different gaits at the neuromuscular level. Further, it could also be used as part of a controller for prostheses and exoskeletons to support human walking (e.g. Eilenberg et al. (2010); Wu et al. (2017); Zhao et al. (2017)).

4.6 Conclusion

This paper aims at further understanding of the gait initiation mechanism focusing on the energy injection from the lower-limb joint perspective. This study provides unique insights on the coupling between the frontal and sagittal plane joints during the gait initiation. We found that the hip abduction torque on the leading limb (lifting leg) is the key to initiate the lateral weight shift at the beginning of gait initiation. The walking gait pattern in both overall leg behavior and individual lower-limb joint emerges after the TO of the leading limb. The hip flexion/extension joint has the highest contribution to the joint positive power in the first stride while the ankle joint contributes the most in the second stride. The peak torque and power of all joints during gait initiation are not more than the steady state walking condition.

The results of this study provide a gait initiation dataset of young and healthy humans, which could be used a reference for the diagnosis of gait impairments and related rehabilitation or medical care. Further, joint kinematics and kinetics can be used to develop concepts for human intention recognition regarding gait initiation. The data and our outcomes can potentially help to develop control principles and assistance techniques to improve the assistance of wearable assistive devices such as exoskeletons and prostheses. In addition, a novel bipedal robot design and control could also be inspired by the presented human gait initiation strategies.

Acknowledgments

Guoping Zhao was supported by the EU project BALANCE under the grant agreement number 601003. Martin Grimmer was funded by the German Science Foundation (DFG) under the grant number GR 4689/3-1.

4.7 Appendix

4.7.1 Mean CoM velocity

The mean CoM velocity for five consecutive strides (i.e. L1, R1, L2, R2, and L3) during gait initiation with three different target velocities are shown in Table 1.

4.7.2 Joint kinematics and kinetics during slow and fast GI

The lower-limb joint kinematics and kinetics during slow and fast target velocity are shown in Fig. 10 and Fig. 11, respectively.

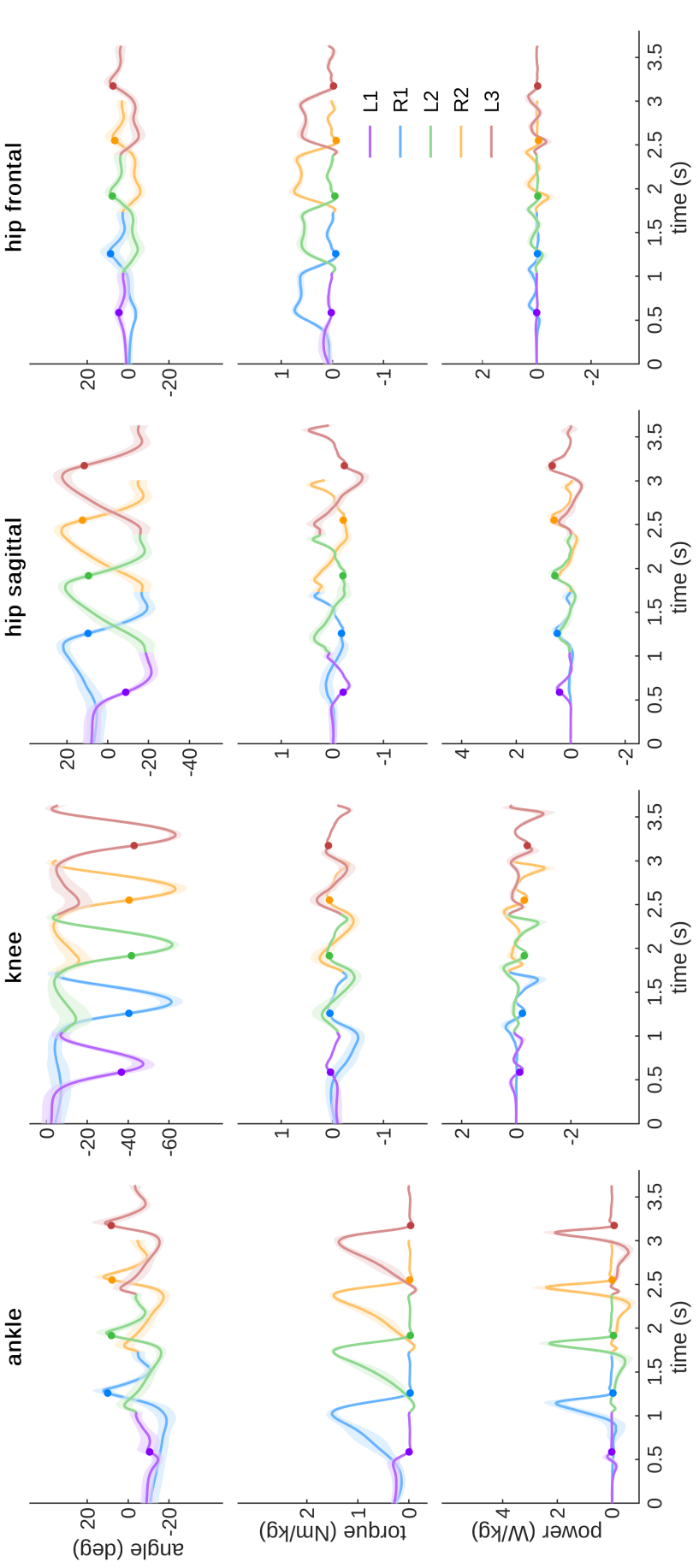

Figure 10: Ankle extension/flexion, knee extension/flexion, hip extension/flexion and hip abduction/adduction joint angle, torque and power during the slow target velocity gait initiation. Extension and abduction angle, torque and power are defined as positive. Solid lines denote the mean value over nine subjects. The error bands denote ± 1 standard deviation. Time 0 is defined as the starting of the gait initiation. Different colors denote different strides. L1, L2, L3 denote the first, second, and third stride on the left side, respectively. R1 and R2 denote the first and second stride on the right side. Ref denotes the regular overground walking at self-selected preferred velocity. The dots denote the take-off moment.

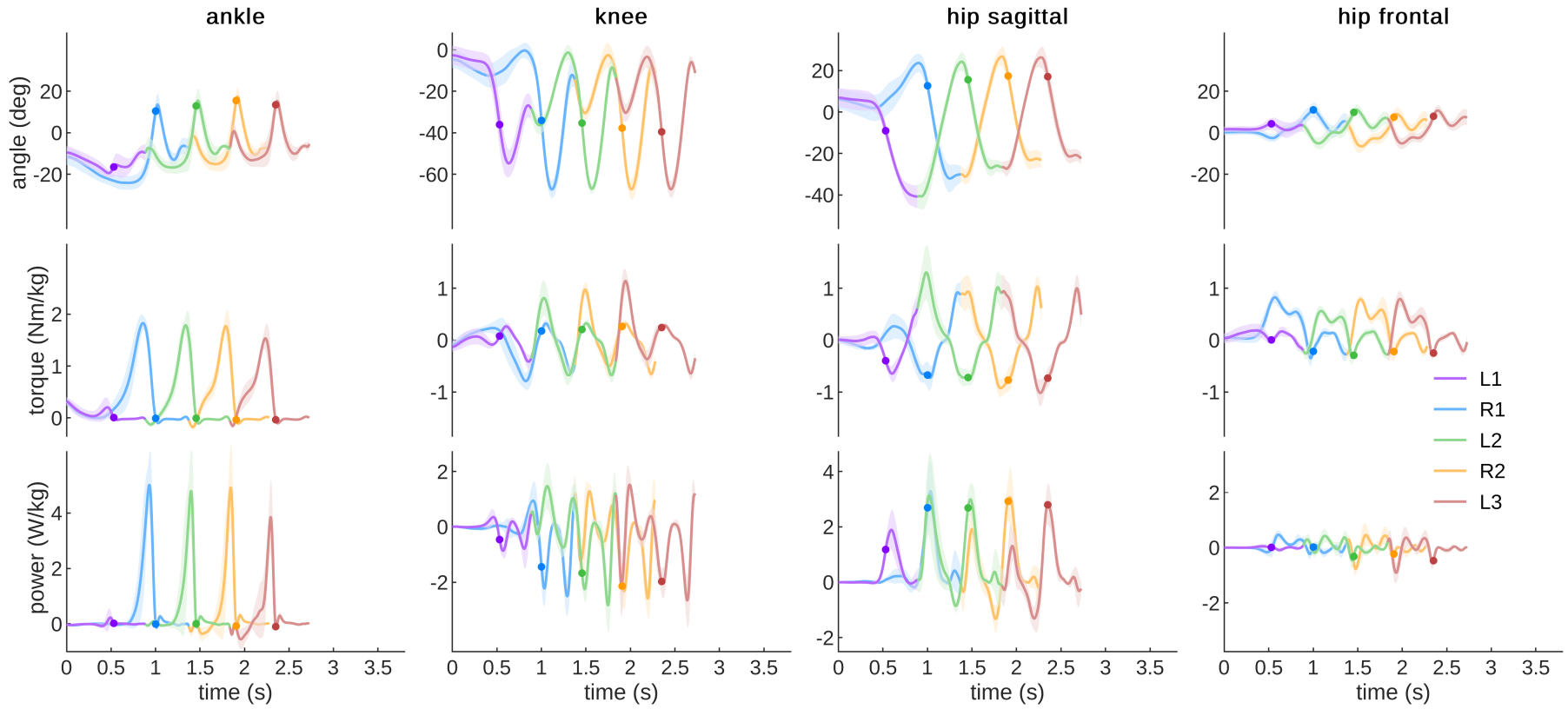

Figure 11: Ankle extension/flexion, knee extension/flexion, hip extension/flexion and hip abduction/adduction joint angle, torque and power during the fast target velocity gait initiation. Extension and abduction angle, torque and power are defined as positive. Solid lines denote the mean value over nine subjects. The error bands denote ± 1 standard deviation. Time 0 is defined as the starting of the gait initiation. Different colors denote different strides. L1, L2, L3 denote the first, second, and third stride on the left side, respectively. R1 and R2 denote the first and second stride on the right side. Ref denotes the regular overground walking at self-selected preferred velocity. The dots denote the take-off moment.

Table 1: Mean center of mass (CoM) velocity for five consecutive strides during gait initiation with three different target velocities. Mean±1standard deviation. The unit is m/s.

Stride	L1	R1	L2	R2	L3
slow	0.27 ± 0.03	0.49 ± 0.04	0.87 ± 0.06	0.96 ± 0.06	1.00 ± 0.07
normal	0.37 ± 0.04	0.67 ± 0.06	1.22 ± 0.13	1.33 ± 0.14	1.37 ± 0.14
fast	0.51 ± 0.06	0.90 ± 0.09	1.77 ± 0.22	1.94 ± 0.20	1.96 ± 0.17

Author contributions

Guoping Zhao is the main and corresponding author of this paper. Guoping Zhao was responsible for the conceptualization and methodology of this work. Guoping Zhao and Martin Grimmer designed the experiment. Guoping Zhao conducted the experiment, processed and analyzed the data. Guoping Zhao and Martin Grimmer drafted the manuscript. All authors interpreted the data and revised the manuscript.

References

Anand, M., Seipel, J., and Rietdyk, S. (2017). A modelling approach to the dynamics of gait initiation. *Journal of The Royal Society Interface*, 14(128):20170043.

Bloem, B. R., Hausdorff, J. M., Visser, J. E., and Giladi, N. (2004). Falls and freezing of gait in parkinson's disease: A review of two interconnected, episodic phenomena. *Movement Disorders*, 19(8):871–884.

Breniere, Y. and Do, M. (1986). When and how does steady state gait movement induced from upright posture begin? *Journal of Biomechanics*, 19(12):1035 – 1040.

Breniere, Y. and Do, M. C. (1991). Control of gait initiation. *Journal of motor behavior*, 23(4):235–240.

Breniere, Y., Do, M. C., and Bouisset, S. (1987). Are dynamic phenomena prior to stepping essential to walking? *Journal of Motor Behavior*, 19(1):62–76. PMID: 23944913.

Brunt, D., Lafferty, M. J., Mckeon, A., Goode, B., Mulhausen, C., and Polk, P. (1991). Invariant characteristics of gait initiation. *American journal of physical medicine & rehabilitation*, 70(4):206–212.

Brunt, D., Liu, S.-M., Trimble, M., Bauer, J., and Short, M. (1999). Principles underlying the organization of movement initiation from quiet stance. *Gait & Posture*, 10(2):121 – 128.

Caderby, T., Yiou, E., Peyrot, N., Begon, M., and Dalleau, G. (2014). Influence of gait speed on the control of mediolateral dynamic stability during gait initiation. *Journal of Biomechanics*, 47(2):417 – 423.

Cavagna, G. A. and Kaneko, M. (1977). Mechanical work and efficiency in level walking and running. *The Journal of physiology*, 268(2):467–481. 874922[pmid].

Crenna, P. and Frigo, C. (1991). A motor programme for the initiation of forward-oriented movements in humans. *The Journal of Physiology*, 437(1):635–653.

Delp, S. L., Anderson, F. C., Arnold, A. S., Loan, P., Habib, A., John, C. T., Guendelman, E., and Thelen, D. G. (2007). Opensim: Open-source software to create and analyze dynamic simulations of movement. *IEEE Transactions on Biomedical Engineering*, 54(11):1940–1950.

Donelan, J., Kram, R., and Kuo, A. D. (2002). Simultaneous positive and negative external mechanical work in human walking. *Journal of Biomechanics*, 35(1):117 – 124.

Eilenberg, M. F., Geyer, H., and Herr, H. (2010). Control of a powered ankle–foot prosthesis based on a neuromuscular model. *IEEE Transactions on Neural Systems and Rehabilitation Engineering*, 18(2):164–173.

Elble, R. J., Moody, C., Leffler, K., and Sinha, R. (1994). The initiation of normal walking. *Movement Disorders*, 9(2):139–146.

Farris, D. J. and Raiteri, B. J. (2017). Modulation of leg joint function to produce emulated acceleration during walking and running in humans. *Royal Society Open Science*, 4(3):160901.

Farris, D. J. and Sawicki, G. S. (2011). The mechanics and energetics of human walking and running: a joint level perspective. *Journal of The Royal Society Interface*, page rsif20110182.

Geyer, H. and Herr, H. (2010). A muscle-reflex model that encodes principles of legged mechanics produces human walking dynamics and muscle activities. *IEEE Transactions on Neural Systems and Rehabilitation Engineering*, 18(3):263–273.

Geyer, H., Seyfarth, A., and Blickhan, R. (2006). Compliant leg behaviour explains basic dynamics of walking and running. *Proceedings of the Royal Society of London B: Biological Sciences*, 273(1603):2861–2867.

Grimmer, M., Eslamy, M., and Seyfarth, A. (2014). Energetic and peak power advantages of series elastic actuators in an actuated prosthetic leg for walking and running. *Actuators*, 3(1):1–19.

Halliday, S. E., Winter, D. A., Frank, J. S., Patla, A. E., and Prince, F. (1998). The initiation of gait in young, elderly, and parkinson's disease subjects. *Gait & Posture*, 8(1):8 – 14.

Hamner, S. R., Seth, A., and Delp, S. L. (2010). Muscle contributions to propulsion and support during running. *Journal of Biomechanics*, 43(14):2709 – 2716.

Hansen, A. H., Miff, S. C., Childress, D. S., Gard, S. A., and Meier, M. R. (2010). Net external energy of the biologic and prosthetic ankle during gait initiation. *Gait & posture*, 31(1):13–17.

Houck, J. R., Duncan, A., and Kenneth, E. (2006). Comparison of frontal plane trunk kinematics and hip and knee moments during anticipated and unanticipated walking and side step cutting tasks. *Gait & posture*, 24(3):314–322.

Ishikawa, M., Komi, P. V., Grey, M. J., Lepola, V., and Bruggemann, G.-P. (2005). Muscle-tendon interaction and elastic energy usage in human walking. *Journal of Applied Physiology*, 99(2):603–608. PMID: 15845776.

Jian, Y., Winter, D. A., Ishac, M. G., and Gilchrist, L. (1993). Trajectory of the body cog and cop during initiation and termination of gait. *Gait & Posture*, 1(1):9–22.

Keller, T., Weisberger, A., Ray, J., Hasan, S., Shiavi, R., and Spengler, D. (1996). Relationship between vertical ground reaction force and speed during walking, slow jogging, and running. *Clinical Biomechanics*, 11(5):253 – 259.

Lichtwark, G. and Wilson, A. (2007). Is achilles tendon compliance optimised for maximum muscle efficiency during locomotion? *Journal of Biomechanics*, 40(8):1768 – 1775.

Lichtwark, G. and Wilson, A. (2008). Optimal muscle fascicle length and tendon stiffness for maximising gastrocnemius efficiency during human walking and running. *Journal of Theoretical Biology*, 252(4):662 – 673.

Maus, H.-M., Lipfert, S., Gross, M., Rummel, J., and Seyfarth, A. (2010). Upright human gait did not provide a major mechanical challenge for our ancestors. *Nature communications*, 1:70.

Maus, H.-M., Seyfarth, A., and Grimmer, S. (2011). Combining forces and kinematics for calculating consistent centre of mass trajectories. *Journal of Experimental Biology*, 214(21):3511–3517.

Nilsson, J. and Thorstensson, A. (1989). Ground reaction forces at different speeds of human walking and running. *Acta Physiologica Scandinavica*, 136(2):217–227.

Novacheck, T. F. (1998). The biomechanics of running. *Gait & Posture*, 7(1):77 – 95.

Nutt, J. G., Bloem, B. R., Giladi, N., Hallett, M., Horak, F. B., and Nieuwboer, A. (2011). Freezing of gait: moving forward on a mysterious clinical phenomenon. *The Lancet Neurology*, 10(8):734 – 744.

Qiao, M. and Jindrich, D. L. (2016). Leg joint function during walking acceleration and deceleration. *Journal of Biomechanics*, 49(1):66 – 72.

Roberts, T. J. and Scales, J. A. (2002). Mechanical power output during running accelerations in wild turkeys. *Journal of Experimental Biology*, 205(10):1485–1494.

Song, S. and Geyer, H. (2015). A neural circuitry that emphasizes spinal feedback generates diverse behaviours of human locomotion. *The Journal of Physiology*, 593(16):3493–3511.

Tudor-Locke, C. and Bassett Jr, D. R. (2004). How many steps/day are enough? *Sports Med*, 34(1):1–8.

Umberger, B. R. and Martin, P. E. (2007). Mechanical power and efficiency of level walking with different stride rates. *Journal of Experimental Biology*, 210(18):3255–3265.

Winter, D. A. (2009). *Biomechanics and Motor Control of Human Movement*. John Wiley & Sons, Hoboken, NewJersey USA, fourth edition.

Wu, A. R., Dzeladini, F., Brug, T. J. H., Tamburella, F., Tagliamonte, N. L., van Asseldonk, E. H. F., van der Kooij, H., and Ijspeert, A. J. (2017). An adaptive neuromuscular controller for assistive lower-limb exoskeletons: A preliminary study on subjects with spinal cord injury. *Frontiers in Neurorobotics*, 11:30.

Yiou, E., Caderby, T., Delafontaine, A., Fourcade, P., and Honeine, J.-L. (2017). Balance control during gait initiation: State-of-the-art and research perspectives. *World journal of orthopedics*, 8(11):815.

Zelik, K. E. and Adamczyk, P. G. (2016). A unified perspective on ankle push-off in human walking. *Journal of Experimental Biology*, 219(23):3676–3683.

Zhao, G., Sharbafi, M., Vlutters, M., Van Asseldonk, E., and Seyfarth, A. (2017). Template model inspired leg force feedback based control can assist human walking. In *Rehabilitation Robotics (ICORR), 2017 International Conference on*, pages 473–478. IEEE.

5 Article III: Template Model Inspired Leg Force Feedback Based Control Can Assist Human Walking

Authors:

Guoping Zhao, Maziar Ahmad Sharbafi, Mark Vlutters,
Edwin van Asseldonk, Andre Seyfarth

Lauflabor Locomotion Laboratory, TU Darmstadt, Darmstadt, Germany
School of Electrical and Computer Engineering, College of Engineering, University of Tehran, Iran
Department of Biomechanical Engineering, University of Twente, Enschede, Netherlands

Published as a paper in

2017 International Conference on Rehabilitation Robotics (ICORR), pages 473–478.

5.1 Abstract

We present a novel control approach for assistive lower-extremity exoskeletons. In particular, we implement a virtual pivot point (VPP) template model inspired leg force feedback based controller on a lower-extremity powered exoskeleton (LOPES II) and demonstrate that it can effectively assist humans during walking. It has been shown that the VPP template model is capable of stabilizing the trunk and reproduce a human-like hip torque during the stance phase of walking. With leg force and joint angle feedback inspired by the VPP template model, our controller provides hip and knee torque assistance during the stance phase. A pilot experiment was conducted with four healthy subjects. Joint kinematics, leg muscle electromyography (EMG), and metabolic cost were measured during walking with and without assistance. Results show that, for 0.6 m/s walking, our controller can reduce leg muscle activations, especially for the medial gastrocnemius (about 16.0%), while hip and knee joint kinematics remain similar to the condition without the controller. Besides, the controller also reduces 10% of the net metabolic cost during walking. This paper demonstrates walking assistance benefits of the VPP template model for the first time. The support of human walking is achieved by a force feedback of leg force applied to the control of hip and knee joints. It can help us to provide a framework for investigating walking assistance control in the future.

5.2 Introduction

A lower-extremity exoskeleton is a wearable robotic device acting in parallel with human lower extremities for assisting human locomotion. It has been widely developed in the last two decades for both impaired (Esquenazi et al., 2012; Jezernik et al., 2003; Kawamoto and Sankai, 2005; Veneman et al., 2007) and able-bodied people (Asbeck et al., 2013; Collins et al., 2015; Malcolm et al., 2013; Zoss et al., 2006). Human walking gait is controlled by a sophisticated network of neurons resulting in coordinated muscle forces and joint movements (Capaday, 2002; Geyer and Herr, 2010), which makes it challenging to assist walking with a lower-extremity exoskeleton.

However, despite the complex human leg function, the principle characteristics of basic human gaits (i.e. hopping, running, and walking) can be captured by a simple spring loaded inverted pendulum (SLIP) model (Blickhan, 1989; Geyer et al., 2006). The SLIP model consists a point mass, representing the human body center of mass (CoM), and one or two massless springs, representing the leg functions. By replacing the point mass with a rigid trunk, the SLIP model can be extended to a TSLIP model (Sharbafi et al., 2013) such that posture/hip control strategies can be investigated. Maus et al. (Maus et al., 2010) proposed a posture controller based on the virtual pivot point (VPP) concept. The VPP can be regarded as a point above the CoM, through which the ground reaction force (GRF) passes during stable walking. By controlling hip torques to redirect the GRF through the VPP, stable walking with an upright trunk could be realized in a TSLIP model. This controller can be approximated by a force modulated compliant hip (FMCH) approach inspired by the muscle properties and reflex systems (Sharbafi and Seyfarth, 2015).

Template models, like SLIP and VPP model, have potentials in bipedal robots and exoskeletons. It has been shown that the SLIP model can be used as a principle guideline for designing and controlling bipedal robots (Garofalo et al., 2012; Hubicki et al., 2016). Grabowski and Herr (Grabowski and Herr, 2009) also showed that a spring-like leg exoskeleton can reduce the metabolic cost of human hopping.

The goal of this study is to prove the feasibility of the implementation of the controller in an exoskeleton with actuated hip and knee joint. We expect that a simple leg force feedback controller, which is inspired by the VPP template model and the FMCH approach, can reduce human lower limb internal work (Willems et al., 1995) during locomotion. By outsourcing this muscular work to exoskeleton, a lower leg muscles activation during walking is expected.

The controller was implemented in the lower-extremity exoskeleton LOPES II (section II). LOPES II is a lower extremity powered exoskeleton developed at University of Twente (Vallery et al., 2009, 2008; Veneman et al., 2007; Meuleman et al., 2016). Joint kinematics, leg muscles activation, and metabolic cost were analyzed during walking with and without the assistance controller (section III).

5.3 Methods

5.3.1 VPP concept based hip control

The VPP walking model includes a rigid trunk and two massless prismatic legs (Fig. 1(a)) (Maus et al., 2010). A hip torque is required to direct the GRF through the VPP. According to this concept, the individual leg hip torque is as (Maufroy et al., 2011):

$$\tau_h = F l \frac{r_h \sin\varphi + r_p \sin(\varphi+\gamma)}{l - r_h \cos\varphi - r_p \cos(\varphi+\gamma)} \tag{1}$$

where τ_h, F, l, φ, r_p and r_h denote individual leg hip torque, leg force, leg length, hip angle, and the distance from CoM to VPP and hip joint respectively. γ denotes the angle between trunk axis and the vector from CoM to VPP. Replacing (F,l,φ) in (1) with $\left(F^L,l^L,\varphi^L\right)$ or $\left(F^R,l^R,\varphi^R\right)$ will get τ_h^L or τ_h^R, where the superscript L and R denote the left and right leg, respectively.

The VPP model can be approximated by the FMCH model (Fig. 1(b)) if $\gamma < 20^\circ$ and $150^\circ < \varphi^{L,R} < 210^\circ$ (Sharbafi and Seyfarth, 2015). The FMCH model uses a variable stiffness rotational spring to generate a similar hip torque and a similar VPP position above the CoM. Leg force is used as a feedback for adjusting hip stiffness. The hip torque τ_h computation is simplified as (Sharbafi and Seyfarth, 2015):

$$\tau_h = cF(\varphi_0 - \varphi) \tag{2}$$

where c and φ_0 denote hip spring stiffness (constant, normalized to body weight) and rest angle, respectively. c can be computed as:

$$c = \frac{\bar{l} r}{\bar{l} + r} \tag{3}$$

where r and $\bar{l}$ denote the distance from the VPP to the hip joint and the average leg length during the stance phase, respectively.

Equation (2) was implemented as the hip torque controller because it is simpler while it has similar performance compared to (1) (Sharbafi and Seyfarth, 2015).

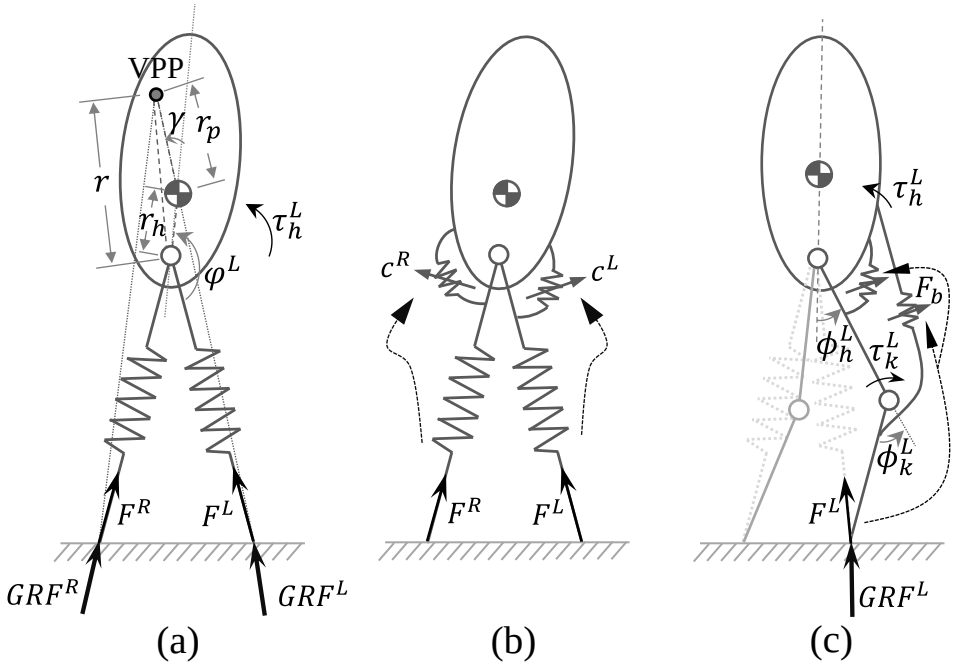

Figure 1: Conceptual models. (a) Virtual pivot point (VPP) model (Maufroy et al., 2011; Maus et al., 2010). (b) Force modulated compliant hip (FMCH) model (Sharbafi and Seyfarth, 2015). (c) Human walking model for knee control. Only left leg springs and parameters are shown.

5.3.2 Knee control

Inspired by the human leg muscle morphology and muscle local reflexes(Geyer and Herr, 2010), two variable stiffness springs (one monoarticular spring and one biarticular spring) are considered for each leg (Fig. 1(c)). The hip torque τ_h is produced by both springs. We assume 1) the torque produced by the biarticular spring force F_b on the hip is proportional to τ_h; 2) the biarticular spring lever arm ratio between the knee and hip ε is variable and follows the equation

$$\varepsilon = \kappa + \cos(\phi_k + \phi_{k0}) \tag{4}$$

where ϕ_k is the knee joint angle. ϕ_{k0} and κ are constant values. Based on these two assumptions, the knee torque τ_k is computed as:

$$\tau_k = b\varepsilon\tau_h \tag{5}$$

where b is a constant value which represents how much the biarticular spring contributes to the hip torque.

5.3.3 Control implementation

The VPP concept based control was implemented on the exoskeleton LOPES II. The VPP concept requires joint torque control. LOPES II is admittance controlled (Meuleman et al., 2016) in the low level which enables torque control for each actuated joint.

The VPP based controller requires the leg force and CoP position as feedback, individually. In the current control setup, an instrumented treadmill is integrated which measures total CoP position $\left(x_{cop}^T, y_{cop}^T\right)^T$ and total vertical GRF GRF_z^T. The x-axis, y-axis and z-axis denote the left-right, fore-aft and vertical direction, respectively. Thus, the individual leg force F has to be estimated.

During the double stance phase, the projection of each ankle joint on the ground is assumed as the CoP for each leg. Therefore, the individual leg GRF_z can be estimated as:

$$\begin{bmatrix} GRF_z^L \\ GRF_z^R \end{bmatrix} = \begin{bmatrix} |y_{cop}^T - y_a^R| \\ |y_{cop}^T - y_a^L| \end{bmatrix} \frac{GRF_z^T}{|y_a^L - y_a^R|} \tag{6}$$

where the superscript L and R denote the left and right leg. The subscript a denotes ankle joint. Individual leg GRF_z equals to GRF_z^T during the single stance phase.

Individual leg force magnitude is estimated as:

$$F = GRF_z \sin\theta \tag{7}$$

where θ is the leg angle with respect to the vertical direction. θ is estimated as:

$$\theta = \arccos \frac{y_h - y_a}{|\mathbf{p}_h - \mathbf{p}_a|} \tag{8}$$

where $\mathbf{p}_h$ and $\mathbf{p}_a$, which can be directly measured by LOPES II, denote the position of hip $(x_h, y_h, z_h)^T$ and ankle $(x_a, y_a, z_a)^T$ joint in the global Cartesian space.

Combining with (2), desired hip flexion/extension torque applied by the exoskeleton to the human τ_{hExo} is computed as:

$$\tau_{hExo} = \eta_h \tau_h = \eta_h cF\left(\varphi_0 - \varphi\right) \tag{9}$$

where η_h is the gain for adjusting hip assisting level. Note φ is the virtual hip angle. It is the angle between trunk axis and the vector from ankle to hip joint.

Desired knee flexion/extension torque applied by the exoskeleton to the human τ_{kExo} is computed as:

$$\tau_{kExo} = \eta_k \tau_k = \eta_k b\left(\kappa + \cos(\phi_k + \phi_{k0})\right) cF\left(\varphi_0 - \varphi\right) \tag{10}$$

Although the parameters (η_h, c, η_k, b) may look like redundant, it is important to take them as independent parameters because η_h and η_k define the assistance level in hip and knee joint, while c and b are the parameters related to the gait. For instance, η_h and η_k should remain constant but c and b should be increased if we want to keep the same assistance level while increase the walking speed.

The controller has seven parameters for each leg $(\eta_h, c, \varphi_0, \eta_k, b, \phi_{k0}, \kappa)$. Left and right leg parameters should be the same if the subject is able-bodied and walks symmetrically. The initial value of each parameter can be estimated from human walking data and simulation results. Then the parameters are tuned

Table 1: Parameter values used in the experiment

Parameter	Value [unit]
η_h	0.25 ± 0.04
c	$0.166\,\mathrm{m/rad}$
φ_0	$186.5^\circ \pm 1.29^\circ$
η_k	0.25 ± 0.04
b	0.5
ϕ_{k0}	20°
κ	0.1

manually for each subject before the experimental trial. The parameter values used in the experiment are shown in Table 1.

Note that our control is only active during the stance phase. The assisting torque from exoskeleton to human during swing phase is set as zero (transparent mode).

The controller was implemented in Matlab 2015b with Simulink Real-time toolbox. LOPES II was controlled by a Matlab xPC target machine with a sampling time of 0.001 s.

5.3.4 Experimental setup

In order to check the muscle response, four leg muscles (rectus femoris (REF), hamstring (HAM), medial gastrocnemius (GAS), and gluteus maximus (GLM)) electromyography (EMG) signals were recorded (Delsys Inc., Natick, USA) with a frequency of 1000 Hz. In addition, for the last two subjects, metabolic cost was measured (Oxycon Pro, Jaeger GmbH, Hoechberg, Germany) to assess how much energy expenditure can be reduced by the assistive controller. Oxygen consumption rate ($\dot{V}_{O_2}$) and carbon dioxide output rate ($\dot{V}_{CO_2}$) were measured every five seconds. Joint kinematics were measured by LOPES II sensors with a sampling rate of 1000 Hz.

5.3.5 Experimental protocol

A preliminary experiment was conducted for testing the controller. Four young and healthy subjects (3 males, 1 female, age 30±5.7 yrs, height 1.78±0.13 m, weight 73.8±3.9 kg) participated in the experiment. Subjects were instructed to wear LOPES II and walk on the treadmill with a constant speed (Fig. 2). The second version LOPES II has eight powered degrees of freedom. It includes hip flexion/extension, knee flexion/extension, hip abduction/adduction, pelvis forward/backward and mediolateral (Meuleman et al., 2016). Each subject's pelvis, shanks, and feet were firmly attached to the braces of LOPES II and were instructed to swing their arms freely (without any arm support from the handrail) and walk normally during the experiment. Due to the speed limitation of LOPES II, the treadmill speed was set as 0.6 m/s.

First of all, to familiarize with the exoskeleton, each subject had a test walking trial (about 3∼5 min) wearing LOPES II in the transparent mode. Then the exoskeleton control was switched to assisted mode with very low gains (<0.01). The control parameters were adapted for each subject by gradually in-

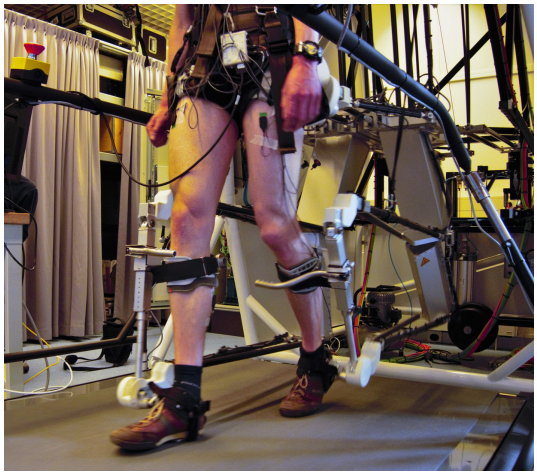

Figure 2: Photo of a healthy subject walking with LOPES II.

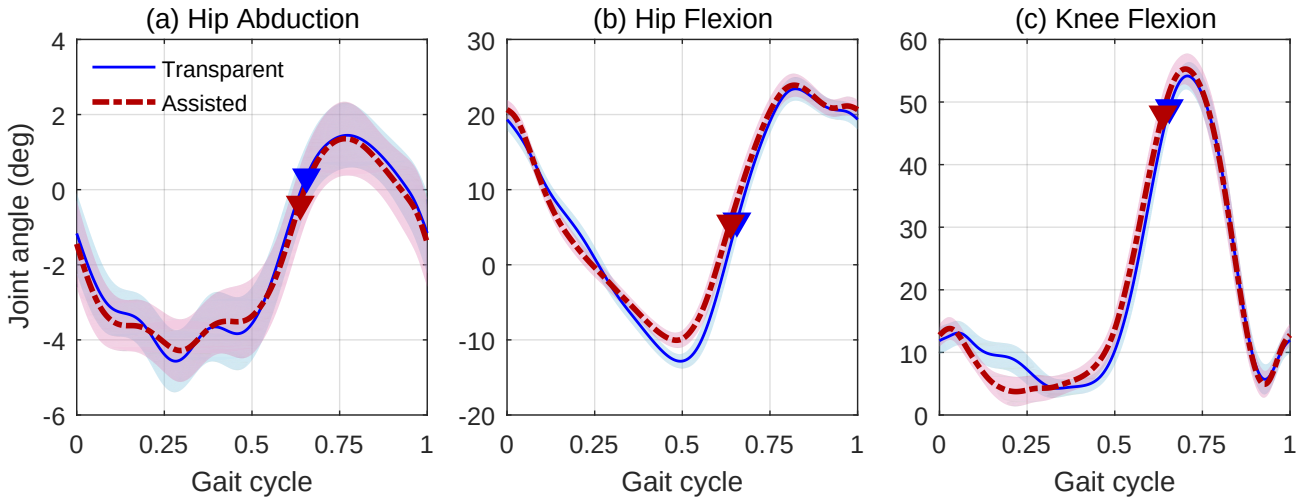

Figure 3: Joint kinematics in one gait cycle. Abduction angle is shown as positive in the subfigure (a). Flexion angle is shown as positive in the subfigure (b) and (c). Solid and dashed lines denote the mean results of all four subjects. Error bands denote ± 1 standard deviation. Transparent and assisted mode walking are shown in blue and red color, respectively. Triangle markers denote the take-off (TO).

creasing the gains and adjusting other parameters until the subject felt most comfortable (about 10 min). Afterwards the experimental trials were conducted.

In the experimental trials, subjects were instructed to walk on the treadmill wearing LOPES II with a constant speed of 0.6 m/s for about 15 min. The exoskeleton control for the first and the second half of each trial was transparent and assisted mode respectively.

Due to the hardware failure, the metabolic cost measurement was only conducted with the last two subjects. The protocol was 3 min transparent walking for warming up (data were not analyzed), 7 min assisted walking, 7 min transparent walking, and 3 min quiet standing at the end.

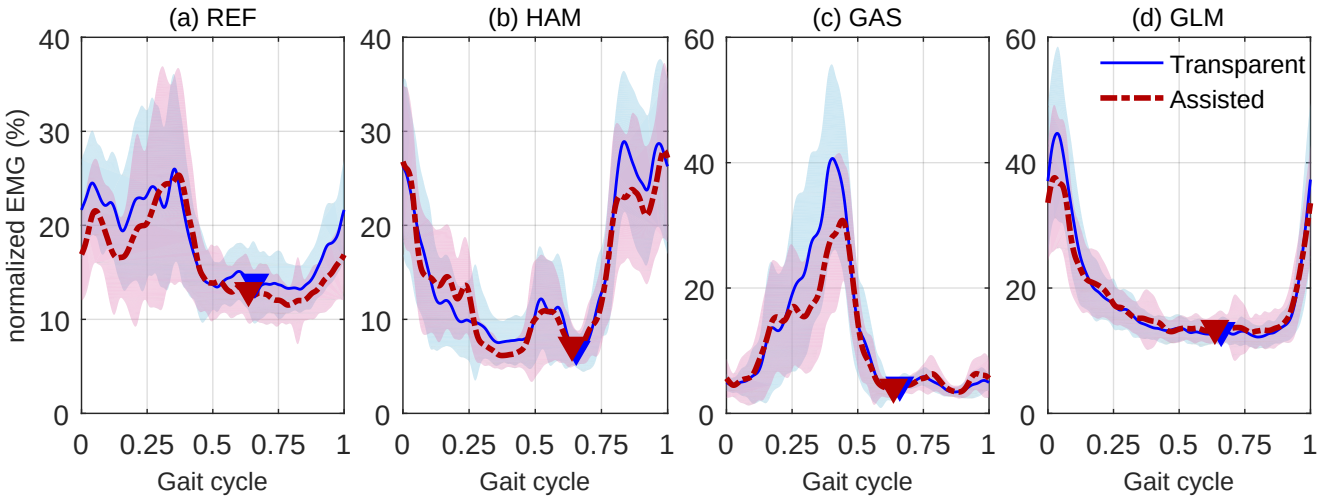

Figure 4: Normalized electromyography (EMG) of (a) rectus femoris (REF), (b) hamstring (HAM), (c) medial gastrocnemius (GAS), and (d) gluteus maximus (GLM) muscle in one walking gait cycle. Solid and dashed lines denote the mean results of all four subjects. Error bands denote ± 1 standard deviation. Transparent and assisted mode walking are shown in blue and red color, respectively. Triangle markers denote the take-off (TO).

5.3.6 Data processing

EMG raw data were filtered with a high-pass filter (cutoff frequency 20 Hz, 4th order zero-lag Butterworth), demeaned, rectified, and low-pass filtered (cutoff frequency 10 Hz, 4th order zero-lag Butterworth) (Sawicki and Ferris, 2008). Then for every trial, each muscle EMG data were normalized using the peak value during the first transparent mode walking phase. The root mean square (r.m.s.) of muscle EMG during each gait cycle was computed to quantify changes in EMG amplitude and indicate average muscle activation level.

The joint kinematics and EMG data of the last 50 gait cycles in the transparent and assisted mode were analyzed and presented in the section III. Statistical analysis (two-sample-t-test) was performed for each subject's muscle r.m.s. EMG data.

Normalized metabolic power was calculated as (Brockway, 1987):

$$P = \frac{16.58\dot{V}_{O_2} + 4.51\dot{V}_{CO_2}}{m} \tag{11}$$

where P and m denote the metabolic power (W/kg) and the subject body mass (kg) respectively. The unit of $\dot{V}_{O_2}$ and $\dot{V}_{CO_2}$ are ml/s.

The net metabolic power during walking was calculated by subtracting the metabolic power during quiet standing form the total metabolic power. The mean of the last 2 min metabolic power during standing was used as the standing metabolic power. The mean of the last 5 min metabolic power in the transparent and assisted mode walking were computed as the walking metabolic power.

5.4 Results

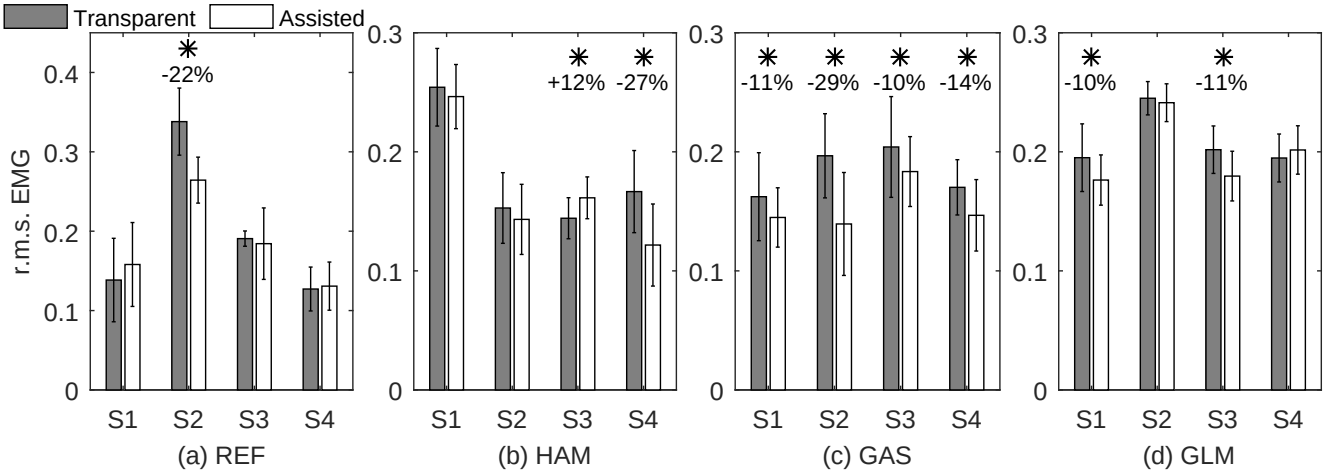

Figure 5: Root mean square electromyography (r.m.s. EMG) of rectus femoris (REF), hamstring (HAM), medial gastrocnemius (GAS), and gluteus maximus (GLM) muscle. S1, S2, S3 and S4 indicate four different subjects. Transparent and assisted mode walking are shown as gray and white bars respectively. Asterisks denote a statistically significant difference between transparent and assisted walking ($p < 0.01$). Error bars are ± 1 standard deviation. Numbers listed below asterisks indicate percentage difference in assisted compared with transparent condition.

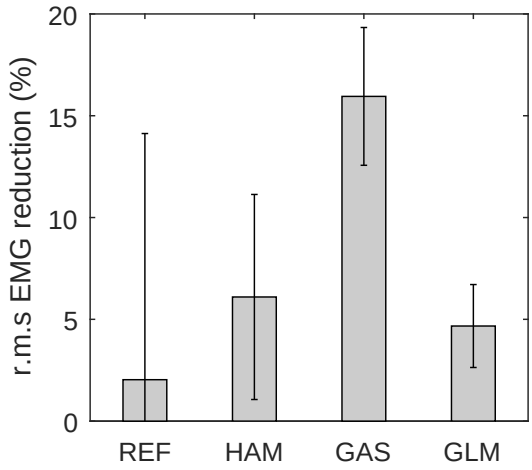

Figure 6: Average root mean square electromyography (r.m.s. EMG) reduction of all four subjects. REF, HAM, GAS, and GLM denote rectus femoris, hamstring, medial gastrocnemius, and gluteus maximus muscle, respectively. Error bars are ± 1 standard deviation.

5.4.1 Joint kinematics

The hip abduction/adduction, hip flexion/extension, and knee flexion/extension angle patterns during the gait cycle are similar when comparing the assisted to the transparent mode (Fig. 3). There is almost no difference between the two modes for these three joint angles during the swing phase (65∼100% of gait cycle). The difference in hip abduction/adduction angle is fairly small (less than 0.4°). The mean maximum hip extension angle in the assisted mode is about 2.8° smaller compared to the transparent mode. At the beginning of the stance phase ($0 \sim 30\%$ of gait cycle), the knee reaches full extension angle at 20% and 30% of gait cycle in the assisted and the transparent mode, respectively. Step frequency

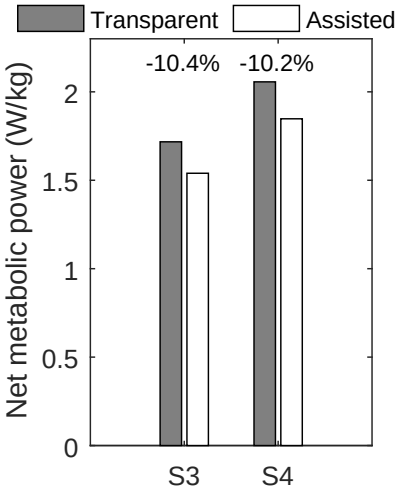

Figure 7: Net metabolic power during transparent and assisted mode walking. S3 and S4 denote two different subjects. Transparent and assisted mode walking are shown as gray and white bars respectively.

is nearly the same for the assisted (1.20±0.09 Hz) and transparent mode (1.19±0.04 Hz). As treadmill speed is constant, step length also stays the same because step frequency does not change.

5.4.2 Muscle activation

Fig. 4 shows the mean normalized EMG pattern of all four subjects. All four muscles have similar activation pattern in the assisted and the transparent mode. However, the EMG peaks clearly decrease for GAS (push-off phase), HAM (the end of swing phase), and GLM (the beginning of stance phase).

The GAS average activations of all subjects in assisted mode significantly decreased compared to the transparent mode (S1: 11% reduction, $p = 0.006$; S2: 29% reduction, $p < 0.001$; S3: 10% reduction, $p = 0.005$; S4: 14% reduction, $p < 0.001$; Fig. 5). The other three muscles do not have a consistent decreasing or increasing trend between assisted and transparent mode across four subjects. Only the REF of subject S2 has a significant difference between transparent and assisted mode (22% reduction, $p < 0.001$). The HAM activation in the assisted mode is significantly increased 12% ($p < 0.001$) in subject S3 but decreased 27% ($p < 0.001$) in subject S4 compared to the transparent mode. For GLM, the activation in assisted mode has a significant reduction for both subject S1 (10%, $p < 0.001$) and S2 (11%, $p < 0.001$).

The mean average muscle activation of four subjects are all reduced in assisted mode compared to transparent mode (Fig. 6). Mean reduction of REF, HAM, GAS, and GLM are 2.0%, 6.1%, 16.0%, and 4.7% respectively.

5.4.3 Metabolic cost

For both subjects, whose the oxygen consumption were measured, a reduction in the net metabolic power (10.4% and 10.2%) comparing assisted to transparent mode walking (Fig. 7) was identified.

5.5 Discussions and conclusions

The results show that our VPP inspired leg force feedback assistance controller can assist the subjects without affecting the gait pattern. The net metabolic power is reduced while the step length and the hip adduction/abduction angle (indicating step width) remain similar. This also indicates that the controller did not disturb the postural balance. The most significant difference between the joint angle in two conditions is detected at the early stance phase of knee flexion/extension. With the assistance controller, the knee reaches full extension much faster (Fig. 3(c)). This fully extended knee can reduce the knee extensor muscles force during stance phase which explains the REF EMG activation reduction at the early stance phase (Fig. 4(a)). But on the other hand, it can also attenuate the knee function in impact absorption (Mann and Hagy, 1980) and increase the knee joint forces. This effect has to be considered if the controller is applied to the subjects who might have difficulties in handling high landing impacts.

Similar EMG patterns in transparent and assisted mode (Fig. 4) suggest that the subjects adapted easily to the controller. Different subjects show different adaptation strategies in the muscle level (Fig. 5). For example, the HAM activation was significantly increased for the subject S3 while decreased for S4. However, the GAS activation was significantly decreased for all subjects, which was also indicated in the GAS activation as a reduced peak during the pre-swing phase (Fig. 4(c)). It is in agreement with what was observed in other studies (Lenzi et al., 2013). This suggests that, by facilitating leg flexion, the plantar flexion (push-off) can be assisted even though the exoskeleton did not produce direct torque assistance to the ankle joint. Thus, the proposed hip and knee assistance could also support people with impairments at the ankle joint (plantar flexion) or transtibial amputees. The application for neurorehabilitation of the controller needs to be explored in the future because all subjects involved in this study are young and healthy.

In conclusion, this paper presents a leg force feedback assistance controller (hip and knee), which is based on the FMCH approach inspired by the VPP template model, for lower-extremity exoskeletons during walking. The pilot experiment results show that the controller can assist human walking. This study provides a framework for using the VPP template as lower-extremity exoskeleton assistance control.

Appendix

Desired and measured hip and knee assistance torques (difference between the assisted and the transparent mode) are shown in Fig. 8.

Author contributions

Guoping Zhao is the main and corresponding author of this paper. Guoping Zhao implemented the bio-inspired controller on the LOPES II. All authors contributed to the design of the experiment. Guoping Zhao, Maziar Sharbafi, and Mark Vlutters conducted the experiment. Guoping Zhao processed and analyzed the data, and drafted the manuscript. All authors interpreted the data and revised the manuscript.

References

Asbeck, A. T., Dyer, R. J., Larusson, A. F., and Walsh, C. J. (2013). Biologically-inspired soft exosuit. In *Rehabilitation Robotics (ICORR), 2013 IEEE International Conference on*, pages 1–8.

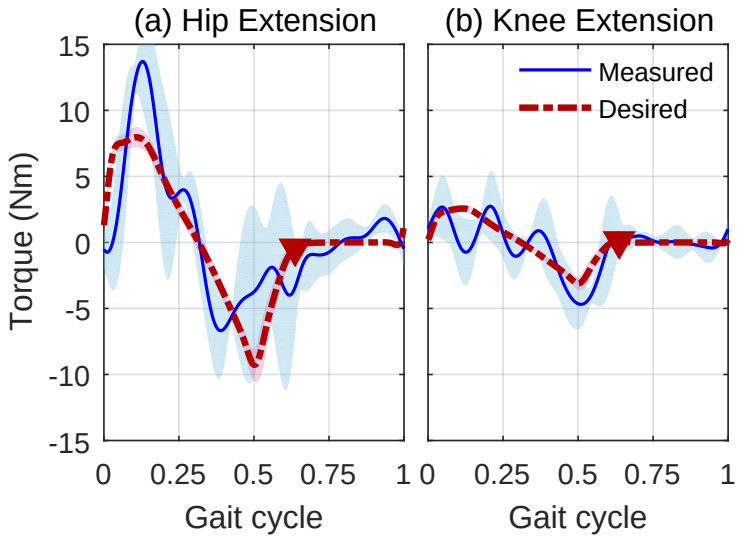

Figure 8: Torques (difference between the assisted and the transparent mode) applied to human (a) hip and (b) knee joints. Positive values denote the extension torques. Solid and dashed line denote the mean results of all four subjects. Error bands denote ± 1 standard deviation. Red and blue colors denote desired and measured torque difference, respectively. The measured torque was filtered with a low-pass filter (cutoff frequency 4Hz, 4th roder zero-lag Butterworth).

Blickhan, R. (1989). The spring-mass model for running and hopping. *Journal of Biomechanics*, 22(11–12):1217 – 1227.

Brockway, J. (1987). Derivation of formulae used to calculate energy expenditure in man. *Human nutrition. Clinical nutrition*, 41(6):463—471.

Capaday, C. (2002). The special nature of human walking and its neural control. *Trends in neurosciences*, 25(7):370–376.

Collins, S. H., Wiggin, M. B., and Sawicki, G. S. (2015). Reducing the energy cost of human walking using an unpowered exoskeleton. *Nature*, 522(7555):212–215.

Esquenazi, A., Talaty, M., Packel, A., and Saulino, M. (2012). The ReWalk Powered Exoskeleton to Restore Ambulatory Function to Individuals with Thoracic-Level Motor-Complete Spinal Cord Injury. *AMERICAN JOURNAL OF PHYSICAL MEDICINE & REHABILITATION*, 91(11):911–921.

Garofalo, G., Ott, C., and Albu-Schäffer, A. (2012). Walking control of fully actuated robots based on the bipedal slip model. In *Robotics and Automation (ICRA), 2012 IEEE International Conference on*, pages 1456–1463.

Geyer, H. and Herr, H. (2010). A muscle-reflex model that encodes principles of legged mechanics produces human walking dynamics and muscle activities. *IEEE Transactions on Neural Systems and Rehabilitation Engineering*, 18(3):263–273.

Geyer, H., Seyfarth, A., and Blickhan, R. (2006). Compliant leg behaviour explains basic dynamics of walking and running. *Proceedings of the Royal Society of London B: Biological Sciences*, 273(1603):2861–2867.

Grabowski, A. M. and Herr, H. M. (2009). Leg exoskeleton reduces the metabolic cost of human hopping. *Journal of Applied Physiology*, 107(3):670–678.

Hubicki, C., Grimes, J., Jones, M., Renjewski, D., Spröwitz, A., Abate, A., and Hurst, J. (2016). Atrias: Design and validation of a tether-free 3d-capable spring-mass bipedal robot. *The International Journal of Robotics Research*.

Jezernik, S., Colombo, G., Keller, T., Frueh, H., and Morari, M. (2003). Robotic orthosis lokomat: A rehabilitation and research tool. *Neuromodulation: Technology at the Neural Interface*, 6(2):108–115.

Kawamoto, H. and Sankai, Y. (2005). Power assist method based on phase sequence and muscle force condition for hal. *Advanced Robotics*, 19(7):717–734.

Lenzi, T., Carrozza, M. C., and Agrawal, S. K. (2013). Powered hip exoskeletons can reduce the user's hip and ankle muscle activations during walking. *IEEE Transactions on Neural Systems and Rehabilitation Engineering*, 21(6):938–948.

Malcolm, P., Derave, W., Galle, S., and De Clercq, D. (2013). A simple exoskeleton that assists plantarflexion can reduce the metabolic cost of human walking. *PLoS ONE*, 8(2):1–7.

Mann, R. A. and Hagy, J. (1980). Biomechanics of walking, running, and sprinting. *The American Journal of Sports Medicine*, 8(5):345–350. PMID: 7416353.

Maufroy, C., Maus, H. M., and Seyfarth, A. (2011). Simplified control of upright walking by exploring asymmetric gaits induced by leg damping. In *Robotics and Biomimetics (ROBIO), 2011 IEEE International Conference on*, pages 491–496.

Maus, H.-M., Lipfert, S. W., Gross, M., Rummel, J., and Seyfarth, A. (2010). Upright human gait did not provide a major mechanical challenge for our ancestors. *Nature communications*, 1(6):70.

Meuleman, J., van Asseldonk, E., van Oort, G., Rietman, H., and van der Kooij, H. (2016). Lopes ii–design and evaluation of an admittance controlled gait training robot with shadow-leg approach. *IEEE Transactions on Neural Systems and Rehabilitation Engineering*, 24(3):352–363.

Sawicki, G. S. and Ferris, D. P. (2008). Mechanics and energetics of level walking with powered ankle exoskeletons. *Journal of Experimental Biology*, 211(9):1402–1413.

Sharbafi, M. A., Maufroy, C., Ahmadabadi, M. N., Yazdanpanah, M. J., and Seyfarth, A. (2013). Robust hopping based on virtual pendulum posture control. *Bioinspiration & Biomimetics*, 8(3):036002.

Sharbafi, M. A. and Seyfarth, A. (2015). FMCH: A new model for human-like postural control in walking. In *Intelligent Robots and Systems (IROS), 2015 IEEE/RSJ International Conference on*, pages 5742–5747.

Vallery, H., van Asseldonk, E. H. F., Buss, M., and van der Kooij, H. (2009). Reference trajectory generation for rehabilitation robots: Complementary limb motion estimation. *IEEE Transactions on Neural Systems and Rehabilitation Engineering*, 17(1):23–30.

Vallery, H., Veneman, J., van Asseldonk, E., Ekkelenkamp, R., Buss, M., and van Der Kooij, H. (2008). Compliant actuation of rehabilitation robots. *IEEE Robotics Automation Magazine*, 15(3):60–69.

Veneman, J. F., Kruidhof, R., Hekman, E. E. G., Ekkelenkamp, R., Asseldonk, E. H. F. V., and van der Kooij, H. (2007). Design and evaluation of the lopes exoskeleton robot for interactive gait rehabilitation. *IEEE Transactions on Neural Systems and Rehabilitation Engineering*, 15(3):379–386.

Willems, P. A., Cavagna, G. A., and Heglund, N. C. (1995). External, internal and total work in human locomotion. *Journal of Experimental Biology*, 198(2):379–393.

Zoss, A. B., Kazerooni, H., and Chu, A. (2006). Biomechanical design of the berkeley lower extremity exoskeleton (bleex). *IEEE/ASME Transactions on Mechatronics*, 11(2):128–138.

6 Article IV: Bio-inspired Balance Control Assistance Can Reduce Metabolic Energy Consumption In Human Walking

Authors:

Guoping Zhao, Maziar Ahmad Sharbafi, Mark Vlutters,
Edwin van Asseldonk, Andre Seyfarth

Lauflabor Locomotion Laboratory, TU Darmstadt, Darmstadt, Germany
School of Electrical and Computer Engineering, College of Engineering,
University of Tehran, Iran
Department of Biomechanical Engineering, University of Twente,
Enschede, Netherlands

Accepted for publication
IEEE Transactions on Neural Systems & Rehabilitation Engineering
in 2019.

6.1 Abstract

The amount of research on developing exoskeletons for human gait assistance has been growing in the recent years. However, the control design of exoskeletons for assisting human walking remains unclear. This paper presents a novel bio-inspired reflex-based control for assisting human walking. In this approach, the leg force is used as a feedback signal to adjust hip compliance. The effects of modulating hip compliance on walking gait is investigated through joint kinematics, leg muscle activations and overall metabolic costs for eight healthy young subjects. Reduction in the average metabolic cost and muscle activation are achieved with fixed hip compliance. Compared to the fixed hip compliance, improved assistance as reflected in more consistent reduction in muscle activities and more natural kinematic behaviour are obtained using the leg force feedback. Furthermore, smoother motor torques and less peak power are two additional advantages obtained by compliance modulation. The results show that the proposed control method which is inspired by human posture control can not only facilitate the human gait, but also reduce the exoskeleton power consumption. This demonstrates that the proposed bio-inspired controller allows a synergistic interaction between human and robot.

Keywords

virtual pivot point, force modulated compliant hip, exoskeleton, bio-inspired control, human gait, assistive device

6.2 Introduction

Human locomotor systems comprise complex but intensively coupled mechanics and control to achieve gaits such as walking and running. As walking is the most common gait in daily life, assisting walking could be a way to overcome mobility related physical and functional losses (Grimmer et al., 2019). In order to assist human gait with an exoskeleton, the exoskeleton should be controlled in a way that humans can easily utilize the provided torque/force for the motion. As the exoskeleton is attached to human body, human states have to be taken into account for the control of the robot. Basic control principles of human locomotion can provide guidelines for designing assistive controllers.

Human locomotion control can be divided into reflexes (feedback, e.g. force, displacement and velocity reflexes) and central pattern generators (CPGs, i.e. feedforward) generated by the central nervous system and the preflex responses resulting from muscle dynamics (Brown and Loeb, 2000; Dietz, 2002; Ijspeert, 2008). It has been shown that the locomotion behaviors in humans and other legged animals are highly depended on the neural circuits in the spinal cord (Gerasimenko et al., 2008; Harkema et al., 2011). The CPGs can be considered as the neural circuits in the spinal cord which can generate rhythmic muscle activation patterns without any feedback inputs (Bizzi et al., 2008; Ijspeert, 2008). However, it is not required to have CPGs to produce a sequence of muscle activation patterns for locomotion. With neuromuscular simulation models, Geyer et al. showed that a pure reflex-based control (sensory feedback integration) can produce stable and diverse behaviors of human locomotion including walking and running gait (Geyer and Herr, 2010; Song and Geyer, 2015). The balance control of the model was realized by manually defined complex muscle reflex pathways. In contrast, a simplified conceptual model with spring-like prismatic legs and compliant hips can also generate human-like walking gait and balance the trunk by a simple leg force based reflex control of the hip compliance (Sharbafi and Seyfarth, 2015).

Here we focus on human-inspired posture control approaches for exoskeletons and their benefits for walking. Posture control is one of the human locomtor sub-functions (Sharbafi et al., 2017b). We believe that with posture control assistance not only stability but also energetics can be improved as locomotor sub-functions are internally connected with each other. As falling injuries are more critical than energetic drawbacks for elderly, targeting improving posture is the more important functionality compared to targeting the walking energetics.

Several control approaches that have been implemented on exoskeletons to assist human walking (Yan et al., 2015): 1) Predefined trajectory tracking based approaches. For instance, ATLAS orthoses (Sanz-Merodio et al., 2012), HAL (Sankai, 2010), Mina (Neuhaus et al., 2011), Mindwalker (Wang et al., 2015), ReWalk (Esquenazi et al., 2012), and eLEGS (Strausser and Kazerooni, 2011) for assisting pathological gaits. 2) Predefined gait pattern based control. As in the soft exosuit control in (Asbeck et al., 2013; Walsh et al., 2006), the desired assistance depends not only on the timing of the control command but also on the characteristics of the elastic elements (stiffness, inertia, damping). 3) Model based approaches in which the desired robotic action is computed on the basis of a human-exoskeleton model. These approaches usually consider gravity compensation, zero moment point (ZMP) balance criterion, and provide extra commanded assistance which requires highly precise models and multiple sensors to recognize human body kinematics and dynamics variables (Yan et al., 2015), e.g. in (Chen et al., 2009; Hyon et al., 2011; Kawamoto et al., 2010; Mori et al., 2006). 4) Adaptive oscillators-based control (basic concept used in CPG) (Ronsse et al., 2011a), which is limited to subjects who can deliver periodic and stable locomotion-related signals, and mostly validated on the hip joint actuation (Giovacchini et al., 2015; Matsubara et al., 2012; Ronsse et al., 2011b; Tagliamonte et al., 2013; Zhang and Hashimoto, 2011). 5) Proportional myoelectrical control for single joint exoskeletons, e.g. Kao et al. (Fleischer and Hommel, 2008; Kao et al., 2010; Norris et al., 2007). 6) Hybrid strategies, including aforementioned methods. E.g. BLEEX adopts a force controller in swing phase and a position controller in stance phase (Kazerooni et al., 2006); or combination of fuzzy control with other methods (He and Kiguchi, 2007; Kong and Jeon, 2006; Lenzi et al., 2013; Wu et al., 2015; Yeh et al., 2010). None of these methods take the basic control principles of human locomotion as the basis for the control of exoskeletons. Recent studies have shown that exoskeletons with neuromuscular controller which use lower limb dynamic model (Dzeladini et al., 2016; Ruiz Garate et al., 2016; Wu et al., 2017) can assist human walking. But this method requires complex neuromuscular modelling of major leg muscle groups.

In this paper, we introduce a simple bio-inspired reflex based control design in gait assistance which is developed based on a human balance control. One phenomenon observed in biological gaits that can be considered as a basis for our bio-inspired balance control is the virtual pendulum (VP) concept (Maus et al., 2010). Maus et al. showed that during human walking the ground reaction force vectors are pointing to a virtual pivot point (VPP) which is placed above the center of mas (CoM). With that the upper body oscillates stably and mimics the periodic motion of a regular pendulum. The VPP control concept can be approximated by the force modulated compliant hip (FMCH) control (Sharbafi and Seyfarth, 2014, 2015) during walking and running. The FMCH controller uses the leg force to adjust the hip stiffness which mimics force reflexes in human body. This simple reflex-based controller can generate human-like hip flexion/extension torque patterns for walking.

In the previous pilot study we have tested the FMCH based controller with both hip and knee assistance for walking (Zhao et al., 2017). We also implemented this concept using a biarticular thigh actuator with a neuromuscular model (Sharbafi et al., 2018). Both results showed that this approach is feasible to implement and can reduce both human metabolic costs and leg muscle activation. However, the individual contributions of hip and knee joint to the reductions are unclear. It also remains open whether a single joint (i.e. hip or knee joints) FMCH based assistance controller can reduce metabolic costs. It has been shown that human hip joint contributes more than 40% of positive work during walking (from 0.75 m/s to 2.00 m/s) (Farris and Sawicki, 2012). Therefore, in this paper, we focus on assisting only the hip joint.

The aim of this paper is to investigate the implementation and the resulting benefits of a human bio-inspired posture control scheme for assisting human walking. In this study, we are focusing on assisting only the hip joints to investigate the benefits of FMCH based controller for walking energetics. In addition, we also investigate the importance of leg force feedback for the assistive controller. This is achieved by comparing the results of the FMCH and the constant compliant hip (CCH) control (without force feedback).

More specifically, we employ the FMCH concept to control the hip actuator of the exoskeleton LOPES II. This method is compared with CCH. The results demonstrate the effects of these two control methods on metabolic costs, muscle activation and kinematic behavior. Finally, the effects of the leg force feedback (used as a reflex pathway) on the aforementioned human locomotion metrics, together with the impacts on efficiency of the methods, will be assessed by the consumed power and produced torques of the exoskeleton and discussed.

6.3 Methods

6.3.1 Control concepts

The VPP walking model consists of a rigid trunk and two massless spring-like prismatic legs (Fig. 1A). Each hip joint torque can be computed as (Maus et al., 2010):

$$\tau_h = Fl\frac{r_h \sin\varphi + r_p \sin(\varphi+\gamma)}{l - r_h\cos\varphi - r_p\cos(\varphi+\gamma)} \tag{1}$$

where τ_h is hip torque, F is leg force, l is leg length, φ is hip angle, r_p is the distance from CoM to VPP, and r_h is the distance from CoM to hip joint. γ denotes the angle between trunk axis and the vector from CoM to VPP. Left or right hip torque (τ_h^L or τ_h^R) can be computed by substituting (F,l,φ) in (1) with $\left(F^L,l^L,\varphi^L\right)$ or $\left(F^R,l^R,\varphi^R\right)$, where the superscript L and R denote the left and right leg, respectively.

The VPP model can be approximated by the FMCH model (Fig. 1B) if $\gamma < 20^\circ$ and $150^\circ < \varphi^{L,R} < 210^\circ$ (Sharbafi and Seyfarth, 2015). This approximation can be made during regular walking (Sharbafi and Seyfarth, 2015). A variable stiffness rotational spring was used in the FMCH model to produce a similar hip torque pattern which results in a similar VPP position above the CoM. The hip torque can be computed with the following equation by assuming the hip spring stiffness is multiplied by the leg force F (Sharbafi and Seyfarth, 2015):

$$\tau_h = cF(\varphi_0 - \varphi) \tag{2}$$

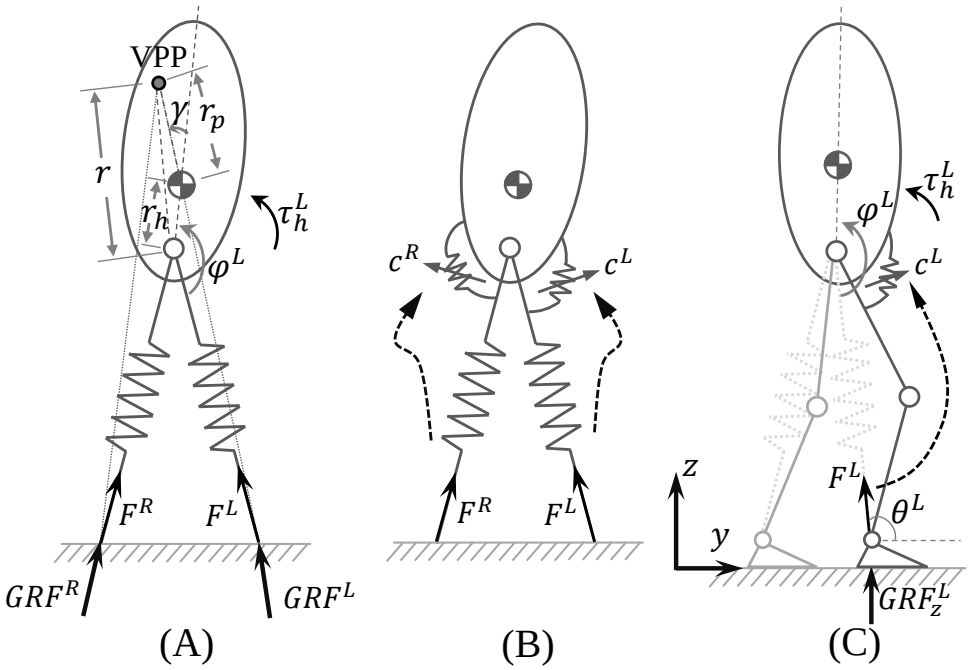

Figure 1: Bio-inspired walking models. (A) Virtual pivot point (VPP) model (Maus et al., 2010). (B) Force modulated compliant hip (FMCH) model (Sharbafi and Seyfarth, 2015). (C) The FMCH based hip torque control implemented in this study.

where c and φ_0 denote nominal hip spring stiffness (constant, normalized to body weight) and rest angle, respectively.

6.3.2 Implementation

The FMCH based hip torque control (2) was implemented on the exoskeleton LOPES II. This control is simpler while it has similar performance compared to (1) (Sharbafi and Seyfarth, 2015). LOPES II consists of a pair of shadow legs which can apply active hip flexion/extension torques on the human body with the low-level admittance controller (Fig. 2, see (Meuleman et al., 2016) for details). The instrumented treadmill provides the net vertical ground reaction force GRF_z^T and the net center of pressure position $\left(x_{cop}^T, y_{cop}^T\right)$ feedback to the control system (see Fig. 3). The left-right, fore-aft and vertical direction are denoted as x-axis, y-axis and z-axis (Fig. 1C), respectively.

Each leg force magnitude F is estimated as:

$$F = GRF_z / \sin\theta \tag{3}$$

where GRF_z and θ denote the individual leg vertical GRF and the leg angle with respect to the horizontal direction, respectively. θ is estimated as:

$$\theta = \arccos \frac{y_h - y_a}{|\mathbf{p}_h - \mathbf{p}_a|} \tag{4}$$

Figure 2: A subject walking with LOPES II exoskeleton.

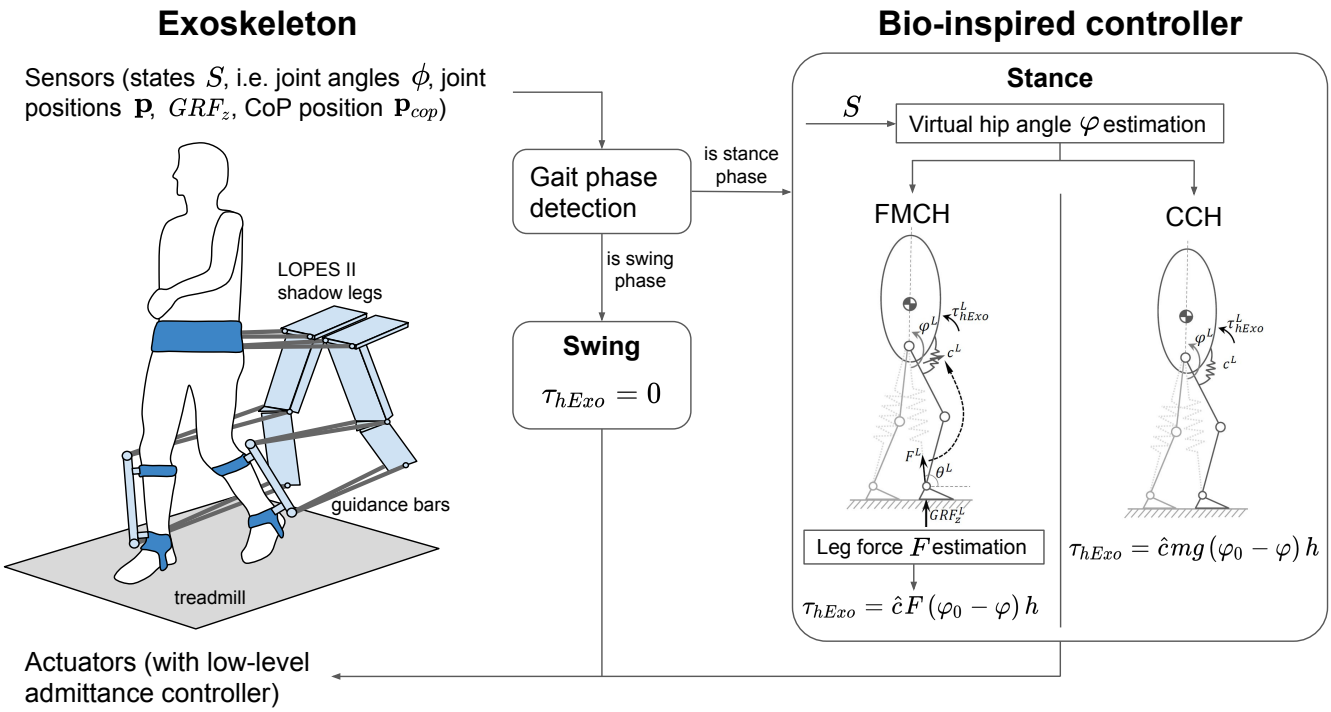

Figure 3: Schematic overview of FMCH and CCH controller. Sensors on the exoskeleton are used to detect if the leg is in stance or swing phase. The exoskeleton is set to transparent mode (hip joint torque is set to zero) if the leg is in swing phase. FMCH or CCH controller is activated if the leg is in stance phase.

Table 1: Parameter values used in the experiment

Parameter	Value [unit]
$\hat{c}$	$0.035\,\mathrm{rad}^{-1}$
φ_0	$3.264\,\mathrm{rad}$

where $\mathbf{p}_h$ and $\mathbf{p}_a$ denote the position of hip (x_h, y_h, z_h) and ankle (x_a, y_a, z_a) joint in the global Cartesian space. They can be measured by LOPES II.

Individual leg GRF_z equals to GRF_z^T during the single stance phase. In the double stance phase, the individual leg GRF_z is estimated by assuming the projection of each ankle joint on the ground as the individual leg CoP position:

$$\begin{bmatrix} GRF_z^L \\ GRF_z^R \end{bmatrix} = \begin{bmatrix} |y_{cop}^T - y_a^R| \\ |y_{cop}^T - y_a^L| \end{bmatrix} \frac{GRF_z^T}{|y_a^L - y_a^R|} \tag{5}$$

The desired hip flexion/extension torque applied by the exoskeleton τ_{hExo} can be computed by combining (2-5). To accommodate for differences in subject height h, we normalized the hip stiffness c with h:

$$\tau_{hExo} = h\hat{c}F\left(\varphi_0 - \varphi\right) \tag{6}$$

φ in (2) is the virtual hip angle which is the angle between trunk axis and the vector from ankle to the hip joint (shown in Fig. 1C). In LOPES II, the trunk axis angle is fixed and set to zero. Ankle position $\mathbf{p}_a$ was used to detect stance and swing phase of each individual leg (Vlutters et al., 2016; Zeni et al., 2008).

The controller has two parameters $(\hat{c}, \varphi_0)$ for each leg. In this study we set each parameter to the same value for both legs by assuming subjects walk symmetrically. In order to find appropriate control parameters, we hand-tuned the parameters based on the previous study (Zhao et al., 2017) for two pilot subjects before the experiment by gradually increasing the parameters till both of them felt most comfortable. The parameter values used in the experiment are shown in Table 1. The test subjects did not participate in the experiment.

In order to investigate the effectiveness of the force modulation in FMCH controller on human walking gait, we also implemented a constant compliant hip (CCH) controller in which the leg force was set to a constant value (subject body weight):

$$\tau_{hExo} = h\hat{c}mg\left(\varphi_0 - \varphi\right) \tag{7}$$

where m and g denotes subject body mass and gravitational acceleration.

Both FMCH and CCH controllers were implemented in Matlab (R2015b, MathWorks) using Simulink Real-time toolbox with a control frequency of 1 kHz.

6.3.3 Experimental protocol

Eight subjects (5 females, 3 males, age 26±4.0 years, height 1.75±0.04 m, weight 67.9±6.2 kg, mean ± std.) participated in this study. All subjects were healthy without any known neuromuscular injury or

functional impairment. They had no previous experience of walking with FMCH or CCH controller in LOPES II. They voluntarily signed an informed consent form approved by the Medical Ethics Committee Twente.

In order to familiarize with the exoskeleton and the experimental setup, each subject had a test walking trail (5 min) with the exoskeleton in transparent, FMCH and CCH mode. Then subjects had 5 min resting time before the experimental trials. During the experiment, subjects were instructed to wear the exoskeleton and walk on the treadmill with natural arm swing at a constant speed of 0.7 m/s. The speed is limited due to safety constraints of LOPES II. At the beginning of walking trials, a 3 min standing (wearing the exoskeleton) session was performed to measure the baseline (steady-state standing) metabolic cost. Then subjects walked for three 7-minute bouts, i.e. walking with transparent, FMCH, and CCH controller. Subjects rested for about 3 min in between walking bouts to prevent fatigue. The three walking bouts were randomized to avoid baseline and learning effects.

Subject hip and knee kinematic data and human-exoskeleton interaction torques were collected by LOPES II at 1 kHz. Seven right leg muscles (tibialis anterior (TIA), soleus (SOL), medial gastrocnemius (GAS), vastus medialis (VAS), rectus femoris (REC), hamstring (HAM), and gluteus maximus (GLU)) surface electromyography (EMG) signals were recorded (Delsys Inc., Natick, USA) at 1 kHz. Metabolic cost rate was assessed by measuring subject oxygen consumption rate and carbon dioxide output rate evey ten seconds (K5, Cosmed, Roma, Italy).

6.3.4 Data processing

To avoid adaptation effects, only the last three minutes of data in each condition were processed and analyzed. EMG data were high-pass filtered at 20 Hz (4th order zero-lag Butterworth), detrended, rectified, and then low-pass filtered at 6 Hz (4th order zero-lag Butterworth). Then each muscle EMG data were normalized to the average maximum EMG value during all the gait cycles in the transparent mode. The root mean square (r.m.s) of muscle EMG during each gait cycle was computed to quantify changes in EMG amplitude and indicate muscle activation level. Then each muscle r.m.s EMG data were normalized to the mean r.m.s EMG in the transparent condition. Joint angles and exoskeleton hip torques were low-pass filtered at 20 Hz and 4 Hz (4th order zero-lag Butterworth), respectively. The exoskeleton hip mechanical power was computed by multiplying exoskeleton hip torque and the time derivative of hip angle. The mean and standard deviation of exerted joint torque and power were computed after normalizing the data to each subject's body mass. The metabolic cost rate was calculated using the Brockway equation (Brockway, 1987). For better presenting the data, the subject order was sorted according to the mean of net metabolic cost rate reduction in FMCH and CCH mode. All data were processed with Matlab (R2018b, MathWorks) scripts.

6.3.5 Statistics

For each condition (i.e. transparent, FMCH and CCH), means and standard deviations of peak joint angle, muscle r.m.s EMG, net metabolic cost rate, exoskeleton torque, power and mechanical energy were computed across participants with standard deviation indicating inter-participant variability. Jarque-Bera test was used for checking if peak joint angle, muscle r.m.s EMG and net metabolic cost rate were normally distributed in each condition. If the data were normally distributed, one-way repeated mea-

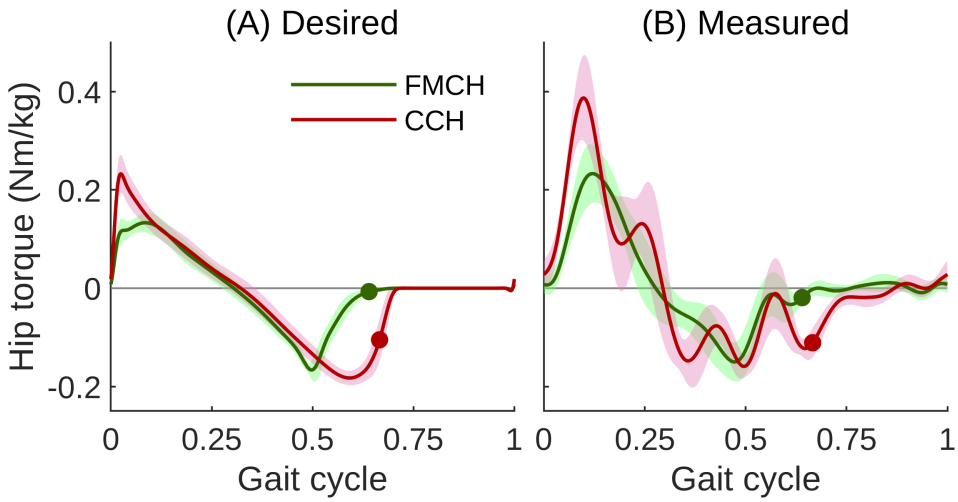

Figure 4: The normalized hip extension/flexion torque (difference between the FMCH/CCH and the transparent mode) applied by exoskeleton. Positive values denote the extension torques. The desired and measured torques are shown in the subfigure (a) and (b), respectively. FMCH and CCH are shown in red and green color, respectively. Solid lines denote the mean value of all eight subjects. Error bands denote ± 1 standard deviation. Circle markers indicate the toe-off.

sures analysis of variance (ANOVA) was performed across three conditions (i.e. transparent, FMCH and CCH). Otherwise the nonparametric Friedman test were performed. Mauchly test was used to evaluate sphericity. The Greenhouse-Geiser correction was applied if the sphericity assumption was violated. If the repeated measures ANOVA or the Friedman test indicated a significant effect, the paired t-test was used for *post hoc* tests. The paired t-test was performed between FMCH and CCH condition for exoskeleton peak torque, power and mechanical energy. p values less than or equal to 0.05 were considered as indicators of statistical significance. All statistical tests were conducted in Matlab (R2018b, MathWorks).

6.4 Results

6.4.1 Exoskeleton torque and power

CCH generated larger desired hip torque than FMCH for both extension and flexion (Fig. 4). The desired torque in CCH has much sharper increasing and decreasing edges compared to FMCH. The measured peak torque in FMCH is smaller than in CCH ($0.149 \pm 0.064\,\mathrm{N\,m/kg}$, $p < 0.001$). Both FMCH and CCH generate similar hip torque pattern during mid-stance phase ($15 \sim 35\%$ of gait cycle), while the measured torque in CCH has larger oscillations in both stance phase and swing phase compared to FMCH. The peak hip extension torque in CCH occurs earlier than in FMCH, while the peak hip flexion torque in FMCH occurs earlier than in CCH.

Similar to the measured torque, the measured mechanical power in CCH also has more oscillations than FMCH. Compared to CCH, FMCH requires less mechanical peak power ($0.603 \pm 0.180\,\mathrm{W/kg}$ in CCH, $0.322 \pm 0.137\,\mathrm{W/kg}$ in FMCH, $p < 0.001$) for the exoskeleton (Fig. 5). The averaged mechanical energy applied by the exoskeleton over one gait cycle in FMCH ($0.1206 \pm 0.0246\,\mathrm{J/kg}$) is also significantly ($p < 0.001$) lower than CCH ($0.2069 \pm 0.0287\,\mathrm{J/kg}$).

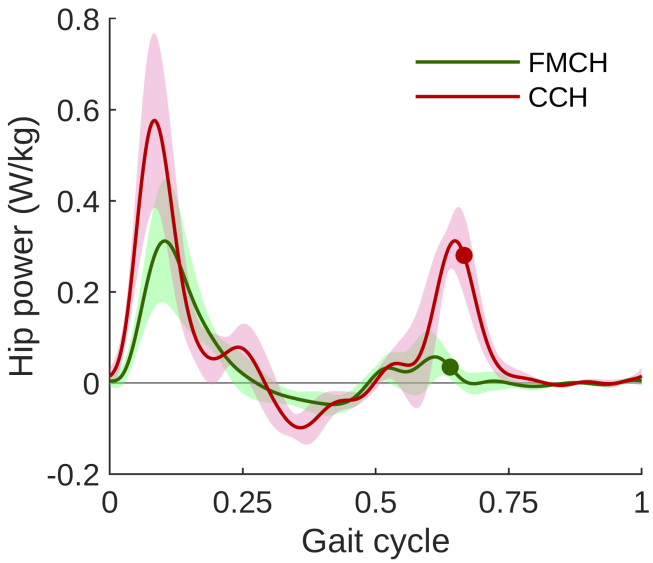

Figure 5: The measured hip mechanical power (normalized to subject body mass) applied by the exoskeleton. FMCH and CCH are shown in green and red color, respectively. Solid lines denote the mean values of all eight subjects. Error bands denote ± 1 standard deviation. Circle markers indicate the toe-off.

6.4.2 Joint kinematics

The hip and knee join angle patterns during the gait cycle are similar in transparent, FMCH, and CCH mode. Compared to the transparent mode, the peak of the hip adduction angle is not significantly different in neither FMCH nor CCH mode. Hip maximum extension angle during stance phase in FMCH is significantly smaller than in transparent mode ($1.7^\circ \pm 1.4^\circ$, $p = 0.014$). Hip maximum flexion angle during swing phase in both FMCH and CCH is significantly different from the transparent mode (FMCH is $1.4^\circ \pm 1.07^\circ$ smaller, $p = 0.008$; CCH is $2.3^\circ \pm 2.1^\circ$ larger, $p = 0.019$). Knee maximum flexion angle during the flight phase in CCH is significantly larger than in the transparent mode ($6.2^\circ \pm 3.0^\circ$, $p < 0.001$). Both hip and knee joints in FMCH and CCH during the early stance phase ($0 \sim 20\%$ of gait cycle) extend faster than in transparent mode.

6.4.3 Muscle activation

Fig. 7 shows the mean normalized EMG pattern across all eight subjects. All eight muscle activation patterns are similar between transparent, FMCH and CCH modes. There are no significant changes for the peak activation of all muslces.

The mean of normalized r.m.s EMG of all muscles which are attached to the thigh (i.e. GAS, VAS, REC, HAM and GLU) show reductions in FMCH (Fig. 8). HAM shows the largest reduction ($20.9 \pm 8.7\%$, $p < 0.001$) while REC activation keeps almost the same as the transparent in FMCH. GAS also shows significant reduction ($5.5 \pm 5.6\%$, $p = 0.028$) in FMCH compared to the transparent mode which is also shown in Fig. 7. GAS, VAS and GLU show similar amount of reductions in both FMCH and CCH.

Different subjects have different responses in terms of muscle activation to FMCH and CCH (Fig. 9). However, compared to CCH, FMCH has more consistent muscle responses. Compared to transparent mode, HAM activation has significant reduction for all subjects in FMCH. In contrast, only four subjects

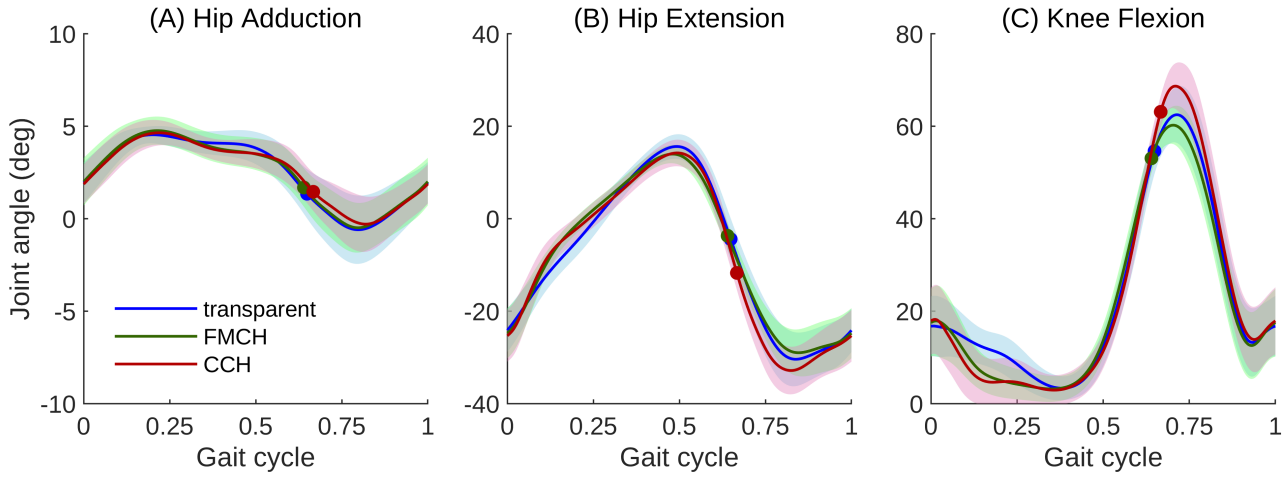

Figure 6: Joint kinematics during the gait cycle. Hip adduction and extension are shown as positive in the subfigure (A) and (B). Knee flexion is shown as positive in the subfigure (C). Transparent, FMCH, and CCH mode walking are shown in blue, red, and green color, respectively. Solid lines denote the subject mean. Error bands denote ± 1 standard deviation. Circle markers indicate the take-off (TO).

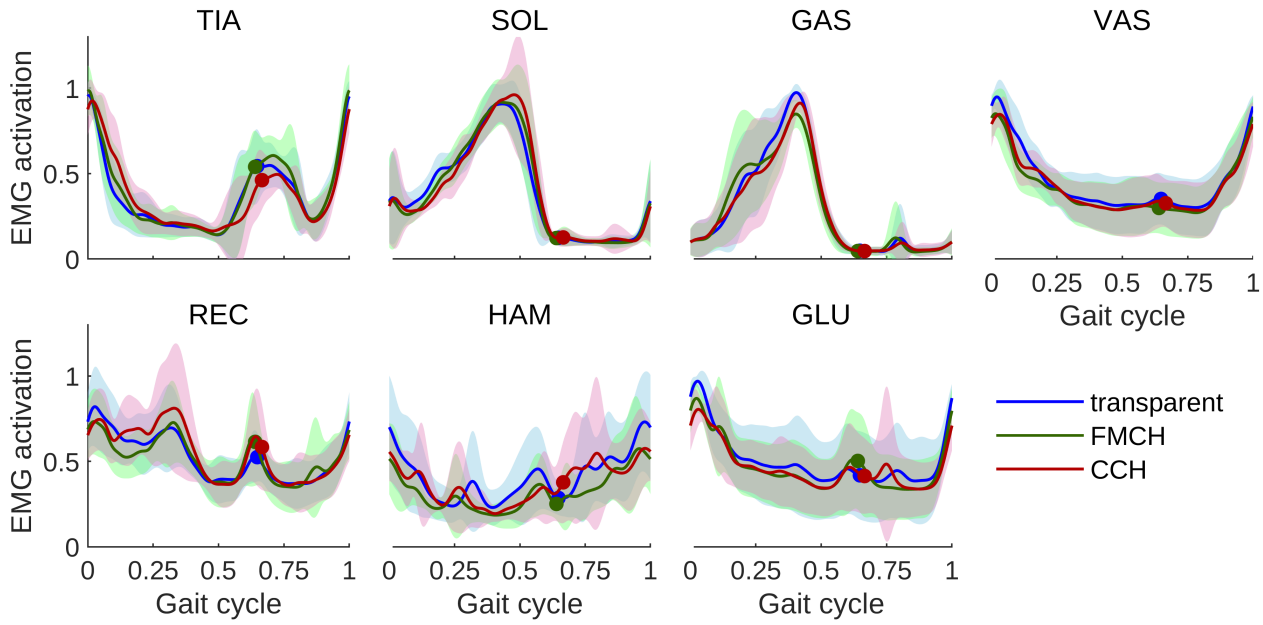

Figure 7: Normalized electromyography (EMG) of tibialis anterior (TIA), soleus (SOL), gastrocnemius medialis (GAS), vastus medialis (VAS), rectus femoris (REC), hamstring (HAM), and gluteus maximus (GLU) muscle during the gait cycle. Solid lines denote the mean values of all eight subjects. Error bands denote ± 1 standard deviation. Transparent, FMCH, and CCH mode walking are shown in blue, red, and green color, respectively. Circle markers indicate the take-off (TO).

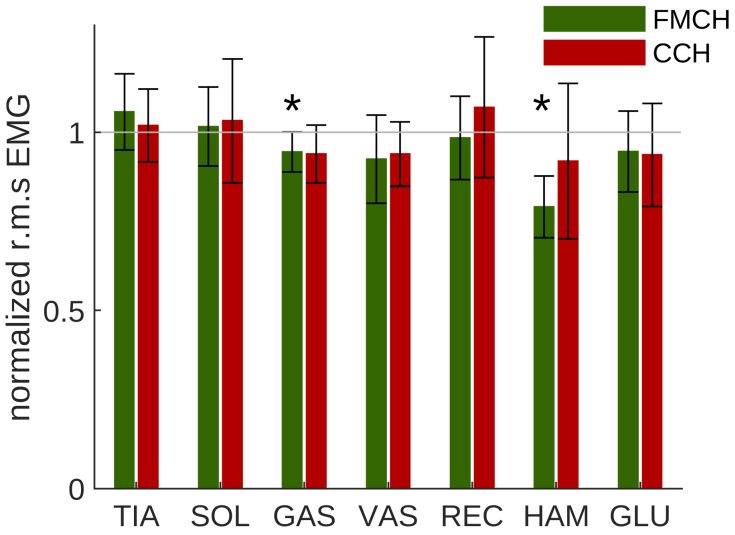

Figure 8: Normalized root mean square electromyography (r.m.s. EMG) of tibialis anterior (TIA), soleus (SOL), gastrocnemius medialis (GAS), vastusmedialis (VAS), rectus femoris (REC), hamstring (HAM), and gluteus maximus (GLU) during the gait cycle. It is normalized to the r.m.s EMG in the transparent mode. The bar height denotes the mean values of all eight subjects. The error-bar denotes ± 1 standard deviation. FMCH and CCH mode are shown in red and green bar, respectively. Asterisks indicate that the EMG reduction is significant compared to the transparent mode.

have HAM reduction in CCH (Fig. 9). Overall EMG reduction of all muscles is smaller in CCH than in FMCH. TIA is the least responsive muscle to both FMCH (three subjects) and CCH (four subjects) controllers. The changes in muscle activation varies quite a lot individually (e.g. SOL, REC and HAM) in CCH.

Subject 1 and 4 with high metabolic cost reduction show EMG reductions in all muscles except TIA which is not significant in FMCH. Subject 2 shows second highest metabolic cost reduction with FMCH has high reduction in VAS and HAM, but REC and GLU activation increased. Subject 1 and 3 with high metabolic cost reduction in CCH have an increase in muscles activation in three and two muscles, respectively.

6.4.4 Metabolic cost

Compared to the transparent mode, seven out of eight subjects show a reduced net metabolic cost rate (Fig. 10) in both FMCH and CCH mode. The average reduction of all eight subjects in FMCH mode is $6.0 \pm 11.4\%$ which is not significant ($p = 0.128$), while the CCH mode has significant reduction of $7.8 \pm 6.8\%$ ($p = 0.018$). Subject 1 has the highest metabolic reduction in both FMCH (24.1%) and CCH (17.7%). Only subject 8 shows a metabolic increase in both FMCH (15.3%) and CCH (3.7%).

6.5 Discussions

In this paper, a new bio-inspired reflex-based approach was presented and applied for control of an exoskeleton to assist human walking. With both modulated and fixed hip compliance controller, we found reductions in the average net metabolic rate and muscle activation. Compared to the fixed hip compli-

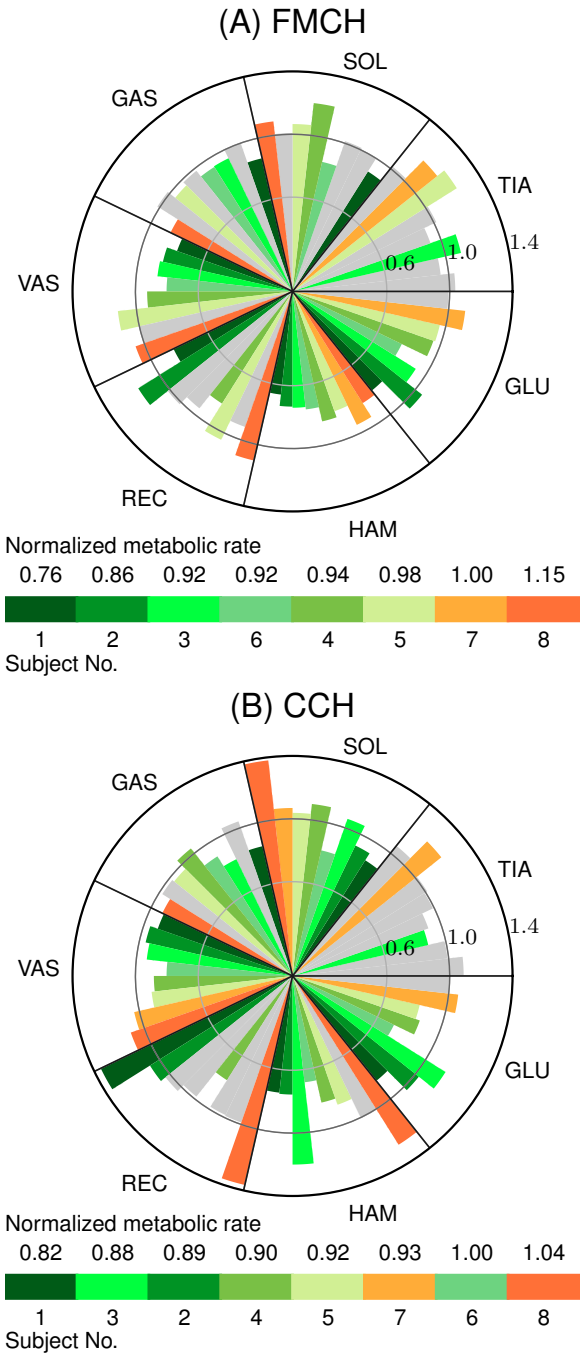

Figure 9: Individual normalized root mean square electromyography (r.m.s EMG) of tibialis anterior (TIA), soleus (SOL), gastrocnemius medialis (GAS), vastus medialis (VAS), rectus femoris (REC), hamstring (HAM), and gluteus maximus (GLU) muscle of all eight subjects walking with (A) FMCH controller, and (B) CCH controller. The r.m.s EMG is represented as the radius. The color denotes the subject specific normalized metabolic rate. The r.m.s EMG is normalized to the transparent mode (e.g. the muscle activation is reduced in FMCH mode compared to transparent mode if the bar height is smaller than 1). Different subjects are denoted with different colors. Gray color denotes that the muscle activation is not significantly different to the transparent mode. Normalized net metabolic cost rate value of each subject is shown above the legend bar. Subject No. is shown below the legend bar.

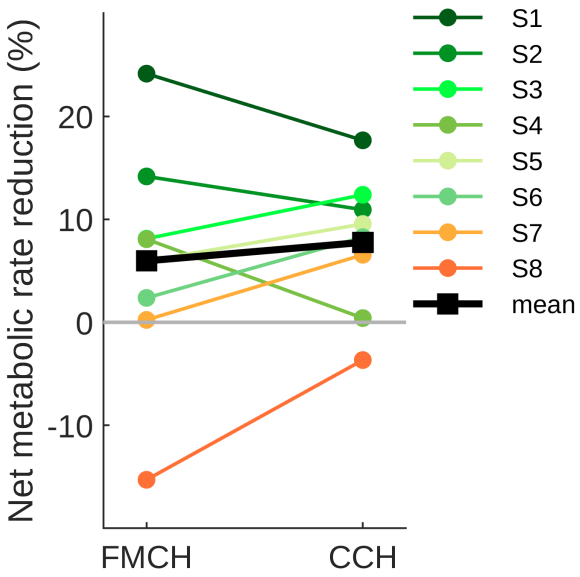

Figure 10: Net metabolic cost rate reduction of all eight subjects in the FMCH and CCH mode compared to the transparent mode. S1 to S8 indicate eight subjects. Mean reduction are shown in black color.

ance, modulation using leg force results in more natural kinematic behavior, more consistent reduction in muscle activities, smoother motor torques and less peak power from the exoskeleton.

It has been shown that the muscle positive force feedback is beneficial for the motion stability in locomotor control (Prochazka et al., 1997). The modulated hip compliance based on leg force controller mimics this force feedback pathway during human gait (Sharbafi and Seyfarth, 2015). We have previously investigated FMCH bio-inspired posture control concept using biarticular thigh actuation for assistance with an exosuit using a neuromuscular model (Sharbafi et al., 2018). Additionally, we implemented this concept in an exoskeleton by emulating biarticular muscles with single joint actuation at hip and knee (Zhao et al., 2017), in contrast to here presented study which is focused on hip actuation. Although the trunk angle is fixed in this study, the posture control based assistance can still result in reduction in both muscle activation and metabolic costs. This could be because human hip control remains consistent even if the posture control is not an issue.

6.5.1 Joint kinematic patterns are preserved

From analyzing the kinematic behavior with the exoskeleton, the joint angle patterns do not change too much (e.g. less than 10% difference in joint angle peaks) in all three control schemes (i.e. transparent, FMCH, and CCH). This demonstrates that both FMCH and CCH can preserve the kinematic patterns. The hip joint maximum extension and flexion angle in FMCH is a bit smaller than in the transparent mode. In contrast, CCH results in larger maximum flexion angle for both hip and knee joint compared to the transparent mode. This suggests that FMCH only affects the hip flexion/extension joint kinematics while CCH affects both hip and knee joint kinematics.

Another finding is prolonged straight knee configurations during stance phase with both FMCH and CCH (Fig. 6). This indicates that providing parallel hip compliance at the beginning of stance phase is beneficial for human gait as it supports straight stance leg configuration which can reduce knee extensors

activation and result in lower metabolic costs. In a study using a clutchable ankle spring, 7.2% metabolic cost reduction during walking (Collins et al., 2015) was found. This is in agreement with our results that switchable joint compliance (both FMCH and CCH, Fig. 10) can provide metabolic benefits during human gait. But it is important to note that this could also lead to load the knee joint in the straight configuration. A knee assistance control could be added in the future to prevent this.

6.5.2 FMCH based controller is more efficient

The efficiency of a control approach can be evaluated based on the energy consumption not only of the human body but also of the assistive device. Although both FMCH and CCH provide almost the same amount of metabolic cost rate reduction (Fig. 10), the mechanical peak power applied by the exoskeleton over one gait cycle in CCH is about twice as high as in FMCH (Fig. 5). This suggests that control of the exoskeleton with the FMCH approach is more efficient than the CCH. The oscillations in the hip power patterns in CCH is originated from the hip torque oscillations. In fact, both FMCH and CCH generate human-like hip torque pattern, but the measured torque in FMCH is much smoother than CCH (Fig. 4). Such fluctuations are due to sharp changes in the desired hip torque with CCH control right after TD (Fig. 4). This indicates that the bio-inspired FMCH approach provides benefits to reduce the peak torque and power at the hip joint and a smoother profile of the hip torque pattern. This facilitates not only human gait but also the implementation in assistive devices such as exoskeletons.

Energy injection in the first half of the stance phase can contribute to the postural control (Maus et al., 2010). The hip extension torques lead to a vertical alignment of the GRF vector and thus reduces the risk of foot slipping at early ground contact. Thus, energy injection at the hip joint right after TD can improve traction control in legged locomotion while decelerating the upper body forward rotation. This initiates the pendulum-like body movement described in the VPP concept (Maus et al., 2010). Furthermore, this active hip extension torque in early stance phase can support not only the upright trunk posture but also the forward acceleration of the contralateral leg to initiate the swing movement. In the second half of stance phase, first the exo generates negative power (significantly smaller compared to the positive power in the first half). This contributes to keep the upper body upright by dissipating part of the injected energy. Afterwards, the hip supports leg swing with active hip flexion torque and accelerating the thigh forward. This results in a second energy injection phase (Fig. 5), which has similar effects as the positive power in the first half of stance phase and also supports the pre-swing movement. Hence, the proposed control methods contribute to the forward rotation of the swing leg, which is driven by the hip torques during stance phase.

6.5.3 FMCH based controller has higher consistency in EMG responses

Analyzing muscle activation (Fig. 8 and Fig. 9), demonstrate successful transfer and application of bio-inspired control models based on human walking dynamics. The following general behaviours are observable from muscle reactions to assistance: 1) consistent and significant reduction in HAM and GAS muscle for all subjects using FMCH method (Fig. 8 and 9); 2) non-significant but consistent reductions in mean normalized activity in all other hip and knee muscles in both FMCH and CCH except REC in CCH (Fig. 8); 3) more consistent muscle responses (Fig. 9) and higher reduction in muscle activities (Fig. 8) in different subjects with FMCH compared to CCH. These results show that the leg force feedback improves

assistance level with respect to reduction in muscle activation, as predicted by our bio-inspired gait models (Sharbafi et al., 2018). In line with improving locomotion function (e.g. regarding kinematics and power consumption), by analyzing activities in different muscles, the exoskeleton can provide essential assistance to a specific muscle group (e.g. HAM). Significant reductions in HAM and GAS muscles using FMCH method are in agreement with previous findings in (Zhao et al., 2017) using two-joint actuation at hip and knee. In our compliant hip approaches, the applied torque to the upper part of thigh segment has positive effects on the muscles acting on this segment. Comparison between CCH and FMCH in Fig. 8 shows clear reductions in thigh biarticular muscles activities, obtained by using leg force feedback in FMCH. This is in agreement with the implementation of VPP concept through FMCH and biarticular thigh actuation in simulated walking models (Sharbafi et al., 2017b) and a bipedal robot (Sharbafi et al., 2016).

Higher consistency between different subjects' muscle responses in FMCH compared to CCH (Fig. 9) shows that the feedback (reflex) control enhances the adaptability of the user to the assistive device. Assistance of the exoskeleton after TD and at the push-off phase supports the pre-swing leg function as well. In addition, support of the exoskeleton in the second half of stance phase contributes to redirecting the CoM velocity before TD of the contralateral swing leg. This is in line with the significant reduction in hip extensor muscles (HAM and GLU) during swing phase.

As gait assistance needs appropriate interaction with human movement, bio-inspired design and control approaches provide clear advantages. In the recent years, introducing wearable (soft) assistive devices called exosuits (Asbeck et al., 2015b), (Asbeck et al., 2015a), (Ding et al., 2018) was a breakthrough enabling novel bio-inspired designs for assistive systems. In this paper, we introduced a simple bio-inspired control method which enables a new approach for assistance toward a more collaborative instead of master-slave relation between human and machine. The novel FMCH based controller reacts to human action within a bio-inspired control framework. Previous experimental and simulation studies have shown that FMCH is a feasible control concept for balance (Sharbafi et al., 2017b; Sharbafi and Seyfarth, 2015). Here, we found that the exoskeleton can assist human by using the same feedback design. Our template based approach avoids the model complexity which is a common drawback of such approaches (Yan et al., 2015). It is the first implementation of such a novel method on a single (hip) joint actuated exoskeleton demonstrated beneficial outcomes regarding reducing metabolic costs and muscle activities compared to similar studies (only with hip joint assistance) on exoskeletons (Lenzi et al., 2013; Seo et al., 2016; Wu et al., 2015) or exosuits (Asbeck et al., 2015a; Young et al., 2017).

6.5.4 Limitations

In this study, we are focusing on assisting the hip joints to investigate the benefits of FMCH based controller for walking energetics. Although the FMCH controller is a bio-inspired posture control concept, the posture stability and balance performance during walking cannot be investigated because of the hardware limitations of LOPES II (the trunk angle is fixed and set to zero during walking). This feature can be investigated with other hip exoskeletons in the future.

Another limitation of this study is that we used a fixed control parameter set for all subjects. Although the parameters were normalized to subject body weight and body height, it could still lower the performance of the proposed method. This is because different subjects have different gait characteristics

which are not related to individual body weight and height (e.g. hip rest angle). This could explain the different responses to the controller across different subjects. For instance, subject 8 showed increased net metabolic cost rate in both FMCH and CCH while all other subjects showed the opposite (Fig. 10). Studies have shown that applying subject specific control parameters with human-in-the-loop optimization approach can improve the level of assistance (Ding et al., 2018; Zhang et al., 2017). In further research our FMCH controller could be combined with human-in-the-loop optimization method to find the individualized control parameters.

Using a minor control interference, as employing leg force to proportionally tune hip stiffness (in FMCH), provides clear advantages compared to the constant hip stiffness design (CCH). A simple proportional gain modulation is sufficient to achieve the observed enhancement in assistance. With our findings we have shown that the FMCH control concept, which is originally for balance control, can provide assistance for walking gait. Still, the swing leg control is one missing part in the proposed method as the exoskeleton operates in transparent mode during swing phase. We have started to extend our bio-inspired methodology to assist subjects during swing phase (e.g. using the biarticular mechanism as presented in (Sharbafi et al., 2017a)). In that respect, a preliminary version of an exosuit with biarticular thigh muscles was developed (Sharbafi et al., 2018). Mimicking muscle properties such as compliance, morphology, biarticular actuation and reflex-based (e.g. force feedback in FMCH) control are important design and control features of novel bio-inspired assistive devices.

Acknowledgment

This work was supported by the BALANCE (Balance Augmentation in Locomotion, through Anticipative, Natural and Cooperative control of Exoskeletons) project, which is partially funded under grant 601003 of the Seventh Framework Program (FP7) of the European Commission (Information and Communication Technologies, ICT-2011.2.1).

Author contributions

Guoping Zhao is the main and corresponding author of this paper. Guoping Zhao implemented the controller on the LOPES II. All authors contributed to the design of the experiment. Guoping Zhao and Mark Vlutters conducted the experiment. Guoping Zhao processed and analyzed the data. Guoping Zhao and Maziar Sharbafi drafted the manuscript. All authors interpreted the data and revised the manuscript.

References

Asbeck, A. T., De Rossi, S. M., Holt, K. G., and Walsh, C. J. (2015a). A biologically inspired soft exosuit for walking assistance. *The International Journal of Robotics Research*, 34(6):744–762.

Asbeck, A. T., Dyer, R. J., Larusson, A. F., and Walsh, C. J. (2013). Biologically-inspired soft exosuit. In *Rehabilitation robotics (ICORR), 2013 IEEE international conference on*, pages 1–8. IEEE.

Asbeck, A. T., Schmidt, K., and Walsh, C. J. (2015b). Soft exosuit for hip assistance. *Robotics and Autonomous Systems*, 73:102–110.

Bizzi, E., Cheung, V., d'Avella, A., Saltiel, P., and Tresch, M. (2008). Combining modules for movement. *Brain Research Reviews*, 57(1):125 – 133. Networks in Motion.

Brockway, J. (1987). Derivation of formulae used to calculate energy expenditure in man. *Human nutrition. Clinical nutrition*, 41(6):463—471.

Brown, I. E. and Loeb, G. E. (2000). *A Reductionist Approach to Creating and Using Neuromusculoskeletal Models*, pages 148–163. Springer New York, New York, NY.

Chen, F., Yu, Y., Ge, Y., and Fang, Y. (2009). Wpal for human power assist during walking using dynamic equation. In *Mechatronics and Automation, 2009. ICMA 2009. International Conference on*, pages 1039–1043. IEEE.

Collins, S. H., Wiggin, M. B., and Sawicki, G. S. (2015). Reducing the energy cost of human walking using an unpowered exoskeleton. *Nature*, 522(7555):212.

Dietz, V. (2002). Proprioception and locomotor disorders. *Nature Reviews Neuroscience*, 3(10):781–790.

Ding, Y., Kim, M., Kuindersma, S., and Walsh, C. J. (2018). Human-in-the-loop optimization of hip assistance with a soft exosuit during walking. *Science Robotics*, 3(15):eaar5438.

Dzeladini, F., Wu, A. R., Renjewski, D., Arami, A., Burdet, E., van Asseldonk, E., van der Kooij, H., and Ijspeert, A. J. (2016). Effects of a neuromuscular controller on a powered ankle exoskeleton during human walking. In *2016 6th IEEE International Conference on Biomedical Robotics and Biomechatronics (BioRob)*, pages 617–622.

Esquenazi, A., Talaty, M., Packel, A., and Saulino, M. (2012). The rewalk powered exoskeleton to restore ambulatory function to individuals with thoracic-level motor-complete spinal cord injury. *American journal of physical medicine & rehabilitation*, 91(11):911–921.

Farris, D. J. and Sawicki, G. S. (2012). The mechanics and energetics of human walking and running: a joint level perspective. *Journal of The Royal Society Interface*, 9(66):110–118.

Fleischer, C. and Hommel, G. (2008). A human–exoskeleton interface utilizing electromyography. *IEEE Transactions on Robotics*, 24(4):872–882.

Gerasimenko, Y., Roy, R. R., and Edgerton, V. R. (2008). Epidural stimulation: Comparison of the spinal circuits that generate and control locomotion in rats, cats and humans. *Experimental Neurology*, 209(2):417 – 425. Regeneration and Rehabilitation after Spinal Cord Injury.

Geyer, H. and Herr, H. (2010). A muscle-reflex model that encodes principles of legged mechanics produces human walking dynamics and muscle activities. *IEEE Transactions on neural systems and rehabilitation engineering*, 18(3):263–273.

Giovacchini, F., Vannetti, F., Fantozzi, M., Cempini, M., Cortese, M., Parri, A., Yan, T., Lefeber, D., and Vitiello, N. (2015). A light-weight active orthosis for hip movement assistance. *Robotics and Autonomous Systems*, 73:123–134.

Grimmer, M., Riener, R., Walsh, C. J., and Seyfarth, A. (2019). Mobility related physical and functional losses due to aging and disease-a motivation for lower limb exoskeletons. *Journal of neuroengineering and rehabilitation*, 16(1):2.

Harkema, S., Gerasimenko, Y., Hodes, J., Burdick, J., Angeli, C., Chen, Y., Ferreira, C., Willhite, A., Rejc, E., Grossman, R. G., and Edgerton, V. R. (2011). Effect of epidural stimulation of the lumbosacral spinal cord on voluntary movement, standing, and assisted stepping after motor complete paraplegia: a case study. *The Lancet*, 377(9781):1938 – 1947.

He, H. and Kiguchi, K. (2007). A study on emg-based control of exoskeleton robots for human lower-limb motion assist. In *Information Technology Applications in Biomedicine, 2007. ITAB 2007. 6th International Special Topic Conference on*, pages 292–295. IEEE.

Hyon, S.-H., Morimoto, J., Matsubara, T., Noda, T., and Kawato, M. (2011). Xor: Hybrid drive exoskeleton robot that can balance. In *Intelligent Robots and Systems (IROS), 2011 IEEE/RSJ International Conference on*, pages 3975–3981. IEEE.

Ijspeert, A. J. (2008). Central pattern generators for locomotion control in animals and robots: a review. *Neural networks*, 21(4):642–653.

Kao, P.-C., Lewis, C. L., and Ferris, D. P. (2010). Invariant ankle moment patterns when walking with and without a robotic ankle exoskeleton. *Journal of biomechanics*, 43(2):203–209.

Kawamoto, H., Taal, S., Niniss, H., Hayashi, T., Kamibayashi, K., Eguchi, K., and Sankai, Y. (2010). Voluntary motion support control of robot suit hal triggered by bioelectrical signal for hemiplegia. In *Engineering in Medicine and Biology Society (EMBC), 2010 Annual International Conference of the IEEE*, pages 462–466. IEEE.

Kazerooni, H., Steger, R., and Huang, L. (2006). Hybrid control of the berkeley lower extremity exoskeleton (bleex). *The International Journal of Robotics Research*, 25(5-6):561–573.

Kong, K. and Jeon, D. (2006). Design and control of an exoskeleton for the elderly and patients. *IEEE/ASME Transactions on mechatronics*, 11(4):428–432.

Lenzi, T., Carrozza, M. C., and Agrawal, S. K. (2013). Powered hip exoskeletons can reduce the user's hip and ankle muscle activations during walking. *IEEE Transactions on Neural Systems and Rehabilitation Engineering*, 21(6):938–948.

Matsubara, T., Uchikata, A., and Morimoto, J. (2012). Full-body exoskeleton robot control for walking assistance by style-phase adaptive pattern generation. In *Intelligent Robots and Systems (IROS), 2012 IEEE/RSJ International Conference on*, pages 3914–3920. IEEE.

Maus, H.-M., Lipfert, S., Gross, M., Rummel, J., and Seyfarth, A. (2010). Upright human gait did not provide a major mechanical challenge for our ancestors. *Nature communications*, 1:70.

Meuleman, J., van Asseldonk, E., van Oort, G., Rietman, H., and van der Kooij, H. (2016). Lopes ii–design and evaluation of an admittance controlled gait training robot with shadow-leg approach. *IEEE Transactions on Neural Systems and Rehabilitation Engineering*, 24(3):352–363.

Mori, Y., Okada, J., and Takayama, K. (2006). Development of a standing style transfer system" able" for disabled lower limbs. *IEEE/ASME Transactions on Mechatronics*, 11(4):372–380.

Neuhaus, P. D., Noorden, J. H., Craig, T. J., Torres, T., Kirschbaum, J., and Pratt, J. E. (2011). Design and evaluation of mina: A robotic orthosis for paraplegics. In *Rehabilitation Robotics (ICORR), 2011 IEEE International Conference on*, pages 1–8. IEEE.

Norris, J. A., Granata, K. P., Mitros, M. R., Byrne, E. M., and Marsh, A. P. (2007). Effect of augmented plantarflexion power on preferred walking speed and economy in young and older adults. *Gait & posture*, 25(4):620–627.

Prochazka, A., Gillard, D., and Bennett, D. J. (1997). Positive force feedback control of muscles. *Journal of Neurophysiology*, 77(6):3226–3236. PMID: 9212270.

Ronsse, R., Lenzi, T., Vitiello, N., Koopman, B., van Asseldonk, E., De Rossi, S. M. M., van den Kieboom, J., van der Kooij, H., Carrozza, M. C., and Ijspeert, A. J. (2011a). Oscillator-based assistance of cyclical movements: model-based and model-free approaches. *Medical & biological engineering & computing*, 49(10):1173.

Ronsse, R., Lenzi, T., Vitiello, N., Koopman, B., van Asseldonk, E., De Rossi, S. M. M., van den Kieboom, J., van der Kooij, H., Carrozza, M. C., and Ijspeert, A. J. (2011b). Oscillator-based assistance of cyclical movements: model-based and model-free approaches. *Med Biol Eng Comput*, 49(10):1173–1185.

Ruiz Garate, V., Parri, A., Yan, T., Munih, M., Molino Lova, R., Vitiello, N., and Ronsse, R. (2016). Walking assistance using artificial primitives: A novel bioinspired framework using motor primitives for locomotion assistance through a wearable cooperative exoskeleton. *IEEE Robotics Automation Magazine*, 23(1):83–95.

Sankai, Y. (2010). Hal: Hybrid assistive limb based on cybernics. In *Robotics research*, pages 25–34. Springer.

Sanz-Merodio, D., Cestari, M., Arevalo, J. C., and Garcia, E. (2012). Control motion approach of a lower limb orthosis to reduce energy consumption. *International Journal of Advanced Robotic Systems*, 9(6):232.

Seo, K., Lee, J., Lee, Y., Ha, T., and Shim, Y. (2016). Fully autonomous hip exoskeleton saves metabolic cost of walking. In *Robotics and Automation (ICRA), 2016 IEEE International Conference on*, pages 4628–4635. IEEE.

Sharbafi, M., Barazesh, H., Iranikhah, M., and Seyfarth, A. (2018). Leg force control through biarticular muscles for human walking assistance. *Frontiers in Neurorobotics*, 12:39.

Sharbafi, M. A., Rashty, A. M. N., Rode, C., and Seyfarth, A. (2017a). Reconstruction of human swing leg motion with passive biarticular muscle models. *Human movement science*, 52:96–107.

Sharbafi, M. A., Rode, C., Kurowski, S., Scholz, D., Möckel, R., Radkhah, K., Zhao, G., Rashty, A. M., von Stryk, O., and Seyfarth, A. (2016). A new biarticular actuator design facilitates control of leg function in biobiped3. *Bioinspiration & biomimetics*, 11(4):046003.

Sharbafi, M. A. and Seyfarth, A. (2014). Stable running by leg force-modulated hip stiffness. In *Biomedical Robotics and Biomechatronics (2014 5th IEEE RAS & EMBS International Conference on*, pages 204–210. IEEE.

Sharbafi, M. A. and Seyfarth, A. (2015). Fmch: A new model for human-like postural control in walking. In *Intelligent Robots and Systems (IROS), 2015 IEEE/RSJ International Conference on*, pages 5742–5747. IEEE.

Sharbafi, M. A., Seyfarth, A., and Zhao, G. (2017b). Locomotor sub-functions for control of assistive wearable robots. *Frontiers in neurorobotics*, 11:44.

Song, S. and Geyer, H. (2015). A neural circuitry that emphasizes spinal feedback generates diverse behaviours of human locomotion. *The Journal of physiology*, 593(16):3493–3511.

Strausser, K. A. and Kazerooni, H. (2011). The development and testing of a human machine interface for a mobile medical exoskeleton. In *Intelligent Robots and Systems (IROS), 2011 IEEE/RSJ International Conference on*, pages 4911–4916. IEEE.

Tagliamonte, N. L., Sergi, F., Carpino, G., Accoto, D., and Guglielmelli, E. (2013). Human-robot interaction tests on a novel robot for gait assistance. In *Rehabilitation Robotics (ICORR), 2013 IEEE International Conference on*, pages 1–6. IEEE.

Vlutters, M., van Asseldonk, E. H. F., and van der Kooij, H. (2016). Center of mass velocity-based predictions in balance recovery following pelvis perturbations during human walking. *Journal of Experimental Biology*, 219(10):1514–1523.

Walsh, C. J., Pasch, K., and Herr, H. (2006). An autonomous, underactuated exoskeleton for load-carrying augmentation. In *2006 IEEE/RSJ International Conference on Intelligent Robots and Systems*, pages 1410–1415. IEEE.

Wang, S., Wang, L., Meijneke, C., van Asseldonk, E., Hoellinger, T., Cheron, G., Ivanenko, Y., Scaleia, V. L., Sylos-Labini, F., Molinari, M., Tamburella, F., Pisotta, I., Thorsteinsson, F., Ilzkovitz, M., Gancet, J., Nevatia, Y., Hauffe, R., Zanow, F., and van der Kooij, H. (2015). Design and control of the mindwalker exoskeleton. *IEEE Transactions on Neural Systems and Rehabilitation Engineering*, 23(2):277–286.

Wu, A. R., Dzeladini, F., Brug, T. J. H., Tamburella, F., Tagliamonte, N. L., van Asseldonk, E. H. F., van der Kooij, H., and Ijspeert, A. J. (2017). An adaptive neuromuscular controller for assistive lower-limb exoskeletons: A preliminary study on subjects with spinal cord injury. *Frontiers in Neurorobotics*, 11:30.

Wu, Q., Wang, X., Du, F., and Zhang, X. (2015). Design and control of a powered hip exoskeleton for walking assistance. *International Journal of Advanced Robotic Systems*, 12(3):18.

Yan, T., Cempini, M., Oddo, C. M., and Vitiello, N. (2015). Review of assistive strategies in powered lower-limb orthoses and exoskeletons. *Robotics and Autonomous Systems*, 64:120–136.

Yeh, T.-J., Wu, M.-J., Lu, T.-J., Wu, F.-K., and Huang, C.-R. (2010). Control of mckibben pneumatic muscles for a power-assist, lower-limb orthosis. *Mechatronics*, 20(6):686–697.

Young, A. J., Gannon, H., and Ferris, D. P. (2017). A Biomechanical Comparison of Proportional Electromyography Control to Biological Torque Control Using a Powered Hip Exoskeleton. *Frontiers in bioengineering and biotechnology*, 5:1182.

Zeni, J., Richards, J., and Higginson, J. (2008). Two simple methods for determining gait events during treadmill and overground walking using kinematic data. *Gait & Posture*, 27(4):710 – 714.

Zhang, J., Fiers, P., Witte, K. A., Jackson, R. W., Poggensee, K. L., Atkeson, C. G., and Collins, S. H. (2017). Human-in-the-loop optimization of exoskeleton assistance during walking. *Science*, 356(6344):1280–1284.

Zhang, X. and Hashimoto, M. (2011). Synchronization based control for walking assist suit-evaluation on synchronization and assist effect. In *Key Engineering Materials*, volume 464, pages 115–118. Trans Tech Publ.

Zhao, G., Sharbafi, M., Vlutters, M., Van Asseldonk, E., and Seyfarth, A. (2017). Template model inspired leg force feedback based control can assist human walking. In *Rehabilitation Robotics (ICORR), 2017 International Conference on*, pages 473–478. IEEE.

7 Article V: Bio-inspired neuromuscular reflex based hopping controller for a segmented robotic leg

Authors:

Guoping Zhao, Florian Szymanski, and Andre Seyfarth

Lauflabor Locomotion Laboratory, TU Darmstadt, Darmstadt, Germany

Submitted for publication in 2019

7.1 Abstract

It has been shown that human-like hopping can be achieved by muscle reflex control in the neuromechanical simulations. However, it is unclear if this concept is applicable and feasible for controlling a real robot. This paper presents a low-cost two-segmented robotic leg design and demonstrates the feasibility and the benefits of the bio-inspired neuromuscular reflex based control for hopping. Simulation models were developed to describe the dynamics of the real robot. Different neuromuscular reflex pathways were investigated with the simulation model. We found that stable hopping can be achieved with both positive muscle force and length feedback. And the hopping height can be controlled by modulating the muscle force feedback gains with the return maps. The force feedback neuromuscular reflex based controller is robust against body mass and ground impedance changes. In order to investigate the influences of the muscle properties on the hopping behavior, the hopping height return map of a simplified muscle model was compared with the normal muscle model. The results show that the muscle properties play an important role in stabilizing the movement, highlighting the importance of morphological computation. Finally, we implemented the controller on the real robot to prove the feasibility of the proposed neuromuscular reflex based control idea. The results of this paper demonstrate the neuromuscular reflex based control approach is feasible to implement and capable of achieving stable and robust hopping in a real robot. It provides a promising direction of controlling the legged robot to achieve robust dynamic motion in the future.

7.2 Introduction

The legged locomotion found in humans and animals are energetic, versatile, and robust against perturbations. The functionality of the leg can be separated into three locomotor sub-functions which are stance (axial leg function), swing (rotational leg function), and balance (trunk posture control) (Seyfarth et al., 2013). The stance sub-function is to support body weight and create the centre of mass bouncing behavior (e.g. during walking, running, etc.). Although human leg structure and the locomotion control are complex, highly simplified template models which emphasizing on the elastic stance leg function can describe and reproduce some basic characteristics of human walking and running gait (Full and Koditschek, 1999; Blickhan, 1989; Geyer et al., 2006). Hopping can be considered as a primitive motion which focuses on stance sub-function. A better understanding of how hopping motion is generated and controlled can help us further recognize the basic principles of human locomotion.

In general, the models proposed for explaining the stance leg function can be divided into two levels: mechanical level and neuromuscular level. Mechanical level models simplify the neuromuscular properties of major muscle groups in the stance leg and represent the stance leg function as a mechanical spring. For instance, a constant stiffness prismatic spring used in the spring loaded inverted pendulum (SLIP) template model is one of the simplest representation of the stance leg sub-function for dynamic locomotion (e.g. hopping, walking, running, etc.) (Blickhan, 1989; Geyer et al., 2006). But the constant stiffness spring model cannot describe the perturbation behaviors because it is energy conservative. Therefore, a few extended SLIP models were proposed. For instance, the ESLIP (Ludwig et al., 2012) model and VSLIP (Riese and Seyfarth, 2011) model modulate the spring stiffness and/or rest length during the locomotion to regulate the system energy.

The neuromuscular level models include the muscle properties (e.g. force-length and force-velocity relationship) and neural reflexes (e.g. muscle force, length, and velocity reflex). For instance, a two-segmented model with a point mass and a Hill-type extensor muscle was proposed in (Geyer et al., 2003) to explain the functionality of the positive force feedback in bouncing gaits. Recently, this model was used with linear reflex compositions for investigating the sensor-motor maps (Schumacher and Seyfarth, 2017). A further simplified model which ignore the leg geometric properties was used for demonstrating the role of intrinsic muscle properties and reflexes in generating stable hopping (Haeufle et al., 2012, 2010). With multi-segment and multi-muscles complex models, Geyer et al. showed that human-like stable and rich bipedal locomotion can be achieved with neural networks emphasizing on the muscle reflexes (Geyer and Herr, 2010; Song and Geyer, 2015). The neuromuscular reflex based controller proposed for these complex models have also been implemented on lower limb prostheses (Eilenberg et al., 2010; Thatte and Geyer, 2016) and exoskeletons (Ruiz Garate et al., 2016; Wu et al., 2017) to assist human walking.

Comparing to the mechanical level models, neuromuscular level models provide deeper insights on the potential benefits of muscle properties and the neural reflex control for generating bouncing gaits (e.g. hopping, walking, running, etc.). Although the hopping motion has been extensively studied with the simulation models mentioned above, it is unclear if the control concept is applicable and feasible for controlling a real hopping robot because most of the time the leg physical properties (e.g. leg inertial, foot-ground collision model, damping in the joint, etc.) are ignored in the simplified models. Therefore, in this paper, we focus on investigating if the bio-inspired neuromuscular reflex based controller can generate stable hopping on both the realistic simulation model and the real robot.

Lots of legged robots emphasizing the bouncing leg function were developed during the last few decades. They can be divided into three groups based on the actuator types: i) serial elastic actuators (SEAs, e.g. (Heim et al., 2018; Sharbafi et al., 2016; Zhu et al., 2016)), ii) soft actuators (e.g. pneumatic actuators, (Liu et al., 2018; Niiyama et al., 2007; Raibert, 1986)), iii) quasi-direct-drive (QDD) actuators (e.g. electric motors with low gear ratio gearboxes, (Ding and Park, 2017; Kalouche, 2017; Kenneally et al., 2016; Seok et al., 2015)). The intrinsic impedance in the SEAs and soft actuators can be beneficial for reducing the energetic cost and impact forces. But it is hard to modulate the intrinsic impedance during the motion. For the QDD actuators, we can control the impedance and emulate different actuator dynamics (e.g. springs, Hill-type muscles, etc.) with a virtual model control approach (Pratt et al., 2001). Besides, QDD actuators can potentially transfer kinetic energy back to electric energy by regenerative braking (Seok et al., 2015). Therefore, the QDD actuators were chosen for the robotic leg in this study.

The goal of this paper is to develop a low-cost robotic leg for hopping and demonstrate the benefits of the bio-inspired neuromuscular reflex based controller in both simulation and hardware experiments. In the following section, we first introduce a single leg robot hardware design (Section II). In order to investigate if the design and the hopping controller can be extended to the bipedal hopping, we also present a bipedal robot with the same design concept. Then the bio-inspired neuromuscular reflex based hopping controller is presented in Section III. Section V shows the results of the simulation and hardware experiments which demonstrates the feasibility and benefits of the bio-inspired controller. Section IV discusses the results and gives insights about this study and future work.

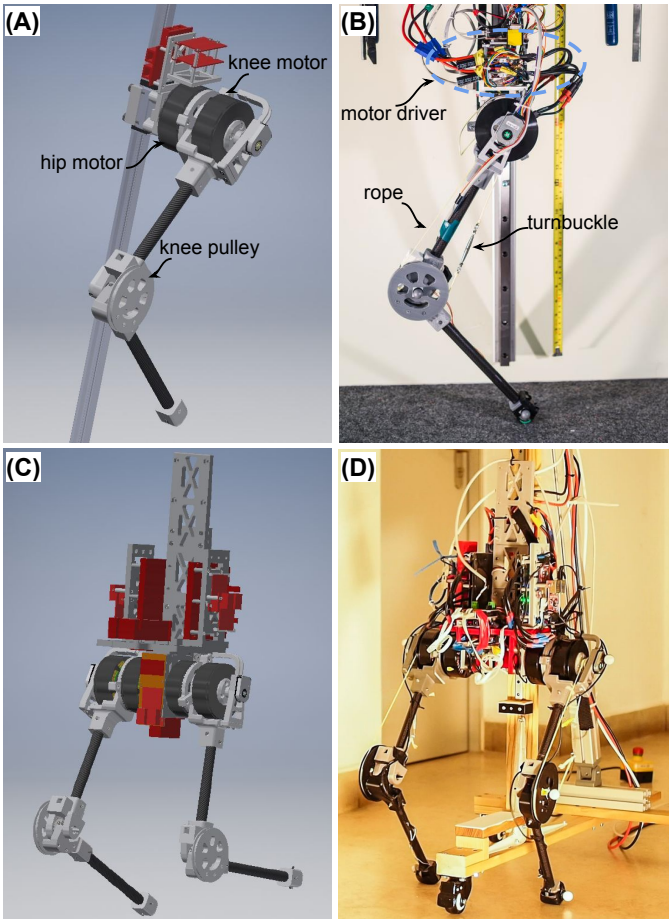

Figure 1: GURO robotic leg mechanical design. (A) The single leg robot CAD model (without ropes and electronic parts). (B) A photo of the single leg robot. (C) The bipedal robot CAD model (without ropes). (D) A photo of the bipedal robot.

7.3 Robot Hardware Design and Simulation

7.3.1 Mechanical design

The single leg robot consists of two BLDC motors (E8318-120KV, Hymotor, China) which control the hip and knee joint separately in the sagittal plane (Fig. 1(A) and (B)). The leg is serially actuated. To minimize the leg moment of inertia, the hip and knee motors are co-axially located at the top of the thigh. Knee joint is coupled with the knee motor shaft by a rope-pulley mechanism (gear-ratio 4:1). In order to avoid high mechanical stiffness and friction in the transmission chain, no gearbox is used for the motors. The direct-drive for the hip and the QDD for the knee actuation ensures the transparency between the motor and the external environment (Kenneally et al., 2016). This makes it possible to achieve relative good torque control performance by motor current sensing (without any force/torque sensors).

Carbon fiber tubes were chosen as the thigh and shank segment to withstand high load while keep the weight and the moment of inertia low. All other mechanical parts, except the screws and bearings, are 3D printed with plastic materials (PLA and ABS) to further reduce the robot weight and keep the cost low. The robot hip is fixed on a 1D linear guide rail so that we can focus on the leg extension function for hopping. The total mass of the robot is 2.8 kg. The thigh and shank segment length are 0.27 m.

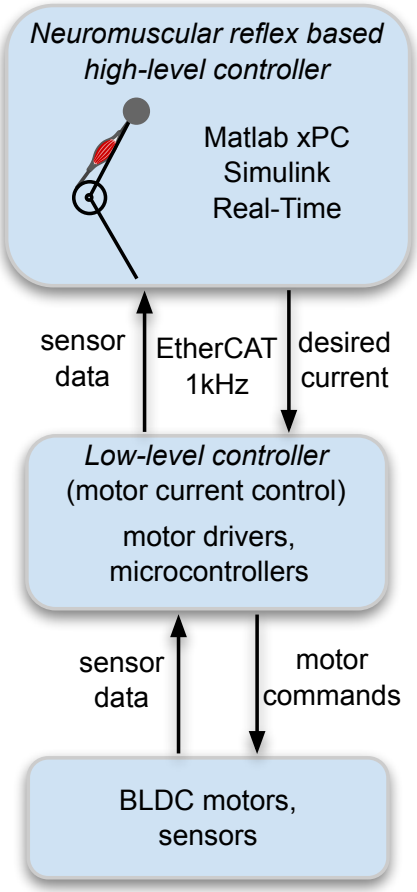

Figure 2: GURO robot control system architecture.

To test if the design is also suitable for bipedal hopping, a bipedal robot was built by connecting two single robotic leg with a trunk (Fig. 1(C) and (D)). Similar as the single leg robot, the trunk motion is also constrained in 1D (up and down movement) by a linear bearing. The total mass of the bipedal robot is 6.2 kg. To keep the maximum knee joint torque to robot mass ratio similar as the single leg robot, the gear-ratio of the bipedal robot leg knee motors (rope-pulley mechanism) is designed as 5:1. The rest mechanical design of the leg is the same as the single leg robot.

7.3.2 Control System Architecture

In the single leg hopping robot, each motor is equipped with an incremental encoder (AMT102-V, CUI, USA) to measure the motor angle. The encoders are used for both low-level current control (motor driver MTVESC50A, Maytech, China) and high-level reflex based control. The motor driver runs low-level field oriented control (FOC) at 20 kHz. A force-sensing resistor is mounted underneath the foot to detect if the robot is in the stance phase or flight phase. An ESP32s microcontroller reads all the sensor data and sends the data to the high-level controller. The high-level control is implemented in realtime at 1 kHz with Matlab Simulink xPC target (Matlab R2018a, Mathworks, USA). The motor drivers and the microcontrollers are interfaced with the xPC target machine through EtherCAT communication bus at 1 kHz. The overview of the control system architecture is illustrated in Fig. 2.

The bipedal robot has the same control architecture as the single leg robot. The main difference is the motor driver. In order to generate higher torques in the motors, the motor drivers in the bipedal

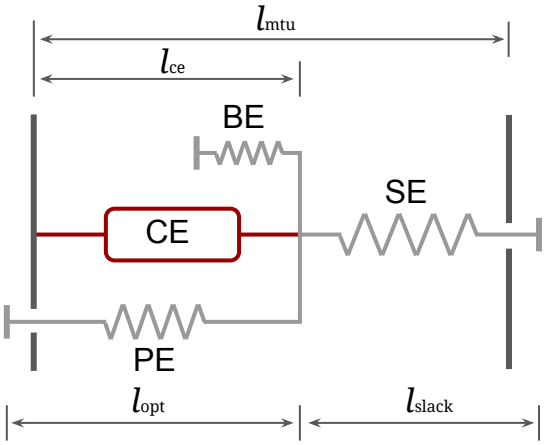

Figure 3: Muscle-tendon unit (MTU) model. CE, BE, PE and SE denote contractile element, buffer elasticity, parallel elasticity, and series elasticity, respectively.

robot (FSESC6.6, Flipsky, China) are able to deliver about twice peak current than the motor drivers in the single leg robot.

7.3.3 Simulation

We built a physical simulation model in MuJoCo (Todorov et al., 2012) based on the robot CAD design. Each part of the robot was weighted before the assembling. The moment of inertia of every part was calculated based on the measured weight by assuming the density is homogeneous. The parameters of the foot-ground contact model and the damping coefficients of all joints were tunned manually to match the results of the real robot experiment data. The MuJoCo physical simulation model runs at 10 kHz to have stable and accurate simulation. The control rate in the simulation was set to 1 kHz to match the control rate of the real robot.

7.4 Controller

7.4.1 Muscular model

The Hill-type muscle-tendon unit (MTU) model (Fig. 3, Geyer and Herr (2010)) is used in this paper. The MTU consists of a series elasticity (SE), a contractile element (CE), a parallel elasticity (PE), and a buffer elasticity (BE). The generated CE force F_{ce} is computed by the muscle activation (A), maximum isometric force F_{max}, force-length (f_l) and force-velocity (f_v) relationships of the CE (Geyer et al., 2003; Geyer and Herr, 2010):

$$F_{ce} = AF_{max} f_l(l_{ce}) f_v(v_{ce}) \tag{1}$$

$$f_l(l_{ce}) = \exp\left(c\left|\frac{l_{ce}-l_{opt}}{l_{opt}w}\right|\right) \tag{2}$$

$$f_v(v_{ce}) = \begin{cases} \frac{v_{max}-v_{ce}}{v_{max}+Kv_{ce}} & v_{ce} < 0 \\ N+(N-1)\frac{v_{max}-v_{ce}}{7.56Kv_{ce}-v_{max}} & v_{ce} \geq 0 \end{cases} \tag{3}$$

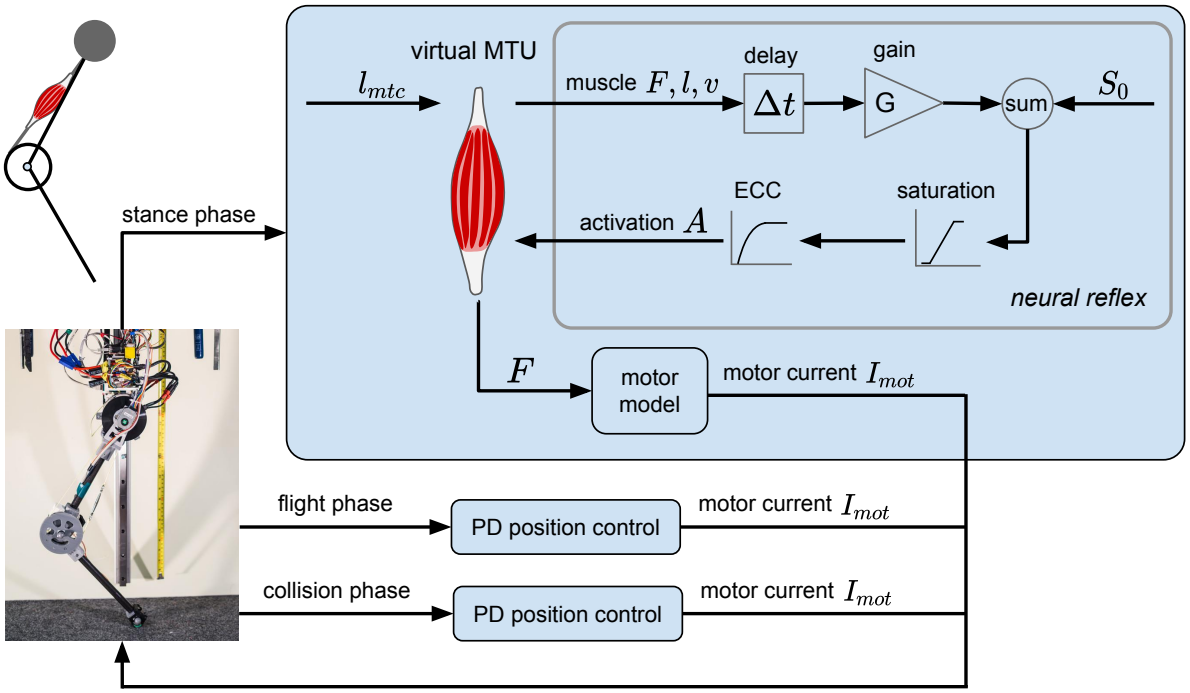

Figure 4: Schematic view of the hopping controller. The force sensor underneath the foot is used to detect if the robot is in stance, flight or collision phase.

where negative CE velocity v_{ce} denotes the concentric movement. The width w and residual force factor c define the shape of f_l. The eccentric force enhancement N and the shape factor K define the f_v. The MTU force F_m can be computed as

$$F_m = F_{se} = F_{ce} + F_{pe} - F_{be} \tag{4}$$

where

$$F_{se} = \begin{cases} F_{max}\left(\frac{l_{se}/l_{slack}-1}{\varepsilon_{ref}}\right)^2 & l_{se} > l_{slack} \\ 0 & l_{se} \leq l_{slack} \end{cases} \tag{5}$$

$$F_{pe} = F_{max}\left(\frac{l_{ce} - l_{opt}}{l_{opt}\varepsilon_{pe}}\right)^2 \tag{6}$$

$$F_{be} = F_{max}\left(\frac{l_{min} - l_{ce}}{l_{opt}\varepsilon_{be}}\right)^2 \tag{7}$$

where l_{se} is the SE length, l_{slack} is the SE rest length, ε_{ref} is the reference strain of the SE, ε_{pe} is the reference strain of the PE, l_{opt} is the optimum length, l_{min} is the BE rest length, ε_{be} is the BE reference strain All the parameter values are listed in Table 1.

Table 1: Virtual neuromuscular model paramters

Parameter	Value [unit]
F_{max}	1600 N
N	1.5
K	5
c	$\ln 0.05$
w	0.4
l_{opt}	0.1 m
l_{slack}	0.4 m
l_{min}	$l_{opt} - w$
v_{max}	$12 l_{opt}$ s^{-1}
ε_{ref}	0.08
ε_{pe}	w
ε_{be}	$w/2$
S_0	0.01
τ	0.01 s
Δt	0.005 s

7.4.2 Neural reflex

The muscle excitation-contraction coupling (ECC) is modelled as (Geyer et al., 2003):

$$\tau \frac{\mathrm{d}A(t)}{\mathrm{d}t} = S(t) - A(t) \tag{8}$$

where $S(t)$ is the stimulation signal (neural input), $A(t)$ is the muscle activation, and τ is a time constant. We assume a linear relation between S and the sensory feedback P (i.e. F_m, l_{ce}, v_{ce}):

$$S(t) = \begin{cases} S_0 & t \leq \Delta t \\ S_0 + GP(t - \Delta t) & t > \Delta t \end{cases} \tag{9}$$

where S_0 is the constant stimulation bias, G is the gain factor for different feedback signals, and Δt is the sensory feedback time delay. $S(t)$ is saturated in the range of $[0, 1]$. In the implementation, each sensory feedback P signal (i.e. F_m, l_{ce}, v_{ce}) is normalized. More specifically, $S(t)$ for each individual feedback pathway (i.e. force feedback (FFB), length feedback (LFB), and velocity feedback (VFB)) is computed as:

$$S(t) = \begin{cases} S_0 & t \leq \Delta t \\ S_0 + G_F F_m^n(t - \Delta t) & \text{FFB}, t > \Delta t \\ S_0 + G_L l_{ce}^n(t - \Delta t) & \text{LFB}, t > \Delta t \\ S_0 + G_F v_{ce}^n(t - \Delta t) & \text{VFB}, t > \Delta t \end{cases} \tag{10}$$

where $F_m^n = F_m/F_{max}$, $l_{ce}^n = l_{ce}/l_{opt}$, and $v_{ce}^n = v_{ce}/v_{max}$. G_F, G_L, and G_V denote the gain for force, length, and velocity feedback pathway, respectively. Compared to the other approaches (Geyer et al., 2003; Haeufle et al., 2012, 2010), the length and velocity offsets are not taken into account in the feedback pathways because finding the optimal control parameters for a certain motion is not the aim of this paper. Here, we aim at demonstrating the feasibility and potential benefits of the neuromuscular reflex control concept on the robotic hardware system.

7.4.3 Hopping control scheme

The hopping control are separated into flight, stance, and collision phase. The overview of the control scheme for a single leg is shown in Fig. 4. The individual leg control scheme of the bipedal robot is the same as the single leg robot.

Stance phase

In the stance phase, the hip motor is set to free (desired current set to 0 A) while the knee motor is controlled as a virtual Hill-type MTU (Fig. 3, Fig. 4). The virtual MTU length l_{mtc} is calculated as

$$l_{mtc} = r_{mtc}\, \theta_{mot}^k / c \tag{11}$$

where θ_{mot}^k, c and r_{mtc} are the robot knee motor angle measured by the encoder, the gear ratio, and the virtual MTC moment arm, respectively. c is 4, which is the ratio between knee joint pulley diameter and the knee motor pulley diameter. r_{mtc} is set to 0.04 m in this study. The muscle activation A is calculated based on the neural reflex controller. Virtual muscle states (i.e. muscle F, l, v) are computed based on the muscular model given l_{mtc}. The knee motor desired current I_{mot}^k is calculated and sent to the motor driver based on the motor model given the desired virtual MTC force.

Flight phase

The flight phase controller is to prepare the leg with an appropriate posture for the next landing. Here, a simple PD position controller with fixed target knee and hip angle is used during the flight phase. The PD values are manually tuned so that the robot can not only achieve the desired posture before next touch down (TD) but also have low effective joint compliance to avoid high impact forces at TD. In this study, the hip and knee desired joint angle during the flight phase are set to 20° and 40° respectively.

Collision phase

The collision phase is defined as a very short duration time t_c after TD. Both hip and knee motor are position controlled with relatively low P but high D value to absorb the impact energy during the collision. This prevents the shank rebounding/oscillating if the robot lands on a stiff ground. We set t_c as 20 ms because it is much shorter than the muscle reflex time (around 200 ms for hopping) while the shank rebound can still be eliminated.

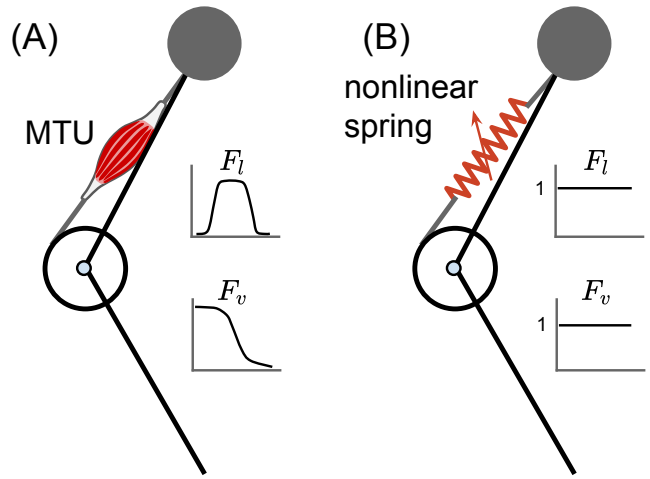

Figure 5: Schematic virtual model of the robotic leg with (A) the virtual MTU model, (B) the simplified MTU model which can be viewed as a nonlinear spring.

7.4.4 MTU vs. simplified nonlinear spring

In order to investigate the potential benefits of the MTU properties, we also built a controller based on a highly simplified MTU model (Fig. 5). Inspired by the work from Haeufle et al. (2010), here the muscle force-length and force-velocity nonlinear relationships were simplified to constant (i.e. $f_l = 1$, $f_v = 1$). And the BE, PE, and SE were removed from the model. This simplified MTU model can be viewed as a nonlinear spring model. The spring force F_s calculation is simplified from the equation (4) to

$$F_s = A_s F_{max} \tag{12}$$

A_s is the same as the muscle activation, which is the factor depending on the spring force, length or velocity. It can be computed with equation (8). The stimulation signal $S(t)$ is calculated as

$$S(t) = \begin{cases} S_0 & t \leq \Delta t \\ S_0 + G_F F_s^n(t-\Delta t) & \text{FFB}, t > \Delta t \\ S_0 + G_L l_s^n(t-\Delta t) & \text{LFB}, t > \Delta t \\ S_0 + G_F v_s^n(t-\Delta t) & \text{VFB}, t > \Delta t \end{cases} \tag{13}$$

where $F_s^n = F_s/F_{max}$, $l_s^n = l_s/l_0$, and $v_s^n = v_{ce}/v_{max}$. This simplified model can be viewed as a nonlinear spring which the stiffness is depended on the spring states (i.e. force, legnth and velocity).

7.4.5 Implementation

The hopping control scheme was implemented with Matlab Simulink (2018a) in both simulation and the real-time controller for the real robots at 1 kHz control rate. The parameters for the PD position controller during the flight phase and the collision phase were tuned by hand. The desired motor currents were saturated due to the motor driver hardware limitation. The maximum motor current was 50 A and 100 A

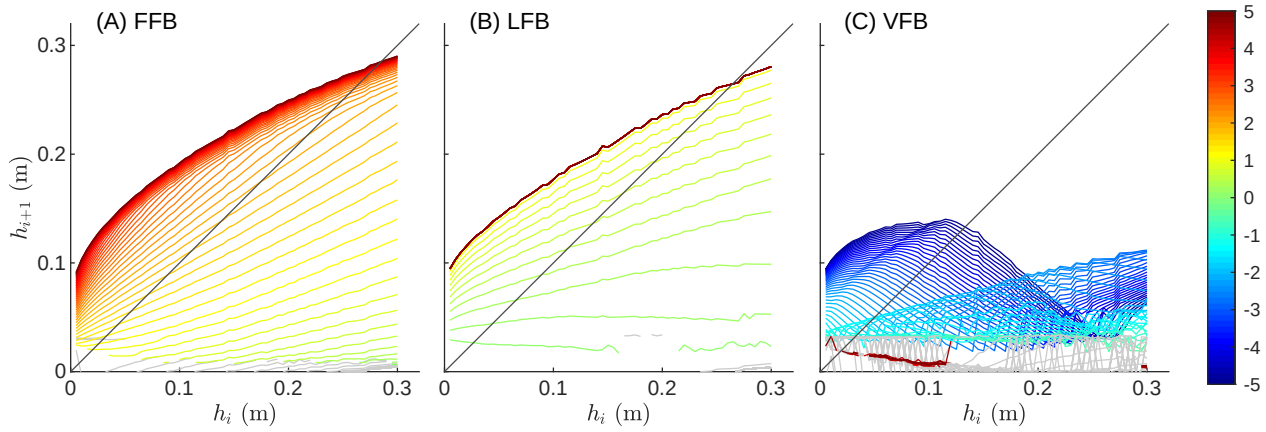

Figure 6: Simulation results of the return maps of the bipedal robot. (A) With only force feedback (FFB). (B) With only length feedback (LFB). (C) With only velocity feedback (VFB). The range of FFB, LFB and VFB gain is $[-5,5]$ with a step size of 0.1. Different gain values are denoted with different colors. The light grey color denotes the situation which the robot does not rebound. The intersections of the colored line and the dark grey diagonal line indicate fixed points (periodic motions, i.e. $h_{i+1} = h_i$). The periodic motion is stable if the slope $S = \mathrm{d}h_{i+1}/\mathrm{d}h_i$ around the fixed point satisfies the condition $|S| < 1$. h_i and h_{i+1} denote the ith and the $(i+1)$th hopping height, respectively.

for the single leg robot and the bipedal robot, respectively. A lithium polymer battery was used to delivery high enough peak current to the motor drivers. Both simulation and the real-time controller have the same parameter values because the simulation model is very close to the hardware setup.

7.5 Results

This section shows the results of the simulation study and the hardware experiments. First, in order to show if stable hopping can be achieved with the proposed bio-inspired hopping controller, the return maps of the individual muscle reflex are presented. Then the robustness of the muscle force feedback is demonstrated by the return maps of different robot model properties and ground impedance. Finally, the results of the robot hardware experiments are presented to verify the simulation model and prove the feasibility of the hardware design and implementation.

7.5.1 Return maps

In order to investigate the influence of the individual muscle feedback pathway (i.e. force, length and velocity) on the hopping motion, we computed return maps for each feedback pathway with brute force in simulation (shown in Fig. 6) by dropping the robot from 0.005 m to 0.3 m height with a step size of 0.005 m. The range of the feedback gain was chosen as $[-5,5]$. The robot can generate both stable hopping and landing (not rebound) motion with the gain in this range. Because the return maps of the single leg robot and the bipedal robot are very similar, we only present the return maps of the bipedal robot.

The results shows that both positive FFB (G_F), positive LFB (G_L) and negative VFB (G_V) can generate stable hopping. The return map of the FFB is smoother than the return map of both LFB and VFB. The VFB generate unstable and chaotic motions if the G_V is around -1.2. There is a clear saturation trend in

the maximum stable hopping height h_{max} for all three feedback pathways (when $G_F > 2.5$, $G_L > 1.0$ or $G_V < -4.5$). The FFB has the highest h_{max} (0.28 m, $G_F = 5$) compared to the LFB (0.27 m, $G_F = 5$) and the VFB (0.13 m, $G_V = -5$). In the FFB, the robot will not rebound even with the 0.3 m dropping height if the G_F is less than zero.

The FFB shows superior features (e.g. smoothness, range of stable hopping height, stability) than the LFB and VFB (Fig. 6). Therefore in the following analysis, we will only focus on the FFB.

7.5.2 Robustness of the FFB

To explore the robustness of the neuromuscular reflex based controller, we analyzed the effects of parameters of the model and the environment on the return map. For the robot parameters, we increased the robot mass from the original mass m to $1.6m$ with a step size of $0.2m$. We also investigated the influences of the rope impedance on the hopping performance. We changed the rope from the original rigid configuration (stiffness 8×10^7N/m, damping coefficient 500Ns/m) to stiff (10^6N/m, 5Ns/m), moderate (10^5N/m, 5Ns/m) and soft (10^4N/m, 5Ns/m) configurations. In this case, the rope can be considered as an elastic component in serial of the virtual MTU. For the environment parameters, we decreased the ground impedance from the original impedance (scaled as 1) to 0.4 with a step size of 0.2. Here we focus on how the FFB return map changes. Based on the original FFB return map (shown in Fig. 6(A)), the robot will not rebound if the gain is smaller than 0.5. And the robot hopping height will be saturated if the gain is larger than 2.5. Therefore, the FFB return map with the gain in $[0.5, 2.5]$ (step size 0.1) was computed for different body mass, ground impedance, and rope stiffness conditions. All the results are shown in Fig. 7.

Compared to the FFB return map in the normal condition (Fig. 7(A)), the robot maximum stable hopping height decreases with the increasing body mass or decreasing ground impedance. Compared to different ground impedance and rope stiffness conditions, the return maps in the different body mass conditions are more similar to the normal condition in terms of the stable hopping height and the shape of the map. For instance, the maximum stable hopping height only dropped 0.016 m from the normal condition to the 1.6 times body mass condition. For the different ground impedance conditions, the robot show stable hopping solutions. But the maximum stable hopping height drops a lot with decreasing ground impedance compared to the normal condition. The maximum stable hopping height for normal, 0.8 impedance, 0.6 impedance, and 0.4 impedance are 0.26 m, 0.215 m, 0.145 m, and 0.102 m, respectively. The return map in stiff rope condition is almost the same as the normal condition. It gets a bit unstable in the moderate rope stiffness condition. In the soft rope condition, there is no stable hopping solution in the hopping height from 0 to 0.3 m.

7.5.3 MTU vs. simplified nonlinear spring

In order to investigate the influence of the muscle force-length and force-velocity relationship on the robot hopping behavior, the return maps of the simplified nonlinear spring model are computed and shown in Fig. 8. Here, we focus on the results of FFB because the FFB with the MTU model shows the best performance in terms of stability, range of stable hopping. The return map in Fig. 8(A) is the same as the return map in Fig. 7(A) but with different x-axis and y-axis scale. Compared to the return maps with MTU mode, the simplified model return map shows no stable hopping solutions in hopping height range

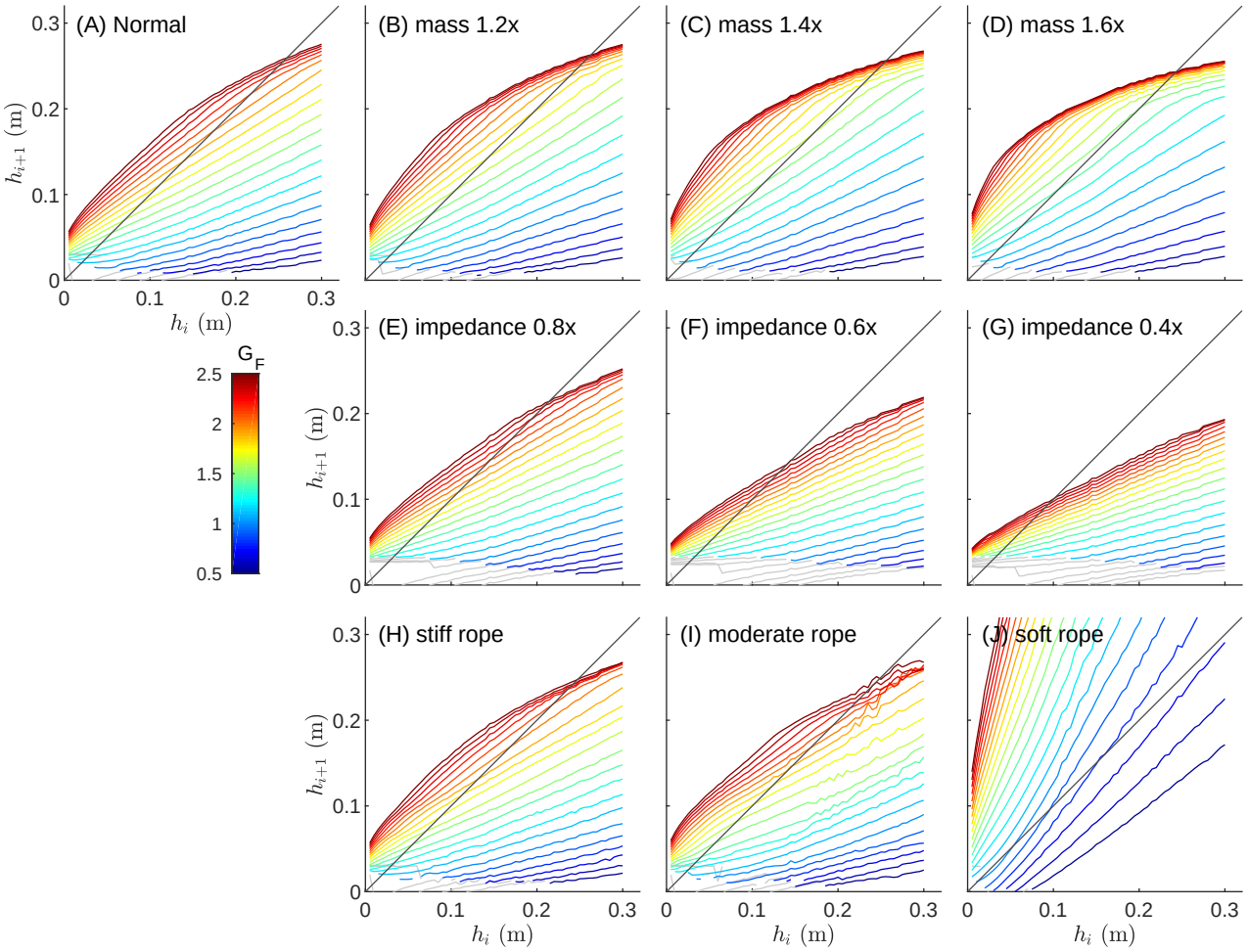

Figure 7: The bipedal robot simulation results of the return maps with only FFB in different conditions. (A) The reference condition. The scaled body mass is 1. The ground is rigid (scaled impedance is 1). And the rope is also rigid (stiffness $k_{rope} = 8 \times 10^7 \mathrm{N/m}$, damping coefficient $d_{rope} = 500 \mathrm{Ns/m}$). (B), (C) and (D) are the return maps of different body mass conditions. The scaled body masses for (B), (C) and (D) are 1.2, 1.4 and 1.6 respectively. (E), (F) and (G) are the return maps of different ground impedance. The scaled impedance are 0.8, 0.6 and 0.4 for (E), (F) and (G), respectively. (H), (I) and (J) are the return maps of different rope stiffness. The rope stiffness for (H), (I) and (J) are $10^6 \mathrm{N/m}$, $10^5 \mathrm{N/m}$, $10^4 \mathrm{N/m}$, respectively. The rope damping coefficients for all three conditions are set as $5 \mathrm{Ns/m}$. The range of FFB gain G_F is $[0.5, 2.5]$ with a step size of 0.1. Different gain values are denoted with different colors. The light grey color denotes the situation which the robot does not rebound. The intersections of the colored line and the dark grey diagonal line indicate fixed points (periodic motions, i.e. $h_{i+1} = h_i$). The periodic motion is stable if the slope $S = \mathrm{d}h_{i+1}/\mathrm{d}h_i$ around the fixed point satisfies the condition $|S| < 1$. h_i and h_{i+1} denote the ith and the $(i+1)$th hopping height, respectively.

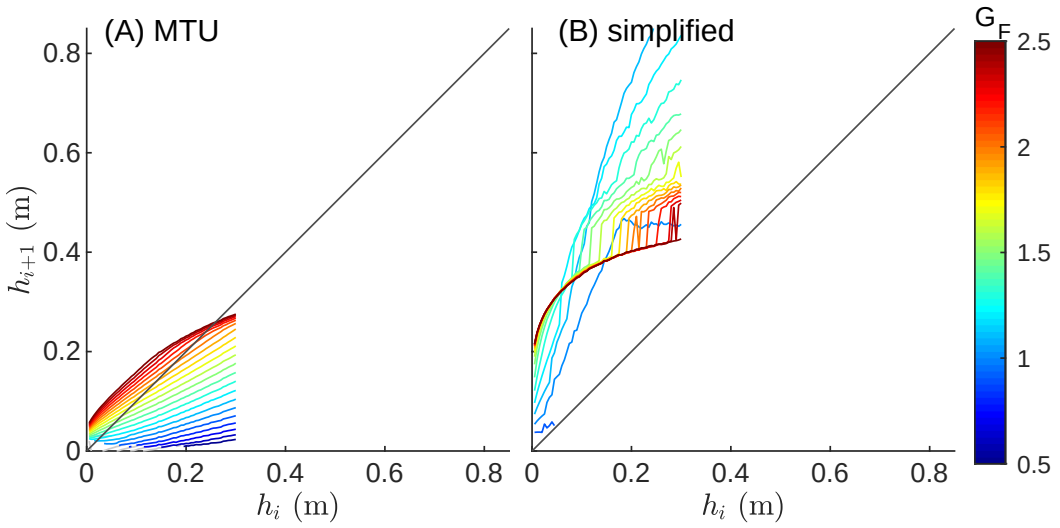

Figure 8: The simulation results of the return maps of the bipedal robot with (A) the Hill-type virtual MTU model, and (B) the simplified MTU model which can be considered as a nonlinear spring. The return maps are only with FFB. The FFB gain G_F is from 0.5 to 2.5 with a step size of 0.1. Different gain values are denoted with different colors. The light grey color denotes the situation which the robot does not rebound. The intersections of the colored line and the dark grey diagonal line indicate fixed points (periodic motions, i.e. $h_{i+1} = h_i$).

from 0 to 0.3 m. With the simplified model, the robot rebound height is higher than the MTU model if the robot is dropped with the same dropping height and the same FFB gain.

7.5.4 Robot hardware demonstration

The bio-inspired neuromuscular reflex based controller was implemented on the real robot. Both the single leg and the bipedal robot can achieve stable and robust hopping with appropriate feedback gains (Fig. 9, see the supplementary video for more details).

The real robot hopping behavior is very similar to the hopping behavior we observed from the simulation. To validate the simulation model, we compared the stable hopping height of the real robot and the simulation model with different FFB gains (shown in Fig. 10). The real robot hopping height was measured by a high-speed camera based motion capture system (Qualisys, Sweden). Ten continuous stable hopping data in each FFB gain were used to calculate the mean and the standard deviation of the real robot hopping height. The robot does not have a stable hopping pattern if the FFB gain is smaller than 1.1. This is the same as we observed in the simulation. The pelvis range of motion is limited by the linear guide length which is 0.4 m. Due to this limitation, we only did the robot hopping experiments with the FFB gain from 1.1 to 1.8 with a step size of 0.1.

The hopping height of both simulation and the real robot experiments increases with higher FFB gain. The maximum hopping height difference is 0.008 m at $G_F = 1.6$. The difference between the simulation and experimental hopping height are 0.004 ± 0.002m (mean$\pm$standard deviation). This confirms that the simulation model is valid.

The measured motor current and the electric power consumption of the single leg robot and the bipedal robot during hopping at the hopping height of 4 cm are shown in Fig. 11. The single leg knee motor current is saturated at 50 A (due to the motor driver hardware limitation) during the mid-stance

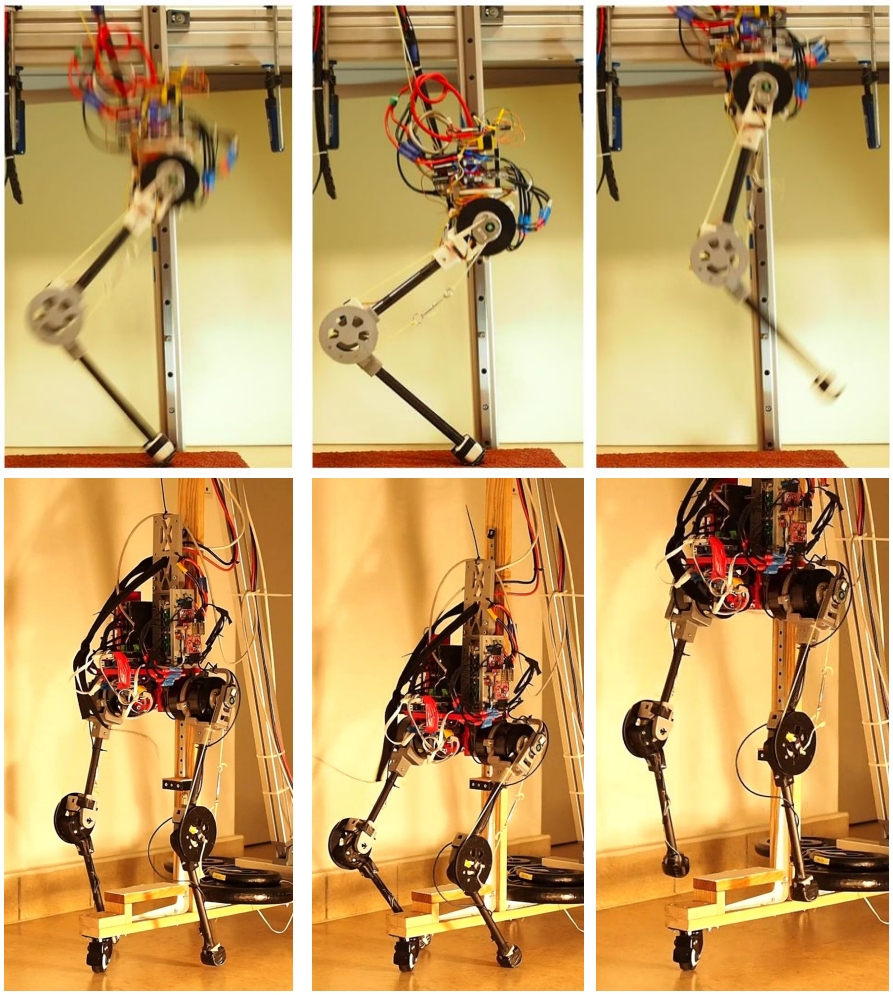

Figure 9: Snapshots of the single leg robot and the bipedal robot during hopping.

phase. We need to increase the motor driver maximum current and/or the gear ratio if we want to achieve higher hopping height. The hip motor peak current in the bipedal robot reaches around 90 A at the beginning and the end of the flight phase. This is because of relative large P value in the PD control of the hip motor. The knee motor of both the single leg robot and the bipedal robot show regenerative braking at the beginning of stance phase and the beginning of flight phase. The average electric energy consumption for each knee motor is 40 J per hop. The regenerated energy is 30% of the consumption energy in each knee motor. The hip motors do not have regenerative braking phases.

7.6 Discussion

In this paper, we presented a low-cost robotic leg design which is capable of demonstrating the bio-inspired neuromuscular reflex based hopping controller. Based on the return maps from the simulation results, we found that the stable hopping can be achieved with both positive force and length reflex while the velocity reflex could result in unstable behaviors. The force reflex based control is more stable than the length reflex based control. The robustness of the force reflex based control was investigated by varying the model parameters (body mass and rope stiffness) and the ground impedance in the simulation. By comparing the results of the Hill-type MTU model and the simplified muscle model (ignoring the force-length and force-velocity relationship), the importance of the muscle intrinsic proprieties in stabilizing

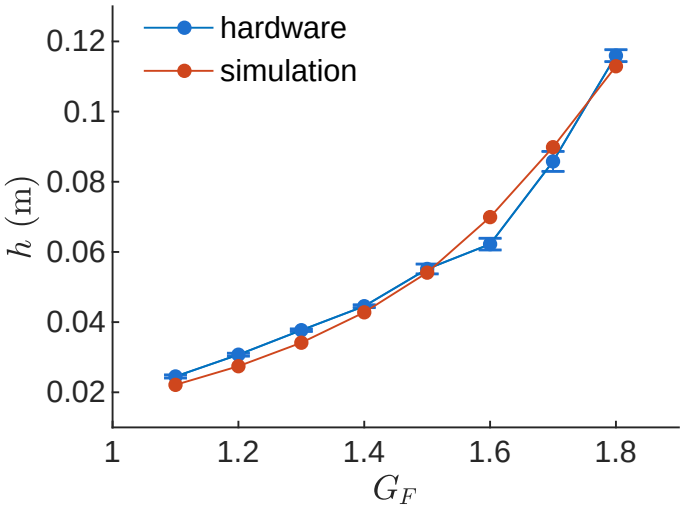

Figure 10: The bipedal robot stable hopping height (h) with different force feedback gains (G_F). The blue and red color denote mean hopping height in the robot hardware experiments and the simulations, respectively. The blue error bars denote ± 1 standard deviation of the experimental data. The means and standard deviations of the robot hopping height of each G_F were calculated with ten continuous stable hopping heights. The simulation hopping height standard deviations are not plotted because they are very small (less than 0.01 mm).

the hopping motion is demonstrated. The robot hardware experimental results show that the bio-inspired controller is feasible to implement and capable of achieving stable and robust hopping with the proposed low-cost robotic leg.

Recently, it has been more and more popular of using QDD electric motors in legged robots for dynamic locomotion (Ding and Park, 2017; Kalouche, 2017; Kau et al., 2019; Kenneally et al., 2016; Seok et al., 2015). The planetary gearbox with low gear ratio is often used in QDD actuators because the motor direct torque output is too small. Here, instead of planetary gearboxes, the rope-pulley mechanism was used in our robotic leg to achieve similar effects as the gearbox. The pulleys used in the robot were 3D printed with plastics. This reduces the mass and the cost of the robot. In addition, it also enables fast prototyping and testing with different gear ratios.

Compared to the robots which use customized high torque density motors (e.g. MIT cheetah (Seok et al., 2015) and MIT cheetah 3 (Bledt et al., 2018), the torque output of the motor used in our robot is relatively low because we are using off the shelf motors and motor drivers. For instance, the max knee torque of our bipedal robot is 40 N m while the max torque of the MIT cheetah 3 actuator is 230 N m). Therefore the robot was built with 3D printed plastic parts and carbon tubes to minimize the weight and the cost. The robot experimental results prove that the motor is capable of delivering enough torque to generate hopping motion. The robot has been tested for more than 1000 hops with different hopping heights (from 2 cm to 12 cm). No mechanical failure occurred. This demonstrates that the robot design is robust and can be used as a test platform for investigating dynamic legged locomotion. Because we used 3D printed parts and off the shelf motors and motor drivers, the total cost of one robotic leg is less than 600 Euros (excluding the battery and the PC for controlling the robot). This low-cost design makes it more accessible for research and education in legged robotics.

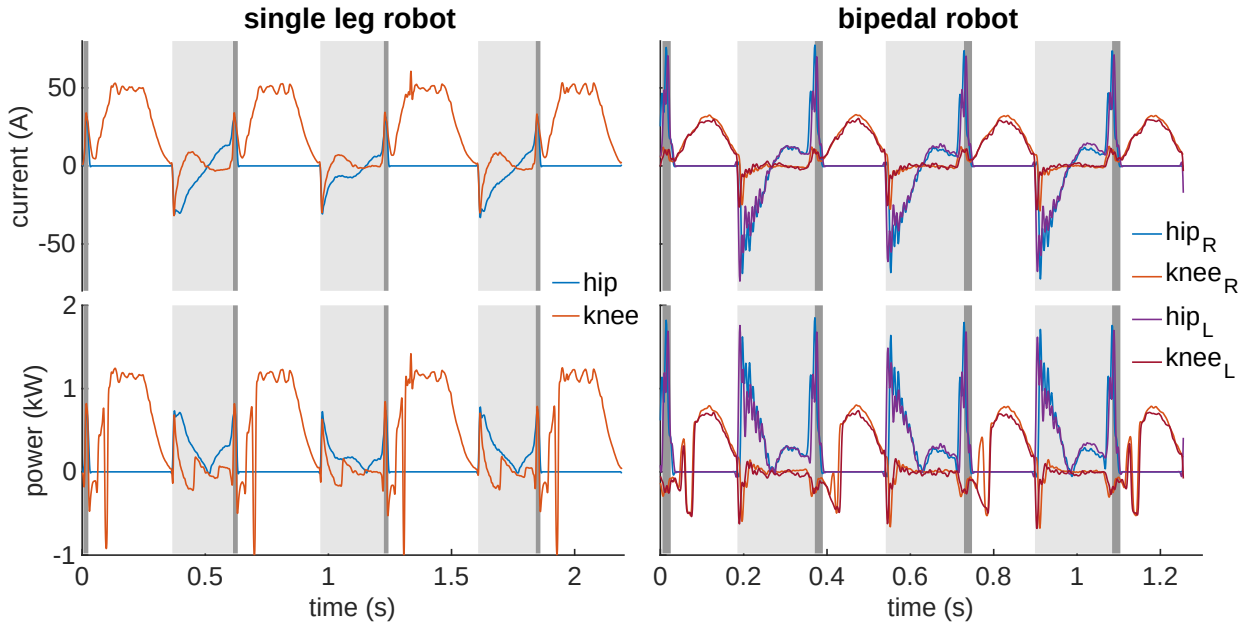

Figure 11: The measured motor current and the electric power consumption of the single leg robot and the bipedal robot during hopping at the hopping height of 4 cm. Light grey and dark grey areas denote the flight phase and the collision phase, respectively. Different colors denote different motors. For the bipedal robot, the subscripts $_R$ and $_L$ denote the right leg and the left leg, respectively. Positive current is defined as the current which results in extension torque in the robot hip or knee joint. Negative power indicates the regenerative braking (charging the battery). Both current and power data are low-pass filtered with a cutoff frequency of 100 Hz (fourth-order Butterworth filter).

Comparing to the mechanical spring or spring-damper based virtual model control (e.g. Kalouche (2017); Kalveram et al. (2012); Oehlke et al. (2016); Hubicki et al. (2016)), the proposed bio-inspired control inherits the intrinsic muscle dynamics and neuroreflex properties which can be beneficial for stabilizing the motion (Haeufle et al., 2012, 2010) and simplifying the high level control by muscle reflexes (FFB, LFB and VFB) (Schumacher and Seyfarth, 2017; Geyer and Herr, 2010; Song and Geyer, 2015). The return maps of the FFB, LFB and VFB demonstrate that both FFB and LFB can result in stable hopping motion and can be used for controlling the robot hopping height (Fig. 6). This is in line with the findings from the simplified point mass simulation models (Geyer et al., 2003; Haeufle et al., 2012; Schumacher and Seyfarth, 2017). In addition, the return map of the simplified MTU model, which assumes constant force-length and force-velocity relationship, shows no stable hopping solution (Fig. 8(B)). This is also in line with the findings from Haeufle et al. (2010). All these findings indicate that the neuromuscular reflex properties play a more important role than the leg inertia properties (a point mass model was used in Geyer et al. (2003); Schumacher and Seyfarth (2017)) and the leg geometry (a prismatic leg was used in Haeufle et al. (2012)) in shaping the hopping behavior. Further analysis on the change of the FFB return maps with different body masses and ground impedance (Fig. 7) highlights the robustness of the neuromuscular FFB based hopping controller. Therefore the proposed bio-inspired neuromuscular reflex based control approach can potentially be implemented on other legged robots to achieve bouncing gait without too much tuning of the control parameters.

Adding an elastic component in serial of the actuator can be beneficial in terms of energy efficiency and stability for dynamic legged locomotion (Sharbafi et al., 2016; Spröwitz et al., 2013). However, the results of different rope stiffness (Fig. 7) show that the additional elastic component in serial of the virtual MTU can lead to unstable hopping if the serial component is too soft. Other control approaches (e.g. combining different reflexes, modulating feedback gains during the stance phase) are required to have a stable hopping in this condition.

In this study, we focused on the neuromuscular reflex based hopping controller during the stance phase. A PD position control was used in the flight phase. This results in high current peaks in the motors at the beginning and the end of flight phase. In the future research, the robot flight phase PD control could replaced by the neuromuscular reflex control to solve this issue. And the current 1D hopping controller can potentially be transferred to 2D hopping (i.e. hopping forward and backward) by tuning the flight phase control.

Another limitation of this study is that we investigated the hopping with individual reflex pathway (i.e. force, length, and velocity). With a simplified simulation model, it has been shown that the hopping performance (e.g. hopping height, efficiency, robustness, etc.) can be improved by linear combinations of different reflexes (Schumacher and Seyfarth, 2017). In addition, combining the muscle reflex control and the feed forward stimulation could also help to generate and stabilize hopping motion (Haeufle et al., 2012). These different combinations could be investigated in the future.

7.7 Appendix

The detailed physical parameters of the single leg and the bipedal robot are shown in the table 2 and table 3, respectively.

Author contributions

Guoping Zhao is the main and corresponding author of this paper. Guoping Zhao developed the robotic leg, implemented the neuromuscular reflex based controller. Guoping Zhao and Florian Szymanski contributed the simulation and hardware robot experiments. Florian Szymanski built the bipedal robot and processed the hardware experimental data. Guoping Zhao interpreted the results and drafted the manuscript. Andre Seyfarth contributed to conceptualizing of the work. All authors revised the manuscript.

References

Bledt, G., Powell, M. J., Katz, B., Di Carlo, J., Wensing, P. M., and Kim, S. (2018). Mit cheetah 3: Design and control of a robust, dynamic quadruped robot. In *2018 IEEE/RSJ International Conference on Intelligent Robots and Systems (IROS)*, pages 2245–2252.

Blickhan, R. (1989). The spring-mass model for running and hopping. *Journal of Biomechanics*, 22(11–12):1217 – 1227.

Ding, Y. and Park, H. (2017). Design and experimental implementation of a quasi-direct-drive leg for optimized jumping. In *2017 IEEE/RSJ International Conference on Intelligent Robots and Systems (IROS)*, pages 300–305.

Table 2: Robot physical parameters

Parameter	Value [unit]
Total mass	2.8 kg
Hip mass	1.24 kg
Thigh mass	1.38 kg
Shank mass	0.18 kg
Thigh length	0.27 m
Shank length	0.27 m
Thigh moment of inertia w.r.t hip joint axis	8.7×10^{-3} kg m^3
Shank moment of inertia w.r.t knee joint axis	1.8×10^{-3} kg m^3
Motor rotor moment of inertia w.r.t motor axis	0.5×10^{-3} kg m^3
Knee motor pulley diameter	0.02 m
Knee joint pulley diameter	0.08 m
Hip joint range of motion	$[-70°, 70°]$
Knee joint range of motion	$[5°, 70°]$
Motor max torque τ_{max}	4 N m
Motor max speed ω_{max}	2600 rpm
Motor torque constant k_τ	0.08 Nm/A
Linear guide rail damping coefficient d_{rail}	0.027 Ns/m
Rope stiffness k_{rope}	8×10^7 N/m
Rope damping coefficient d_{rope}	500 Ns/m

Eilenberg, M. F., Geyer, H., and Herr, H. (2010). Control of a powered ankle–foot prosthesis based on a neuromuscular model. *IEEE Transactions on Neural Systems and Rehabilitation Engineering*, 18(2):164–173.

Full, R. and Koditschek, D. (1999). Templates and anchors: neuromechanical hypotheses of legged locomotion on land. *Journal of Experimental Biology*, 202(23):3325–3332.

Geyer, H. and Herr, H. (2010). A muscle-reflex model that encodes principles of legged mechanics produces human walking dynamics and muscle activities. *IEEE Transactions on neural systems and rehabilitation engineering*, 18(3):263–273.

Geyer, H., Seyfarth, A., and Blickhan, R. (2003). Positive force feedback in bouncing gaits? *Proceedings of the Royal Society of London B: Biological Sciences*, 270(1529):2173–2183.

Geyer, H., Seyfarth, A., and Blickhan, R. (2006). Compliant leg behaviour explains basic dynamics of walking and running. *Proceedings of the Royal Society of London B: Biological Sciences*, 273(1603):2861–2867.

Haeufle, D. F. B., Grimmer, S., Kalveram, K.-T., and Seyfarth, A. (2012). Integration of intrinsic muscle properties, feed-forward and feedback signals for generating and stabilizing hopping. *Journal of The Royal Society Interface*, 9(72):1458–1469.

Haeufle, D. F. B., Grimmer, S., and Seyfarth, A. (2010). The role of intrinsic muscle properties for stable hopping stability is achieved by the force velocity relation. *Bioinspiration & Biomimetics*, 5(1):016004.

Table 3: Robot physical parameters

Parameter	Value [unit]
Total mass	6.2 kg
Trunk mass	3.3 kg
Knee Rotor mass	0.26 kg
Thigh mass	1.0 kg
Shank mass	0.19 kg
Thigh length	0.27 m
Shank length	0.28 m
Thigh moment of inertia w.r.t hip joint axis	7.1×10^{-3} kg m^3
Shank moment of inertia w.r.t knee joint axis	1.7×10^{-3} kg m^3
Motor rotor moment of inertia w.r.t motor axis	0.35×10^{-3} kg m^3
Knee motor pulley diameter	0.02 m
Knee joint pulley diameter	0.1 m
Hip joint range of motion	$[-70°, 70°]$
Knee joint range of motion	$[0°, -120°]$
Motor max torque τ_{max}	8 N m
Motor max speed ω_{max}	2600 rpm
Motor torque constant k_τ	0.08 Nm/A
Linear guide rail damping coefficient d_{rail}	0.027 Ns/m
Rope stiffness k_{rope}	8×10^7 N/m
Rope damping coefficient d_{rope}	500 Ns/m

Heim, S., Ruppert, F., Sarvestani, A. A., and Spröwitz, A. (2018). Shaping in practice: Training wheels to learn fast hopping directly in hardware. In *2018 IEEE International Conference on Robotics and Automation (ICRA)*, pages 1–6.

Hubicki, C., Grimes, J., Jones, M., Renjewski, D., Spröwitz, A., Abate, A., and Hurst, J. (2016). Atrias: Design and validation of a tether-free 3d-capable spring-mass bipedal robot. *The International Journal of Robotics Research*, 35(12):1497–1521.

Kalouche, S. (2017). Goat: A legged robot with 3d agility and virtual compliance. In *2017 IEEE/RSJ International Conference on Intelligent Robots and Systems (IROS)*, pages 4110–4117.

Kalveram, K. T., Haeufle, D. F. B., Seyfarth, A., and Grimmer, S. (2012). Energy management that generates terrain following versus apex-preserving hopping in man and machine. *Biological Cybernetics*, 106(1):1–13.

Kau, N., Schultz, A., Ferrante, N., and Slade, P. (2019). Stanford doggo: An open-source, quasi-direct-drive quadruped. *arXiv preprint arXiv:1905.04254*.

Kenneally, G., De, A., and Koditschek, D. E. (2016). Design principles for a family of direct-drive legged robots. *IEEE Robotics and Automation Letters*, 1(2):900–907.

Liu, X., Rosendo, A., Ikemoto, S., Shimizu, M., and Hosoda, K. (2018). Robotic investigation on effect of stretch reflex and crossed inhibitory response on bipedal hopping. *Journal of The Royal Society Interface*, 15(140):20180024.

Ludwig, C., Grimmer, S., Seyfarth, A., and Maus, H.-M. (2012). Multiple-step model-experiment matching allows precise definition of dynamical leg parameters in human running. *Journal of Biomechanics*, 45(14):2472 – 2475.

Niiyama, R., Nagakubo, A., and Kuniyoshi, Y. (2007). Mowgli: A bipedal jumping and landing robot with an artificial musculoskeletal system. In *Proceedings 2007 IEEE International Conference on Robotics and Automation*, pages 2546–2551.

Oehlke, J., Sharbafi, M. A., Beckerle, P., and Seyfarth, A. (2016). Template-based hopping control of a bio-inspired segmented robotic leg. In *2016 6th IEEE International Conference on Biomedical Robotics and Biomechatronics (BioRob)*, pages 35–40.

Pratt, J., Chew, C.-M., Torres, A., Dilworth, P., and Pratt, G. (2001). Virtual model control: An intuitive approach for bipedal locomotion. *The International Journal of Robotics Research*, 20(2):129–143.

Raibert, M. H. (1986). *Legged robots that balance*. MIT press.

Riese, S. and Seyfarth, A. (2011). Stance leg control: variation of leg parameters supports stable hopping. *Bioinspiration & Biomimetics*, 7(1):016006.

Ruiz Garate, V., Parri, A., Yan, T., Munih, M., Molino Lova, R., Vitiello, N., and Ronsse, R. (2016). Walking assistance using artificial primitives: A novel bioinspired framework using motor primitives for locomotion assistance through a wearable cooperative exoskeleton. *IEEE Robotics Automation Magazine*, 23(1):83–95.

Schumacher, C. and Seyfarth, A. (2017). Sensor-motor maps for describing linear reflex composition in hopping. *Frontiers in Computational Neuroscience*, 11:108.

Seok, S., Wang, A., Chuah, M. Y., Hyun, D. J., Lee, J., Otten, D. M., Lang, J. H., and Kim, S. (2015). Design principles for energy-efficient legged locomotion and implementation on the mit cheetah robot. *IEEE/ASME Transactions on Mechatronics*, 20(3):1117–1129.

Seyfarth, A., Grimmer, S., et al. (2013). Biomechanical and neuromechanical concepts for legged locomotion: Computer models and robot validation: Andre seyfarth, sten grimmer, daniel häufle, horst-moritz maus, frank peuker and karl-theodor kalveram. In *Routledge Handbook of Motor Control and Motor Learning*, pages 99–119. Routledge.

Sharbafi, M. A., Rode, C., Kurowski, S., Scholz, D., Möckel, R., Radkhah, K., Zhao, G., Rashty, A. M., von Stryk, O., and Seyfarth, A. (2016). A new biarticular actuator design facilitates control of leg function in BioBiped3. *Bioinspiration & Biomimetics*, 11(4):046003.

Song, S. and Geyer, H. (2015). A neural circuitry that emphasizes spinal feedback generates diverse behaviours of human locomotion. *The Journal of physiology*, 593(16):3493–3511.

Spröwitz, A., Tuleu, A., Vespignani, M., Ajallooeian, M., Badri, E., and Ijspeert, A. J. (2013). Towards dynamic trot gait locomotion: Design, control, and experiments with cheetah-cub, a compliant quadruped robot. *The International Journal of Robotics Research*, 32(8):932–950.

Thatte, N. and Geyer, H. (2016). Toward balance recovery with leg prostheses using neuromuscular model control. *IEEE Transactions on Biomedical Engineering*, 63(5):904–913.

Todorov, E., Erez, T., and Tassa, Y. (2012). Mujoco: A physics engine for model-based control. In *2012 IEEE/RSJ International Conference on Intelligent Robots and Systems*, pages 5026–5033.

Wu, A. R., Dzeladini, F., Brug, T. J. H., Tamburella, F., Tagliamonte, N. L., van Asseldonk, E. H. F., van der Kooij, H., and Ijspeert, A. J. (2017). An adaptive neuromuscular controller for assistive lower-limb exoskeletons: A preliminary study on subjects with spinal cord injury. *Frontiers in Neurorobotics*, 11:30.

Zhu, Q., Mao, Y., Xiong, R., and Wu, J. (2016). Adaptive torque and position control for a legged robot based on a series elastic actuator. *International Journal of Advanced Robotic Systems*, 13(1):26.

8 Article VI: A deep reinforcement learning based approach towards generating human walking behavior with a neuromuscular model

Authors:

Akhil S Anand, Guoping Zhao, Hubert Roth and Andre Seyfarth

Lauflabor Locomotion Laboratory, TU Darmstadt, Darmstadt, Germany
Department of Control Engineering, Universität Siegen, Siegen, Germany

Submitted for publication in 2019

8.1 Abstract

A gait model capable of generating human-like walking behavior at both the kinematic and the muscular level can be a very useful framework for developing control schemes for humanoids and wearable robots such as exoskeletons and prostheses. In this work we demonstrated the feasibility of using deep reinforcement learning based approach for neuromuscular gait modelling. A lower limb gait model consists of seven segments, fourteen degrees of freedom, and twenty two Hill-type muscles was built to capture human leg dynamics and the characteristics of muscle properties. We implemented the proximal policy optimization algorithm to learn the sensory-motor mappings (control policy) and generate human-like walking behavior for the model. Human motion capture data, muscle activation patterns and metabolic cost estimation were included in the reward function for training. The results show that the model can closely reproduce the human kinematics and ground reaction forces during walking. It is capable of generating human walking behavior in a speed range from 0.6 m/s to 1.2 m/s. It is also able to withstand unexpected hip torque perturbations during walking. We further explored the advantages of using the neuromuscular based model over the ideal joint torque based model. We observed that the neuromuscular model is more sample efficient compared to the torque model.

8.2 Introduction

The gait model capable of reproducing human-like locomotion can help us further understand the human locomotion control scheme which can be used for developing bipedal robots and wearable robots (e.g. exoskeletons, prostheses, etc.). For instance, with a simple inverted pendulum model, it has been shown that the human-like bipedal walking gait can be achieved passively (without active control) because of the natural dynamics of the human body (McGeer, 1990). It has also been found that both human walking and running gait can be described by a simple spring loaded inverted pendulum model (Blickhan, 1989; Geyer et al., 2006). Several legged robots were developed and successfully demonstrated the control benefits of these models (Collins et al., 2005; Hubicki et al., 2016; McGeer, 1990). Besides, the bio-inspired conceptual model also shows benefits for the exoskeleton control (Zhao et al., 2017). However, although these simplified template models can generate human-like gait (in terms of e.g. the centre of mass movement, step length/frequency, etc.), their capability of reproducing human-like rich locomotion behaviors (e.g. stair/slope climbing, acceleration/deceleration, etc.) is very limited.

Recently, Song and Geyer (Song and Geyer, 2015) demonstrated that the diverse behaviours of human locomotion can be generated with a complex neuromuscular gait model using a neural circuitry which emphasizes the muscle reflexes. They also demonstrated that the model can produce human-like immediate changes in the muscle activation of some muscle groups (Song and Geyer, 2017). However, the architecture of the neural circuitry used in the model was hand-crafted. The model performance could be further improved if we explore the circuitry (connections of reflex pathways) with a systematic approach.

Peng et al. (2018, 2017) showed that deep reinforcement learning (deep-RL) is very useful approach in developing robust controllers for complex locomotive systems. They also demonstrated the capability of deep-RL in learning a broad range of challenging locomotion skills using kinematic data. Another closely matching work from Peng et al (Peng and van de Panne, 2017), demonstrated learning 2D muscle actuated bipedal locomotion using deep-RL. They identified that the local feedback provided by high-

level action parameterizations can significantly impact the learning, robustness, and motion quality of the resulting policies.

RL had its major successes in the discrete domain problems such as computer games (Chang et al., 2016), but human locomotion needs to be solved as a continuous control problem. RL is of advantage in solving continuous domain problems ever since the latest developments in policy gradient based methods (Lillicrap et al., 2015; Mnih et al., 2016; Schulman et al., 2015, 2017). Policy gradients were a breakthrough in the continuous domain, but still limited by many factors such as the learning rate, sample efficiency etc. Many approaches tried to eliminate these flaws which resulted in the development of algorithms such as TRPO (Schulman et al., 2015), ACER (Wang et al., 2016), PPO (Schulman et al., 2017) etc. All these methods have their own trade-offs, ACER is by far more complicated than PPO, requiring the addition of code for off-policy corrections and a replay buffer with very marginal advantage in the results tested on Atari benchmark by Open-AI (Dhariwal et al., 2017). Considering the above mentioned trade-offs, we decided to use the "Proximal Policy Optimization (PPO)" (Schulman et al., 2017) algorithm to address our problem regarding human locomotion.

The aim of this paper is to investigate the feasibility of using deep-RL for generating human walking with a neuromuscular gait model. Here, we present a deep-RL based approach towards the development of a human gait model capable of producing individual-specific 3D walking gait at the kinematic, the kinetic and the muscular levels. Although the major focus of our work is on developing deep-RL based human walking gait, we also explore the advantage of learning a muscle-based control over torque-based control in terms of sample efficiency.

The approach followed in this paper is, (i) conducting human experiments to collect the individual kinematic and kinetic data and providing a dataset for deep-RL, (ii) setting up a musculoskeletal gait model to perform deep-RL, (iii) conducting deep-RL to generate human-like kinematics and to optimize energetics, (iv) testing model against robustness, and (v) comparing the sample efficiency of muscle-based and torque-based control.

8.3 Methods

8.3.1 Human experiments

Human treadmill walking experiments were conducted with one subject (male, 27 years, height 1.75 m, weight 66 kg) to acquire the data of lower-limb joint kinematics and ground reaction forces (GRFs) in a walking speed range from 0.6 m/s to 1.2 m/s. The subject provided their informed consent for the experiment. The study design and protocol were approved by the ethical committee of TU Darmstadt. The experimental data have been pre-processed to prepare the dataset for reinforcement learning normalized to one walking step (half gait cycle). In total, the dataset contains 1200 walking steps. One step in the dataset contains all the individual lower body joint kinematics from one foot touch-down to the contra-lateral foot touch-down.

8.3.2 Modelling

The musculoskeletal model used in this study is a lower limb human model with seven segments and twenty two muscles. The model was adopted from Song and Geyer (2015) and implemented in MuJoCo

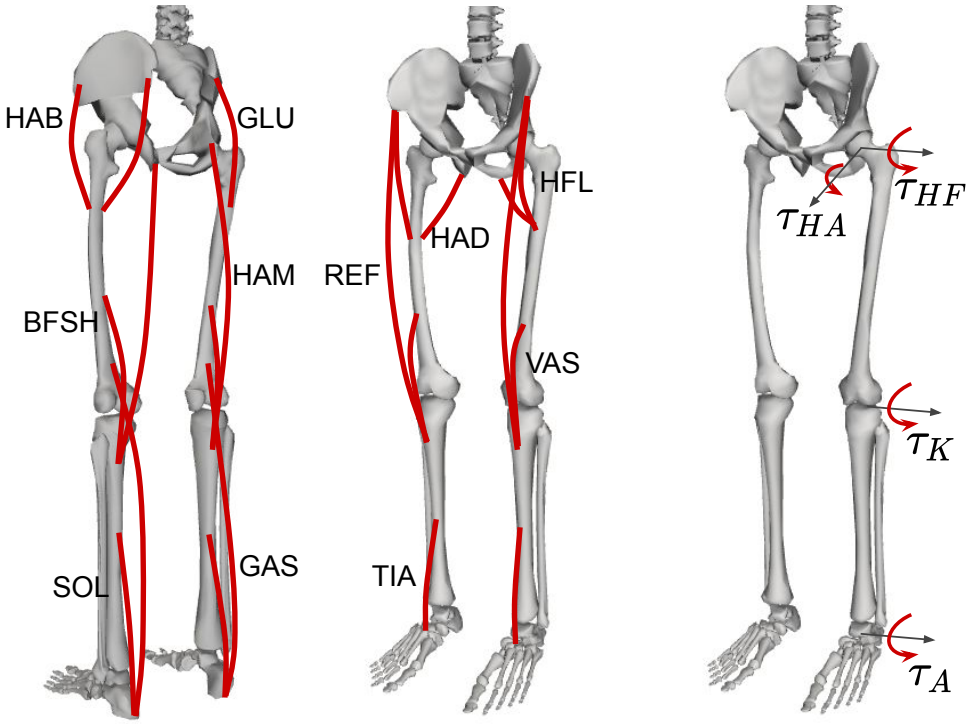

(a) neuromusculoskeletal gait model (b) torque gait model

Figure 1: Schematics of the musculoskeletal model and the torque model. (a) Lower-limb musculoskeletal model with eleven muscle groups per leg. The muscle groups are hip abductors (HAB), hip adductors (HAD), hip flexors (HFL), glutei (GLU), hamstrings (HAM), rectus femoris (REF), vastii (VAS), biceps femoris short head (BFSH), gastrocnemius (GAS), soleus (SOL), and tibialis (TIA). The HAM, REF and GAS are biarticular muscles. The HAB, HAD, HFL, GLU, VAS, BFSH and TIA are monoarticular muscles. (b) Lower-limb torque controlled bipedal model with 8 torque actuators. There are 4 joint torque actuators for each leg which are (i) hip flexion/extension τ_{HF}, (ii) hip adduction/abductionτ_{HA}, (iii) knee flexion/extension τ_K and (iv) ankle dorsiflexion/plantar flexion τ_A. The torque values could be both positive and negative.

(Todorov et al., 2012) to achieve high simulation speed. Then the model was integrated with Open-AI Gym to facilitate easy implementation of deep-RL. The model is 1.8 m tall, has a weight of 66 kg and fourteen degrees of freedom (six global DOFs for the trunk and eight internal joint DOFs). The model is 5 cm taller than the subject, but we believe the effect of such a small height difference on the joint kinematics is negligible. The physical properties, muscle-tendon-units (MTU) and the muscle properties are similar to the model from Song and Geyer (2015) except for the foot. The foot is modelled as a cuboid (width 10 cm, length 25 cm and height 6 cm) with four ground contact points. The eleven muscle groups of each leg are shown in Fig. 1(a). The torque controlled model also posses same weight, segment dimensions and degrees of freedoms. The model is actuated with eight ideal torque actuators (four for each leg) as depicted in Fig. 1(b).

8.3.3 Deep-RL implementation

In the final implementation with PPO algorithm, separate network architectures and hyper-parameters are chosen for both muscle-based and torque-based model as they differ in the state-action space dimension and characteristics. The input state space for the torque model contains the joint positions θ, joint

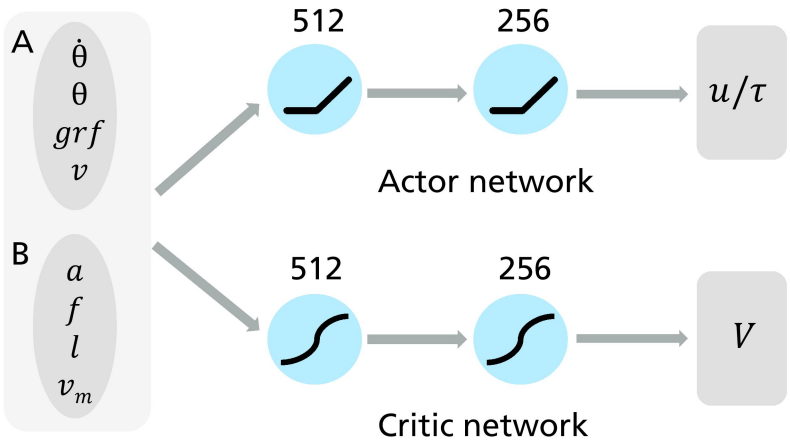

Figure 2: The network consists of two fully connected hidden layers of size 512 and 256 respectively. The actor (policy) and the critic have the same network structure. The activation function for actor and critic networks are ReLU and tanh respectively for both muscle and torque models. The input set A is the input for torque model and A,B together is the input for the muscle model. u and τ denotes the muscle activations and joint torques for muscle and torque models respectively. V denotes the state value from the critic

Table 1: Hyperparameters used for muscle and torque models

Hyperparameter	Muscle model	Torque model
No. of actors N	40	40
Samples per actor/episode n	128	128
No. of minibatches	32	32
No. of epochs	7	7
Clip factor β	0.2	0.2
GAE Parameter λ	0.95	0.95
Discount factor γ	0.99	0.99
Value function coefficient c_1	0.5	0.5
Entropy coefficient c_2	0 – 0.005	0 – 0.005
Learning rate lr	3e-5 – 1e-7	5e-4 – 1e-6

angular velocities $\dot{\theta}$, GRFs grf and target walking velocity v. The muscle-based model has additional input state, which are muscle force f, muscle length l, muscle velocity v_m and muscle activations a. The input to the muscle model is the muscle stimulation u. In the case of the torque model the inputs are the joint torques τ to the 8 joints.

Both the policy and value function architecture are defined using neural networks shown in Fig. 2. All the hyperparameters for the learning process are shown in the Table 1. The algorithm is implemented with 40 threads (workers), collecting data by acting on the environment and training the neural network on a single GPU. The pseudo-code of the implementation is shown in Algorithm 1. The input state vector and the scalar reward values are normalized using its running mean. And the standard deviation of the states are clipped to the range [-10, 10].

In Algorithm 1, θ and ϕ are the policy and value function (baseline) parameters. N is the total number of time-steps, I and J are the number of sub-iterations with policy and baseline (value function

Algorithm 1 Pseudo-code for PPO implementation

$\theta \leftarrow$ random weights
$\phi \leftarrow$ random weights
for $n \in \{1,\ldots,N\}$ **do**
  $\pi_{\mathrm{w}} \leftarrow \pi_\theta$
  Run W workers in parallel
  $\pi_{\mathrm{old}} \leftarrow \pi_\theta$
  for $i \in \{1,\ldots,I\}$ **do**
    $J_{PPO}(\theta) = \sum_{t=1}^{T} \frac{\pi_\theta(a_t|s_t)}{\pi_{old}(a_t|s_t)} \hat{A}_t - \lambda KL[\pi_{old}|\pi_\theta]$
    Update θ by stochastic gradient method w.r.t.
    $J_{PPO}(\theta)$
  end for
  for $j \in \{1,\ldots,J\}$ **do**
    $L_V(\phi) = -\sum_{t=1}^{T} \left(\sum_{t'>t} \gamma^{t'-t} r_{t'} - V_\phi(s_t)\right)^2$
    Update ϕ by a gradient method w.r.t. $L_V(\phi)$
  end for
  if $\mathrm{KL}[\pi_{old}|\pi_\theta] > \beta_{high}\mathrm{KL}_{target}$ **then**
    $\lambda \leftarrow \alpha\lambda$
  else if $\mathrm{KL}[\pi_{old}|\pi_\theta] < \beta_{low}\mathrm{KL}_{target}$ **then**
    $\lambda \leftarrow \lambda/\alpha$
  end if
end for

Worker:
for $t \in \{1,\ldots,T\}$ **do**
  Run policy π_θ , collecting $\{s_t, a_t, r_t\}$
  Estimate return $R_t = \sum_{t'=t} \gamma^{t'-t} r(s_{t'}, a_{t'})$
  Estimate advantages $\hat{A}_t = \hat{R}_t - V_\phi(s_t)$
  Store the trajectory information
end for

here) updates over a batch of data points. T denotes the number of data points collected per worker. λ and α are the KL regularization coefficient and the scaling term, respectively.

8.3.4 Muscle dynamics and perturbation protocols

In order to generate human-like muscle activation patterns, the model is trained with the guidance of the human experimental data from Perry et al. (2010). The guidance is implemented by clipping the stimulations at appropriate phases in the gait cycle. For example, in the second half of stance phase HAD and HAM muscles are completely inactive. This evidence is implemented by clipping the HAD and HAM activations to 0 during this phase. All the sensory feedback signals (kinematics, muscle dynamics and ground reaction forces) and the input stimulation signals for the muscle model are delayed by 15 ms to mimic the human sensory feedback delay (Song and Geyer, 2015).

The model is trained with joint torque perturbations on hip flexion/extension movements. In the training phase, random joint torque perturbations are applied on the model continuously for 50 ms (starting at a randomly chosen time step in the gait cycle) with a magnitude in the range from -5 N m to 5 N m. Maximum of only one perturbation is applied per gait cycle in any one of the hip joints. The probability

of applying perturbation in any gait cycle is 50%. For testing the robustness, much larger joint torque perturbations in the range of [-200, 200] Nm are applied on the hip continuously for for 50 ms. The joint torque perturbations are chosen to emulate the situation of using exosuits for assisting/perturbing walking.

Random State Initialisation (RSI) and Early Termination (ET) are very useful methods for reinforcement learning (Peng et al., 2018). We divided each trajectory in the training dataset into 10 equal time intervals. RSI is implemented by randomly selecting trajectories during training from the reference kinematic dataset and defining the initial condition by randomly choosing from 10 equal intervals of the trajectory. The idea of ET is implemented by terminating the episode if the kinematic error exceeds a given limit. More specifically, the ET is terminated if the pelvis vertical position is lower than 0.8 m or higher than 1.4 m, which corresponds to the undesired falling and jumping motion respectively.

8.3.5 Reward shaping

The reward function for the muscle and torque model contain terms which encourage imitating the kinematic trajectory, continuous stable walking, attaining a target velocity. An additional metabolic cost reward term is included for the muscle model, but the torque model is learned without using any torque minimization term.

$$r = w_l r_l + w_k r_k + w_m r_m + w_v r_v \tag{1}$$

where r is the reward, r_l is the life bonus, r_k is the kinematic behavior bonus, r_m is the metabolic bonus and r_v is the target velocity bonus. w_l=1, w_k=4, w_m=4, w_v=1 are the weights of r_l, r_k, r_m and r_v, respectively. All these individual bonus is between 0 and 1. The total reward, r is in the range from 0 to 10. The life bonous r_l denotes the reward for walking without falling. The falling condition occur when the pelvis vertical position is out of the range [0.8, 1.4] m. The r_k term defines the reward for imitating the desired trajectory. Individual position and velocity errors between the model and the experimental data are calculated for each sampling step. These errors are:

- Foot position vector error e_{fp} which denotes the squared difference between the foot position vector of the model and the reference human trajectory data.

$$e_{fp} = [c(s_{fp}(t) - \bar{s}_{fp}(t))]^2 \tag{2}$$

  Here, $s_{fp}(t)$ and $\bar{s}_{fp}(t)$ are the foot position vector of the model and the reference data respectively at time t and the scaling coefficient, c=30.

- Pelvis COM position error e_{pp} which denotes the squared difference between the pelvis COM position vector of the model and the reference data.

$$e_{pp} = [c(s_{pp}(t) - \bar{s}_{pp}(t))]^2 \tag{3}$$

  Here, $s_{pp}(t)$ and $\bar{s}_{pp}(t)$ are the pelvis COM position vector of the model and the reference data respectively at time t and c=20.

- Pelvis COM velocity error e_{pv} which denotes the squared difference between the pelvis COM velocity vector of the model and the reference data.

$$e_{pv} = c[s_{pv}(t) - \bar{s}_{pv}(t)]^2 \tag{4}$$

  Here, $s_{pv}(t)$ and $\bar{s}_{pv}(t)$ are the pelvis COM velocity vector of the model and the reference data respectively at time t and c=2.

- Joint angular position error e_{ap} which denotes the squared difference between all the joint angles of the model and the reference data.

$$e_{ap} = [c(\theta_{ap}(t) - \bar{\theta}_{ap}(t))]^2 \tag{5}$$

  Here, $\theta_{ap}(t)$ and $\bar{\theta}_{ap}(t)$ are the array of all the joint angles of the model and the reference data respectively at time t and c=12.

- Joint angular velocity error e_{av} which denotes the squared difference between all the joint angular velocities of the model and the reference data.

$$e_{av} = [c(\theta_{av}(t) - \bar{\theta}_{av}(t))]^2 \tag{6}$$

  Here, $\theta_{av}(t)$ and $\bar{\theta}_{av}(t)$ are the array of all the joint angular velocities of the model and the reference data respectively at time t and c=0.1.

All these individual errors are concatenated to form a single error vector, E as follows:

$$E = [e_{fp}, e_{pp}, e_{pv}, e_{ap}, e_{av}] \tag{7}$$

E is converted to its negative exponential and the resulting terms are summed up to get a scalar value T:

$$T = \text{sum}\left[\text{e}^{-E}\right] \tag{8}$$

The r_k term denotes how large is the T value compared to the limiting value of 28. It is computed as follows

$$r_k = \frac{T - T_{\text{limit}}}{T_{max} - T_{limit}} \quad \text{where } T_{limit} = 28\ ,\ T_{\text{max}} = 35 \tag{9}$$

The value of r_k is between 0 to 1, where 1 denotes an exact imitation of the joint trajectory and 0 corresponds a maximum allowed deviation defined by T_{limit}. The T_{limit} is also used as the ES criterion. In other words, the ES will be triggered if $T < T_{limit}$.

The metabolic rate p for the musculoskeletal model is estimated based on the muscle states according to Alexander's work (Alexander, 1997). The metabolic energy over a sampling step is converted to a value

between 0 to 1 by taking the negative exponential with a coefficient of 1/30. The value of 1/30 is chosen by monitoring the range of p during training. The calculation of r_m as follows:

$$r_m = e^{-p/30} \tag{10}$$

The r_v term is a function of the difference between the running mean of the experimental walking speed $\bar{v}_p$ and the running mean of the model walking speed v_p.

$$r_v = \frac{\sum(e^{e_v})}{3} \quad \text{where } e_v = c[\bar{v}_p - v_p]^2 \tag{11}$$

The coefficient $c = 50$.

8.4 Results

8.4.1 Learned gait

The learned musculoskeletal gait model is capable of generating human-like joint kinematics, muscle activation and GRF in a speed range from 0.6 m/s to 1.2 m/s. It could maintain a predefined target walking speed with an error bound of 0.1 m/s when it is initialized with the desired speed. The kinematic behavior generated by the muscle model at 1.2 m/s walking speed in comparison to the experimental data is shown in the Fig. 3. The comparison shows a close correlation (correlation values R between 0.82 to 0.98) between the model and the experimental data for all the lower limb joint angles. Compared to the joint angles, the joint angular velocity patterns of the model are less similar to the experimental data (R values are between 0.46 and 0.92). The R values between the model and the experimental data are higher for lower walking speed (e.g. 0.9 m/s shown in Fig. 4. The model is able to reproduce the asymmetric characteristics in the human data (e.g. hip frontal joint angle).

The GRFs generated by the gait model are not as smooth as in the human experimental data. The mean (over 100 steps of walking) of the vertical GRF from the gait model (muscle based model) has a high correlation with the experimental data with a R value of 0.98 at a walking speed of 1.2 m/s (shown in Fig. 5). The gait model is trained to generate human-like muscle activations through stimulation clipping and optimizing for minimum metabolic cost. The muscle activation patterns generated by the gait model are shown in Fig. 6. The overall muscle activation patterns are similar to the experimental data found in the literature (Perry et al., 2010).

The musculoskeletal gait model produces robust walking. It can recover from the perturbation up to 200 N m on the hip. The perturbation response exhibited by the gait model is highly dependent on the timing of the perturbation. For touch-down and take-off conditions the perturbation response is highly unpredictable and random as it is not exhibiting the expected behaviour of model becoming increasingly unstable with increasing perturbation magnitude. For instance, the performance drops when high extension torques are applied to the swing leg.

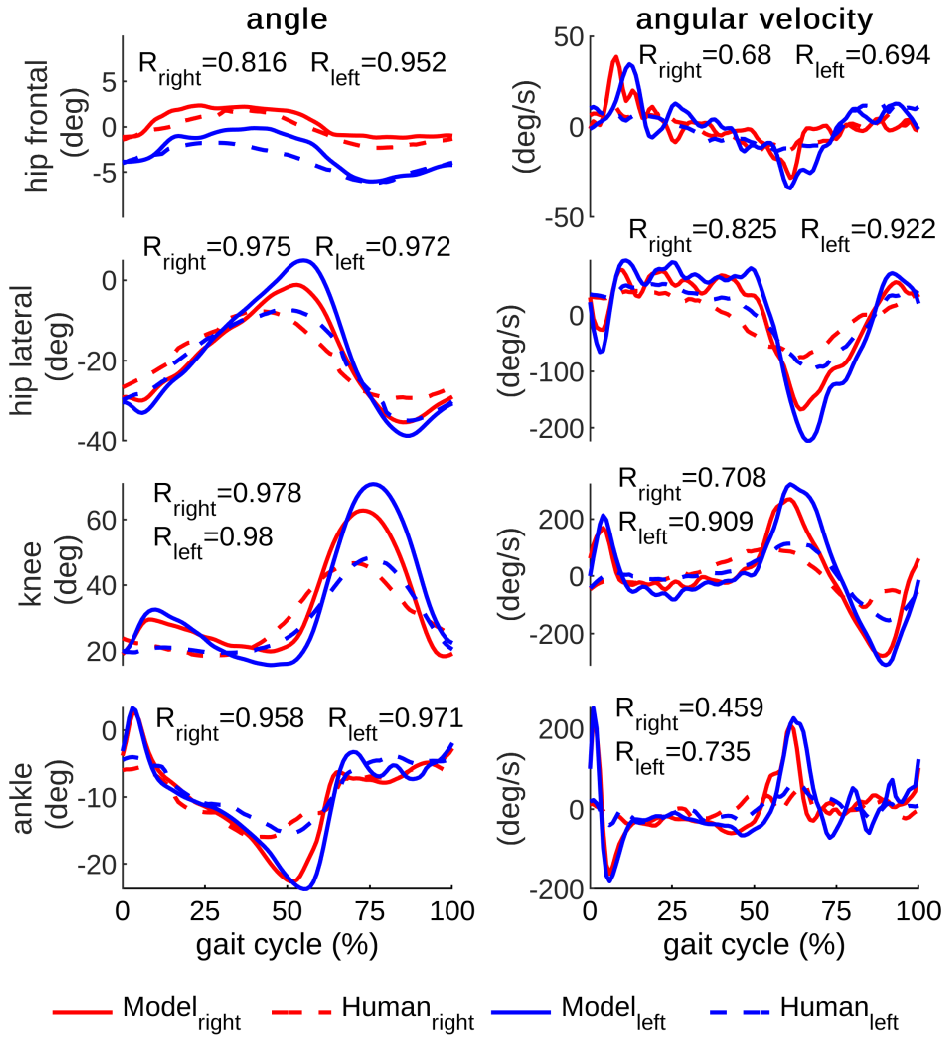

Figure 3: Joint angle and angular velocity of the musculoskeletal gait model (in solid lines) and the human experimental data (in dashed lines) at the walking speed of $1.2\,\mathrm{m/s}$. The data are the mean of 100 steps of steady state walking during a gait cycle (touch-down to touch-down). The red and blue color denote the right and left leg joint data, respectively. The R_{right} and R_{left} denote the cross correlation values (R) for right and left leg joints respectively.

8.4.2 Muscle control vs torque control

After training, the torque based gait model is also able to imitate the human joint kinematics (sample result is shown in Fig. 7). Compared with the torque based model, the muscle based model shows slightly better performance in reproducing human kinematic data. For example the mean (of left and right) R values of the muscle based model are higher than the torque based model for hip adduction/abduction, hip flexion, knee flexion and ankle angle at a walking speed of $1.2\,\mathrm{m/s}$.

The learning progress is depicted in the learning curves in Fig. 8. The muscle model achieves a mean return of 1688 after 10 million time-steps. But the torque model could achieve only a mean return of 1497 after 27.65 million time-steps. Although the same mean return values for both models do not correspond to exactly same behaviour, the returns are comparable as the single step rewards for both the models are scaled between 0 to 10.

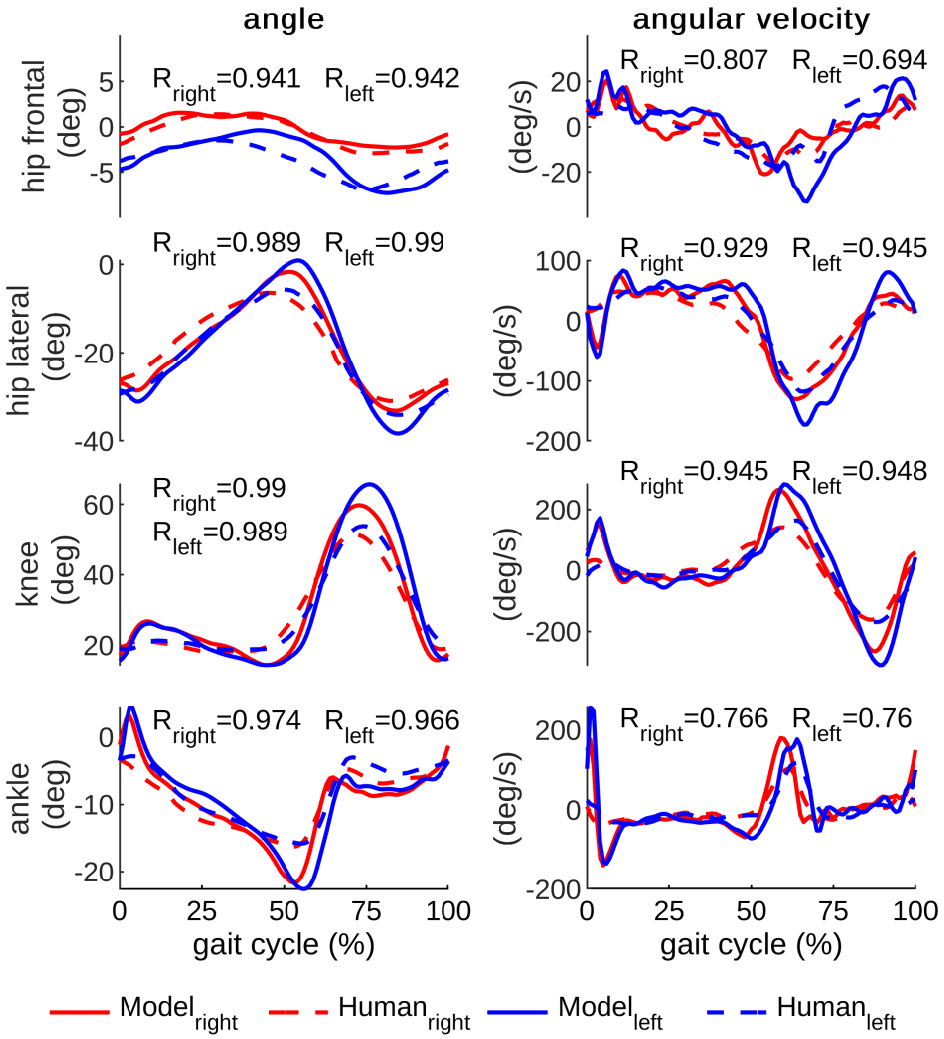

Figure 4: Joint angle and angular velocity of the musculoskeletal gait model (in solid lines) and the human experimental data (in dashed lines) at the walking speed of $0.9\,\mathrm{m/s}$. The data are the mean of 100 steps of steady state walking during a gait cycle (touch-down to touch-down). The red and blue color denote the right and left leg joint data, respectively. The R_{right} and R_{left} denote the cross correlation values (R) for right and left leg joints respectively.

8.5 Discussions

We derived a sensory motor mapping of human walking behavior at the spinal cord level using an artificial neural network. The learned muscle and torque model is able to closely follow the joint angles from experimental data. When comparing the results of our model at $1.2\,\mathrm{m/s}$ with the model from Song and Geyer (Song and Geyer, 2015), our model has a R values of 0.832 and 0.946 for the left and right leg, respectively, compared to 0.54 in their model on reproducing the hip adduction/abduction movement. Also for ankle (frontal plane) movements, our model has a R value of 0.96 compared to 0.46 in their model at $1.2\,\mathrm{m/s}$. Our model could also learn the left-right asymmetries of the human subject very closely, which is evident in the hip movement on the frontal plane. These are considerable improvements over the existing gait models.

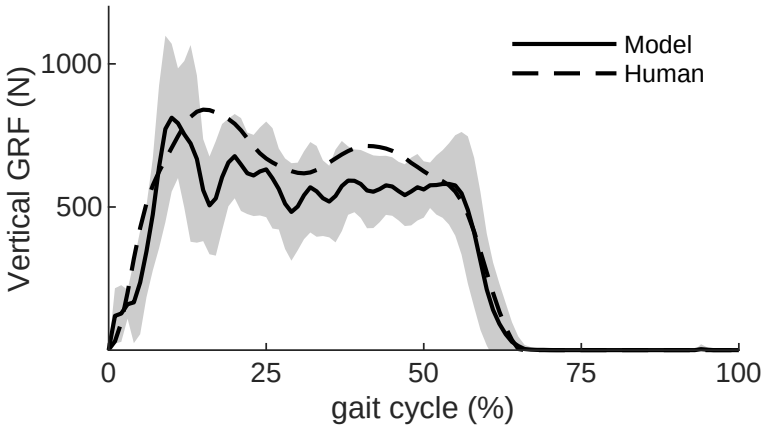

Figure 5: Vertical GRF of the musculoskeletal gait model (the solid line) and the human experimental data (the dashed line) during walking. The mean (over 100 walking steps) GRF for a walking speed of $1.2\,\mathrm{m/s}$ is shown for the musculoskeletal gait model. The error band denotes ± 1 standard deviation.

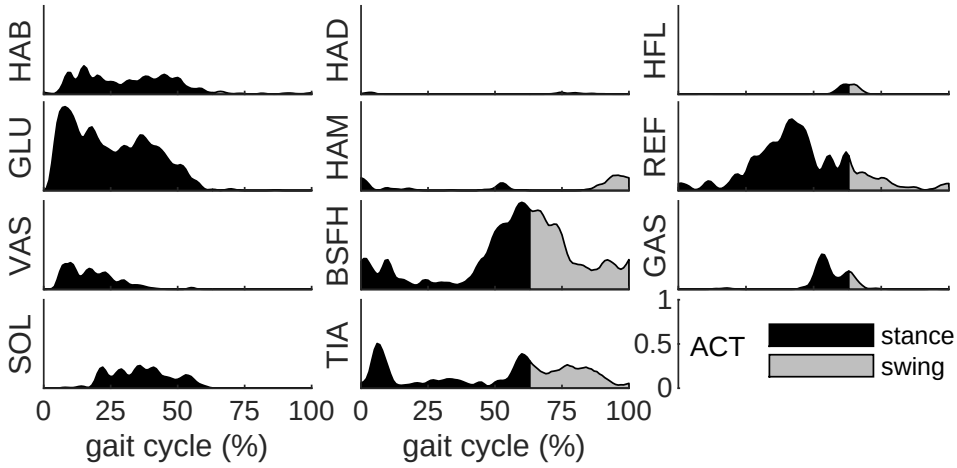

Figure 6: The muscle mean activation of the musculoskeletal gait model at a walking speed of $1.2\,\mathrm{m/s}$. The stance phase and the swing phase are denoted as black and grey area.

Humans tend to walk with a preferred step frequency at a given speed to minimize the metabolic cost (Zarrugh et al., 1974). Thus by optimizing the model for minimum metabolic cost, it enables the model to mimic human-like energetics. The muscle patterns were optimized using metabolic cost minimization and also by clipping the stimulation inputs to the model based general human muscle activation reference data (Song and Geyer, 2015). The HAB, HAD, HFL, GLU, VAS, SOL and TIA muscles have a good correlation to human muscle activation pattern. In contrast, the activation patterns in HAM, REF, BFSH and GAS muscle groups clearly deviate from human patterns. The low activations in GAS is compensated by the high activations of BFSH as these muscles together contribute to knee flexion. Similarly, the higher activation levels of REF muscle group in our model could correspond to the very low activations of HAM muscle group as both contribute to hip extension. The muscle dynamics are different from human data as the metabolic cost may have not yet achieved a global minimum solution. This would demand further optimization.

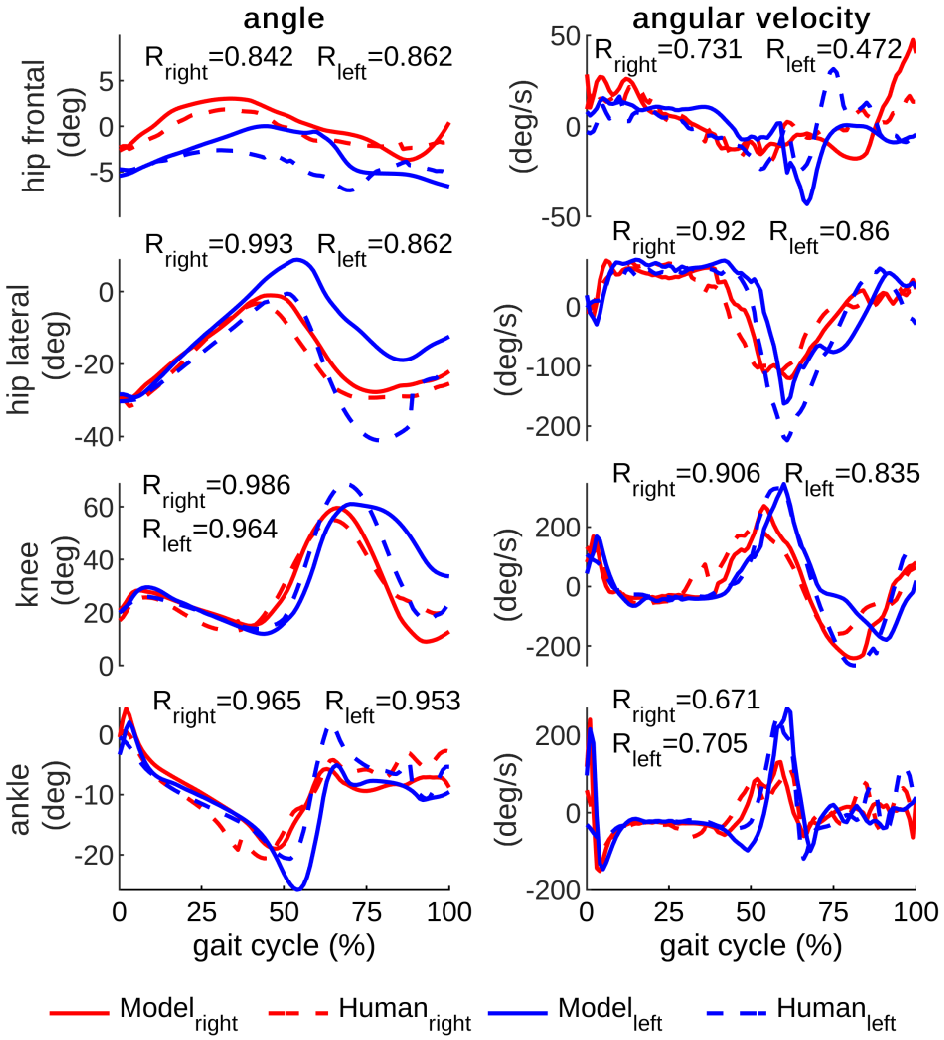

Figure 7: Joint angle and angular velocity of the torque-based gait model (in solid lines) and the human experimental data (in dashed lines) at the walking speed of $1.2\,\mathrm{m/s}$. The red and blue color denote the right and left leg joint data, respectively. R denotes the cross-correlation value.

The GRF profile is an important characteristic in human locomotion (Hirai et al., 1998; Hunter et al., 2005; Keller et al., 1996). This is well visible in the learning procedure as the GRF feedback has a large influence on the final policy. The GRF profile generated by the model is not as smooth as the human experimental data. This could be due to the ground contact model in the simulation is too rigid. It could be resolved by using a more realistic ground contact model. The three-segmented foot model used in OpenSim models could be adopted providing foot the flexibility of a smooth touch-down, roll over and push-off compared to the single rigid foot element with four contact points as in this work.

Compared to torque based model, the muscle based model learned a policy which has higher sample efficiency during training. This result is similar to the findings in other studies, showing the advantages of muscle based control for locomotion tasks over torque based control (Cruz Ruiz et al., 2017; Komura et al., 1997; Peng et al., 2018; Schröder et al., 2003; Shen, 2010). No detailed comparison between the performances of torque based and muscle based control for bipedal locomotion is carried out in this study. But further aspects of muscle based and torque based control will be addressed in the future studies.

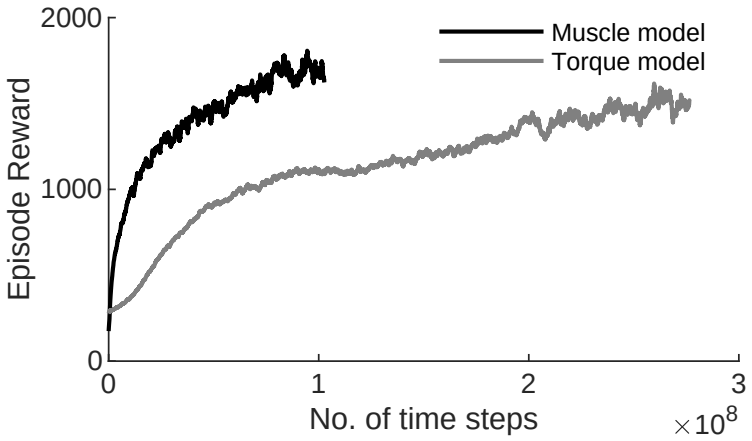

Figure 8: Learning curve of the muscle model (in back) and the torque model (in grey) training.

The perturbation response study for testing the model's robustness generated unexpected results. The response behaviour doesn't show any correspondence with the model stability and the perturbation torques, rather it is highly random. For example model become unstable after 20 steps when a perturbation torque of 40Nm is applied, but model is able to walk up-to 100 steps after applying perturbation torque of 150Nm. The reason for this random perturbation response is not yet clear and needs to be addressed in the future research. This could be a result of the nonlinear policy learned and the passive dynamics of the muscles, which is making the model capable of stabilizing even at very high perturbation toques at the hip such as ± 200 Nm. The muscle model could withstand such high perturbations although it is trained with very low perturbation torques of ± 5 Nm. This is because the muscle based control is taking advantage of its passive dynamics of the musculoskeletal structure to learn a robust policy. But model could not learn the acceleration/deceleration behaviour of the human subject while walking. For example the model looses stability on trying to accelerate from 0.9 m/s to 1.2 m/s within 10-20 steps. This is because of the lack of acceleration/deceleration behaviour in the training data. This could be improved by using training data acquired on an well designed experiment where the subject is asked to accelerate and decelerate between various speeds while walking.

8.6 Conclusions

In this study we explored the idea of learning a gait model to perform human-like walking using deep-RL. For learning the gait model, a reward function was designed based on the kinematics, target walking speed, stability, and metabolic cost. The learned gait model is capable of reproducing human walking kinematics and kinetics robustly at a defined target velocity. The results demonstrate the advantages of modelling the human gait using deep-RL. The results also show that the muscle-based control is superior to the torque-based control in terms of learning sample efficiency. Our future goal is to develop a deep-RL based individualized walking gait model that is more robust and capable of reproducing human response to unexpected perturbations. And with the learned model we aim to identify optimal control schemes for human assistive devices such as lower limb exoskeletons and prostheses.

Acknowledgment

We thank Dr. Martin Grimmer (TU Darmstadt) for helping us in revising the manuscript and conducting the human experiments.

Author contributions

Akhil Anand and Guoping Zhao are the main authors of this paper. Guoping Zhao was responsible for the conceptualization and methodology of this work. Guoping Zhao developed gait model. Akhil Anand implemented the learning algorithm. Akhil Anand and Guoping Zhao interpreted the results and wrote the manuscript. Andre Seyfarth and Hubert Roth were the supervisors of this project and contributed to conceptualizing of the work. All authors revised the manuscript.

References

Alexander, R. M. (1997). Optimum muscle design for oscillatory movements. *Journal of theoretical Biology*, 184(3):253–259.

Blickhan, R. (1989). The spring-mass model for running and hopping. *Journal of Biomechanics*, 22(11–12):1217 – 1227.

Chang, H. S., Fu, M. C., Hu, J., and Marcus, S. I. (2016). Google deep mind's alphago. *OR/MS Today*, 43(5):24–29.

Collins, S., Ruina, A., Tedrake, R., and Wisse, M. (2005). Efficient bipedal robots based on passive-dynamic walkers. *Science*, 307(5712):1082–1085.

Cruz Ruiz, A., Pontonnier, C., Pronost, N., and Dumont, G. (2017). Muscle-based control for character animation. In *Computer Graphics Forum*, volume 36, pages 122–147. Wiley Online Library.

Dhariwal, P., Hesse, C., Klimov, O., Nichol, A., Plappert, M., Radford, A., Schulman, J., Sidor, S., Wu, Y., and Zhokhov, P. (2017). Openai baselines. https://github.com/openai/baselines.

Geyer, H., Seyfarth, A., and Blickhan, R. (2006). Compliant leg behaviour explains basic dynamics of walking and running. *Proceedings. Biological sciences / The Royal Society*, 273(1603):2861–7.

Hirai, K., Hirose, M., Haikawa, Y., and Takenaka, T. (1998). The development of honda humanoid robot. In *Robotics and Automation, 1998. Proceedings. 1998 IEEE International Conference on*, volume 2, pages 1321–1326. IEEE.

Hubicki, C., Grimes, J., Jones, M., Renjewski, D., Spröwitz, A., Abate, A., and Hurst, J. (2016). Atrias: Design and validation of a tether-free 3d-capable spring-mass bipedal robot. *The International Journal of Robotics Research*, 35(12):1497–1521.

Hunter, J. P., Marshall, R. N., and McNair, P. J. (2005). Relationships between ground reaction force impulse and kinematics of sprint-running acceleration. *Journal of applied biomechanics*, 21(1):31–43.

Keller, T. S., Weisberger, A., Ray, J., Hasan, S., Shiavi, R., and Spengler, D. (1996). Relationship between vertical ground reaction force and speed during walking, slow jogging, and running. *Clinical biomechanics*, 11(5):253–259.

Komura, T., Shinagawa, Y., and Kunii, T. L. (1997). A muscle-based feed-forward controller of the human body. In *Computer Graphics Forum*, volume 16, pages C165–C176. Wiley Online Library.

Lillicrap, T. P., Hunt, J. J., Pritzel, A., Heess, N., Erez, T., Tassa, Y., Silver, D., and Wierstra, D. (2015). Continuous control with deep reinforcement learning. *arXiv preprint arXiv:1509.02971*.

McGeer, T. (1990). Passive dynamic walking. *The International Journal of Robotics Research*, 9(2):62–82.

Mnih, V., Badia, A. P., Mirza, M., Graves, A., Lillicrap, T., Harley, T., Silver, D., and Kavukcuoglu, K. (2016). Asynchronous methods for deep reinforcement learning. In *International conference on machine learning*, pages 1928–1937.

Peng, X. B., Abbeel, P., Levine, S., and van de Panne, M. (2018). Deepmimic: Example-guided deep reinforcement learning of physics-based character skills. *arXiv preprint arXiv:1804.02717*.

Peng, X. B., Berseth, G., Yin, K., and Van De Panne, M. (2017). Deeploco: Dynamic locomotion skills using hierarchical deep reinforcement learning. *ACM Transactions on Graphics (TOG)*, 36(4):41.

Peng, X. B. and van de Panne, M. (2017). Learning locomotion skills using deeprl: Does the choice of action space matter? In *Proceedings of the ACM SIGGRAPH/Eurographics Symposium on Computer Animation*, page 12. ACM.

Perry, J., Burnfield, J., and Burnfield, J. (2010). *Gait Analysis: Normal and Pathological Function*. SLACK.

Schröder, J., Kawamura, K., Gockel, T., and Dillmann, R. (2003). Improved control of a humanoid arm driven by pneumatic actuators. *Proceedings of Humanoids 2003*.

Schulman, J., Levine, S., Abbeel, P., Jordan, M., and Moritz, P. (2015). Trust region policy optimization. In *International Conference on Machine Learning*, pages 1889–1897.

Schulman, J., Wolski, F., Dhariwal, P., Radford, A., and Klimov, O. (2017). Proximal policy optimization algorithms. *arXiv preprint arXiv:1707.06347*.

Shen, X. (2010). Nonlinear model-based control of pneumatic artificial muscle servo systems. *Control Engineering Practice*, 18(3):311–317.

Song, S. and Geyer, H. (2015). A neural circuitry that emphasizes spinal feedback generates diverse behaviours of human locomotion. *The Journal of physiology*, 593(16):3493–3511.

Song, S. and Geyer, H. (2017). Evaluation of a neuromechanical walking control model using disturbance experiments. *Frontiers in Computational Neuroscience*, 11:15.

Todorov, E., Erez, T., and Tassa, Y. (2012). Mujoco: A physics engine for model-based control. In *2012 IEEE/RSJ International Conference on Intelligent Robots and Systems*, pages 5026–5033.

Wang, Z., Bapst, V., Heess, N., Mnih, V., Munos, R., Kavukcuoglu, K., and de Freitas, N. (2016). Sample efficient actor-critic with experience replay. *arXiv preprint arXiv:1611.01224*.

Zarrugh, M. Y., Todd, F. N., and Ralston, H. J. (1974). Optimization of energy expenditure during level walking. *European Journal of Applied Physiology and Occupational Physiology*, 33(4):293–306.

Zhao, G., Sharbafi, M., Vlutters, M., van Asseldonk, E., and Seyfarth, A. (2017). Template model inspired leg force feedback based control can assist human walking. In *2017 International Conference on Rehabilitation Robotics (ICORR)*, pages 473–478.

9 Conclusion

Currently, the performance of artificial legged robotic systems (e.g. humanoid robots, prostheses, exoskeletons, etc.) are inferior compared to humans in terms of stability, versatility and energetics. Investigating human locomotor systems can help us improve the robotic systems by employing the learned bio-inspired concepts.

This thesis aimed at exploring the bio-inspired approaches for further understanding human locomotion. It presents a systematic way of investigating the bio-inspired approaches from concepts to applications for human locomotion. The main contribution of this work is demonstrating how the bio-inspired concepts are extracted from the human experimental data, tested with the simulation models, and implemented and validated with the hardware systems. The outcome of this work can be used as a guideline to develop novel bio-inspired controllers for improving legged and wearable robots.

This thesis consists of interdisciplinary studies including biomechanical analyses of human experimental data, robot design and control, neuromuscular modeling and reinforcement learning. The key outcomes of this thesis are summarized in the following.

9.1 Methodology for investigating bio-inspired concepts

The test trilogy includes simulations, hardware implementations, and human experiments (Kalveram and Seyfarth, 2009). It has been proposed as a method for evaluating if the bio-inspired concepts are valid. Inspired by the test trilogy, this thesis includes three main parts: biomechanical studies on human experimental data, simulations (modeling of human locomotion), and implementations on robots and exoskeletons. The biomechanical studies provide insights and indicate underlying principles (concepts) of human locomotor subfunctions (Article I and II). The simulation studies can help us test the bio-inspired concepts and reveal the key mechanisms of human locomotion control (Article VI). The hardware implementations validate the bio-inspired concepts by demonstrating the feasibility and benefits of applying the concepts on robots (Article V).

In this work, we extended the test trilogy by adding one more step: applying the bio-inspired concepts back to human body with wearable robots (e.g. an exoskeleton, Article III and IV). Bio-inspired concepts are often proposed based on human locomotion data in steady state condition. It is unclear how humans will respond if we implement the bio-inspired concept based control on wearable robots. The validity of the bio-inspired concepts can be justified if human are assisted during the locomotion.

9.2 Synergies between locomotor subfunctions

Human legged locomotor systems can be divided into three subfunctions which are stance (axial leg function), swing (rotational leg function) and balance (posture control) (Seyfarth et al., 2013). Finding out the how different subfunctions interact with each other can help us further understand the underlying mechanisms of human locomotion.

We find a phase locking mechanism and synergistic interactions among the three locomotor subfunctions by analyzing how much swing leg, stance leg and trunk motion contribute to the total ground reaction forces during human walking at five different speeds (Article I). The results show that, in vertical

direction, the force created by the swing leg movement has an in-phase M-shape pattern with respect to the force created by the trunk. In contrast, the vertical force created by the stance leg movement is almost constant. In the fore-aft direction, we find that the stance leg and the swing leg are coupled. The forces created by the movement of the stance leg and the swing leg cancel each other out.

In addition, analyses on the human gait initiation experimental data reveal the emergence of stance leg and swing leg subfunctions from lower limb-joint perspective (Article II). Further, in order to keep balance, a strong correlation between the control of frontal plane joints and sagittal plane joints has been found. More specifically, the results show that the initial lateral weight shift is achieved by the hip abduction torque on the lifting leg (leading limb). Before the take-off (TO) of the leading limb, the body forward movement is initiated by decreasing the ankle plantarflexion torque, which results in an inverted pendulum-like passive forward falling. The hip flexion/extension joint has the highest positive mechanical energy output in the first stride of the leading limb, while the ankle joint contributes the most positive mechanical energy in the first stride of the trailing limb (stance leg). The vertical ground reaction forces and all joint kinetics show similar patterns as in the reference walking stride after the leading limb TO.

The identified synergies between locomotor subfunctions suggest that the support of one subfunction could provide benefits for the others.

9.3 Bio-inspired leg force reflex based control can assist human walking

In the two exoskeleton implementation studies (Article III and IV), a novel bio-inspired leg force reflex based simple approach was introduced and applied for control of a lower-limb exoskeleton to assist human walking. In the first study (Article III), the bio-inspired concept was implemented for assisting both hip and knee joints. In the second study (Article IV), only hip joints were assisted. Although the bio-inspired leg force reflex based control concept was developed for achieving the posture balance subfunction, the results of both studies show that human walking can be assisted (reductions in muscle activations and metabolic costs can be found). This demonstrates that the proposed bio-inspired controller allows a synergistic interaction between human and the exoskeleton. It also supports the concept of synergies between human locomotor subfunctions (Article I and II).

Further, in the second study (Article IV), we also investigated the importance of the leg force reflex for the assistive controller. The results show that, although the metabolic costs can also be reduced without the leg force reflex, the leg force reflex based controller results in more natural kinematic behavior, more consistent reduction in muscle activation, smoother motor torques and less peak power form the exoskeleton. These demonstrate that the proposed bio-inspired leg force reflex based controller can not only facilitate the human gait, but also reduce the exoskeleton power consumption.

9.4 Bio-inspired neuromuscular reflex based control for hopping robot

In order to demonstrate the feasibility and benefits of neuromuscular reflex based control for stance leg (rebounding) function, we built a low-cost hopping robot and implemented the novel bio-inspired neuromuscular reflex based hopping controller on the robot (Article V). The results show that the stable hopping can be achieved with both positive force and length reflex while the velocity reflex could result in unstable behaviors. The force reflex based control is more stable than the length reflex based con-

trol. In addition, the force reflex based control is robust against the changes in body mass and ground impedance. Further, the neuromuscular properties play an important role in stabilizing the hopping motion. The results demonstrate the neuromuscular reflex based control approach is feasible to implement and capable of achieving stable and robust hopping in a real robot. It provides a promising direction of controlling the legged robot to achieve robust dynamic motion in the future.

9.5 Individualized gait modeling with reinforcement learning

Current human gait models and bio-inspired concepts are mostly only valid for describing human steady state periodic locomotion. A gait model capable of generating individualized walking behavior at both the kinematic and the muscular level can be a very useful framework for developing control schemes for humanoids and wearable robots such as exoskeletons and prostheses. In Article VI, we explored the idea of using deep reinforcement learning based approach for neuromuscular gait modeling. The subject joint kinematic data were used in the reward function for learning the subject specific walking behavior. The results show that the gait model can closely reproduce the human kinematics and ground reaction forces during walking. It is also able to withstand unexpected hip torque perturbations during walking. We further explored the advantages of using the neuromuscular based model over the ideal joint torque based model. We observed that the neuromuscular model is more sample efficient compared to the torque model.

9.6 Outlook

This work provides a framework for systematically investigating bio-inspired approaches for human locomotion from concepts to applications. This framework can be used for further understanding the underlying principles of dynamic legged locomotion in humans and applying these bio-inspired principles to the design and control of legged robots.

The observed insights on the synergies between different subfunctions during walking and gait initiation can be used to develop more robust and versatile walking models (e.g. extending the models from Maus et al. (2010); Sharbafi and Seyfarth (2015)). The human gait initiation data can also be used to optimize the control parameters of multi-segment musculoskeletal walking models (e.g. Geyer and Herr (2010); Song and Geyer (2015)). Such a model could provide further insights on how human generate different gaits at the neuromuscular level. Further, the human experimental data can also be used for training the individualized gait model from Article VI. The trained model could be used as part of a controller for prostheses and exoskeletons (e.g. in Article III and IV) to support human walking. In addition, the human-in-the-loop optimization approach (Ding et al., 2018; Zhang et al., 2017) could also be implemented in the future to automatically generate subject specific control parameters of the bio-inspired controller for better assisting human locomotion with exoskeletons. Besides, the walking gait models can also be implemented on humanoid robots to achieve more robust and dynamic gaits.

Investigating human responses to unexpected perturbations during locomotion (e.g. Ferber et al. (2002); Hof et al. (2010); Vlutters et al. (2018)) can further reveal the mechanisms of human locomotor control systems. In the future, we will combine the perturbation studies with the simulation approaches mentioned above to investigate the role of muscle properties and muscle reflexes in human dynamic legged locomotion.

References

Ding, Y., Kim, M., Kuindersma, S., and Walsh, C. J. (2018). Human-in-the-loop optimization of hip assistance with a soft exosuit during walking. *Science Robotics*, 3(15):eaar5438.

Ferber, R., Osternig, L. R., Woollacott, M. H., Wasielewski, N. J., and Lee, J.-H. (2002). Reactive balance adjustments to unexpected perturbations during human walking. *Gait & Posture*, 16(3):238 – 248.

Geyer, H. and Herr, H. (2010). A muscle-reflex model that encodes principles of legged mechanics produces human walking dynamics and muscle activities. *IEEE Transactions on neural systems and rehabilitation engineering*, 18(3):263–273.

Hof, A. L., Vermerris, S. M., and Gjaltema, W. A. (2010). Balance responses to lateral perturbations in human treadmill walking. *Journal of Experimental Biology*, 213(15):2655–2664.

Kalveram, K. T. and Seyfarth, A. (2009). Inverse biomimetics: How robots can help to verify concepts concerning sensorimotor control of human arm and leg movements. *Journal of Physiology-Paris*, 103(3):232 – 243. Neurorobotics.

Maus, H.-M., Lipfert, S. W., Gross, M., Rummel, J., and Seyfarth, A. (2010). Upright human gait did not provide a major mechanical challenge for our ancestors. *Nature communications*, 1(6):70.

Seyfarth, A., Grimmer, S., et al. (2013). Biomechanical and neuromechanical concepts for legged locomotion: Computer models and robot validation: Andre seyfarth, sten grimmer, daniel häufle, horst-moritz maus, frank peuker and karl-theodor kalveram. In *Routledge Handbook of Motor Control and Motor Learning*, pages 99–119. Routledge.

Sharbafi, M. A. and Seyfarth, A. (2015). FMCH: A new model for human-like postural control in walking. In *Intelligent Robots and Systems (IROS), 2015 IEEE/RSJ International Conference on*, pages 5742–5747.

Song, S. and Geyer, H. (2015). A neural circuitry that emphasizes spinal feedback generates diverse behaviours of human locomotion. *The Journal of physiology*, 593(16):3493–3511.

Vlutters, M., van Asseldonk, E. H. F., and van der Kooij, H. (2018). Lower extremity joint-level responses to pelvis perturbation during human walking. *Scientific Reports*, 8(1):14621.

Zhang, J., Fiers, P., Witte, K. A., Jackson, R. W., Poggensee, K. L., Atkeson, C. G., and Collins, S. H. (2017). Human-in-the-loop optimization of exoskeleton assistance during walking. *Science*, 356(6344):1280–1284.

10 List of own publications

Journal Papers

- Sharbafi, M. A., Rode, C., Kurowski, S., Scholz, D., Möckel, R., Radkhah, K., **Zhao, G.**, Rashty, A. M., von Stryk, O., and Seyfarth, A. (2016). A new biarticular actuator design facilitates control of leg function in BioBiped3. *Bioinspiration & Biomimetics*, 11(4):046003.
- Sharbafi, M. A., Seyfarth, A., and **Zhao, G.** (2017). Locomotor Sub-functions for Control of Assistive Wearable Robots. *Frontiers in Neurorobotics*, 11:44.
- Sharbafi, M. A., Shin, H., **Zhao, G.**, Hosoda, K. and Seyfarth, A. (2017). Electric-Pneumatic Actuator: A New Muscle for Locomotion. In *Actuators*, 6(4):30. Multidisciplinary Digital Publishing Institute.
- Van Nimmen, K., **Zhao, G.**, Seyfarth, A., and Van den Broeck, P. (2018). A robust methodology for the reconstruction of the vertical pedestrian-induced load from the registered body motion. *Vibration*, 1(2):250–268.
- **Zhao, G.**, Sharbafi, M., Vlutters, M., van Asseldonk, E., and Seyfarth, A. (2019). Bio-inspired Balance Control Assistance Can Reduce Metabolic Energy Consumption In Human Walking. Accepted for publication in *IEEE Transactions on Neural Systems & Rehabilitation Engineering*.

Conference Papers

- **Zhao, G.** and Seyfarth, A. (2015). Contributions of stance and swing leg movements to human walking dynamics. In *ASSISTIVE ROBOTICS: Proceedings of the 18th International Conference on CLAWAR 2015*, pages 224–231. World Scientific.
- **Zhao, G.**, Sharbafi, M., Vlutters, M., van Asseldonk, E., and Seyfarth, A. (2017). Template model inspired leg force feedback based control can assist human walking. In *2017 International Conference on Rehabilitation Robotics (ICORR)*, pages 473–478.
- Schumacher, C., Grimmer, M., Scherf, A., **Zhao, G.**, Beckerle, P., and Seyfarth, A. (2018). A movement manipulator to introduce temporary and local perturbations in human hopping. In *2018 7th IEEE International Conference on Biomedical Robotics and Biomechatronics (Biorob)*, pages 940–947.
- Seyfarth, A., Sharbafi, M. A., **Zhao, G.**, and Schumacher, C. (2019). Modular composition of human gaits through locomotor subfunctions and sensor-motor-maps. In Carrozza, M. C., Micera, S., and Pons, J. L., editors, *Wearable Robotics: Challenges and Trends*, pages 339–343, Cham. Springer International Publishing.

Curriculum vitae

Guoping Zhao

Born on August 1, 1989
From Huai'an, Jiangsu, P. R. China

Education

- **Technische Universität Darmstadt**, *Lauflabor Locomotion Laboratory* — Darmstadt, Germany
  Phd, Dr.rer.nat in Biomechanics — **2013 - 2019**
  Dissertation: Bio-inspired Approaches for Human Locomotion: From Concepts to Applications
- **Southeast University**, *School of Mechanical Engineering* — Nanjing, P. R. China
  M.Sc. in Mechatronics Engineering — **2010 - 2013**
  Thesis: Analysis and Application Research on Human Lower Limb Movement
- **Southeast University**, *School of Mechanical Engineering* — Nanjing, P. R. China
  B.Eng. in Mechanical Engineering and Automation — **2006 - 2010**
  Thesis: Measurement and Analysis on Electromyogram and Mechanomyogram of Human Skeletal Muscle

Research Experience

- **Researcher at Lauflabor Locomotion Laboratory, TU Darmstadt** — **2013 - 2019**
  - Electric-Pneumatic Actuator (EPA) project funded by the German Research Foundation (DFG) under grant No. AH307/2-1 and SE1042/29-1.
  - Balance Augmentation in Locomotion, through Anticipative, Nature and Cooperative control of Exoskeleton (BALANCE) project funded under grant 601003 of the Seventh Framework Program (FP7) of the European Commission (Information and Communication Technologies, ICT-2011.2.1).